UNIVERSITY OF CALIFORNIA SAN DIEGO

Multi-electron Polyanion Cathode, $VOPO_4$, for High Energy Density Alkali-ion Batteries

A dissertation submitted in partial satisfaction of the

requirements for the degree Doctor of Philosophy

in

Materials Science and Engineering

by

Yuh-Chieh Lin

Committee in charge

Professor Shyue Ping Ong, Chair
Professor Ping Liu
Professor Shirley Meng
Professor Yu Qiao
Professor Sheng Xu

2018

The Dissertation of Yuh-Chieh Lin is approved, and it is acceptable in quality and form for publication on microfilm and electronically:

_____

_____

_____

_____

_____

Chair

University of California San Diego

2018

DEDICATION

To

my grandparents, parents and elder sister

TABLE OF CONTENTS

LIST OF FIGURES

LIST OF TABLES

ACKNOWLEDGEMENTS

First of all, I would like to express my gratitude to my advisor, Dr. Shyue Ping Ong, for his great support and guidance throughout my graduate studies. I deeply admire him for his professionalism in scientific research and code development. My deepest gratitude also goes to the thesis committee Dr. Shirley Meng, Dr. Ping Liu, Dr. Sheng Xu and Dr. Yu Qiao for their assistance in the completion of this dissertation.

Secondly, I am grateful to my previous and current collaborators, Dr. Iek-Heng Chu, Dr. Balachandran Radhakrishnan, Dr. Zhenbin Wang, Dr. Xiangguo Li, Richard Tran, Marc F. V. Hidalgo and Bohua Wen.

Finally, I would like to thank my grandmother, parents and elder sister for their unconditional support and encouragement through this journey.

Chapter 2 is, in full, a reprint of the material "Thermodynamics, Kinetics and Structural Evolution of ε-$LiVOPO_4$ over Multiple Lithium Intercalation" as it appears in Chemistry of Materials, Y.-C. Lin, B. Wen, K. M. Wiaderek, S. Sallis, H. Liu, S. H. Lapidus, O. J. Borkiewicz, N. F. Quackenbush, N. A. Chernova, K. Karki, F. Omenya, P. J. Chupas, L. F. J. Piper, M. S. Whittingham, K. W. Chapman and S. P. Ong, 2016, 28, 1794–1805. The dissertation author was the primary investigator and author of this paper. All calculations and corresponding data analysis were done by the author. The experimental portion of the work – synthesis, characterization and data analysis were done by collaborators, B. Wen, K. M. Wiaderek, S. Sallis, H. Liu, S. H. Lapidus, O. J. Borkiewicz, N. F. Quackenbush, K. Karki, F. Omenya, P. J. Chupas.

Chapter 3 is, in full, a reprint of the material "Comparison of the polymorphs of $VOPO_4$ as multi-electron cathodes for rechargeable alkali-ion batteries" as it appears in Journal of Materials Chemistry A, Y. C. Lin, M. F. V. Hidalgo, I. H. Chu, N. A. Chernova, M. Stanley Whittingham

and S. P. Ong, 2017, **5**, 17421–17431. The dissertation author was the primary investigator and author of this paper. All calculations and corresponding data analysis were done by the author. The experimental portion of the work – synthesis, characterization and data analysis were done by collaborator, M. F. V. Hidalgo.

Chapter 4 is, in full, is a preprint currently being prepared for submission for publication of the material "Rational Synthesis and Electrochemical Performance of $LiVOPO_4$ Polymorphs", Marc F. V. Hidalgo, Yuh-Chieh Lin, Antonin Grenier, Dongdong Xiao, Richard Tran, Huolin Xin, Jennifer Donohue, Fredrick O. Omenya, Iek-Heng Chu, Zhenbin Wang, Xiangguo Li, Natasha A. Chernova, Karena W. Chapman, Guangwen Zhou, Shyue Ping Ong, and M. Stanley Whittingham. The dissertation author was a co-primary investigator and author of this paper. All calculations and corresponding data analysis were done by the author. The experimental portion of the work – synthesis, characterization and data analysis were done by collaborator, M. F. V. Hidalgo.

I would like to acknowledge NorthEast Center for Chemical Energy Storage for providing the financial support via Grant No. DE-SC0012583. I would also like to acknowledge computing resources provided by the Triton Shared Computing Cluster (TSCC) at the University of California, San Diego, the National Energy Research Scientific Computing Centre (NERSC), and the Extreme Science and Engineering Discovery Environment (XSEDE), which is supported by National Science Foundation Grant No. ACI1053575.

VITA

2009 Bachelor of Engineering, National Cheng Kung University, Taiwan

2013 Master of Engineering, University of Florida, USA

2018 Doctor of Philosophy, University of California San Diego, USA

PUBLICATIONS

1. N. F. Quackenbush, L. Wangoh, D. O. Scanlon, R. Zhang, Y. Chung, Z. Chen, B. Wen, Y. Lin, J. C. Woicik, N. A. Chernova, S. P. Ong, M. S. Whittingham and L. F. J. Piper, *Chem. Mater.*, 2015, **27**, 8211–8219.

2. Y. Huang, Y.-C. Lin, D. M. Jenkins, N. A. Chernova, Y. Chung, B. Radhakrishnan, I.-H. Chu, J. Fang, Q. Wang, F. Omenya, S. P. Ong and M. S. Whittingham, *ACS Appl. Mater. Interfaces*, 2016, **8**, 7013–7021.

3. Y.-C. Lin, B. Wen, K. M. Wiaderek, S. Sallis, H. Liu, S. H. Lapidus, O. J. Borkiewicz, N. F. Quackenbush, N. A. Chernova, K. Karki, F. Omenya, P. J. Chupas, L. F. J. Piper, M. S. Whittingham, K. W. Chapman and S. P. Ong, *Chem. Mater.*, 2016, **28**, 1794–1805.

4. I. H. Chu, H. Nguyen, S. Hy, Y. C. Lin, Z. Wang, Z. Xu, Z. Deng, Y. S. Meng and S. P. Ong, *ACS Appl. Mater. Interfaces*, 2016, **8**, 7843–7853.

5. B. Wen, Q. Wang, Y. Lin, N. A. Chernova, K. Karki, Y. Chung, F. Omenya, S. Sallis, L. F. J. Piper, S. P. Ong and M. S. Whittingham, *Chem. Mater.*, 2016, **28**, 3159–3170.

6. L. W. Wangoh, S. Sallis, K. M. Wiaderek, Y. C. Lin, B. Wen, N. F. Quackenbush, N. A. Chernova, J. Guo, L. Ma, T. Wu, T. L. Lee, C. Schlueter, S. P. Ong, K. W. Chapman, M. S. Whittingham and L. F. J. Piper, *Appl. Phys. Lett.*, , DOI:10.1063/1.4960452.

7. Y. C. Lin, M. F. V. Hidalgo, I. H. Chu, N. A. Chernova, M. Stanley Whittingham and S. P. Ong, *J. Mater. Chem. A*, 2017, **5**, 17421–17431.

8. J. Ding, Y. C. Lin, J. Liu, J. Rana, H. Zhang, H. Zhou, I. H. Chu, K. M. Wiaderek, F. Omenya, N. A. Chernova, K. W. Chapman, L. F. J. Piper, S. P. Ong and M. S. Whittingham, *Adv. Energy Mater.*, 2018

ABSTRACT OF THE DISSERTATION

Multi-electron Polyanion Cathode, $VOPO_4$, for High Energy Density Alkali-ion Batteries

by

Yuh-Chieh Lin

Doctor of Philosophy in Materials Science and Engineering

University of California San Diego, 2018

Professor Shyue Ping Ong, Chair

Today's commercial lithium-ion battery cathodes function on the basis of a single-electron transfer per transition metal. To attain significantly higher capacities, particularly in polyanionic compounds with higher voltages, achieving reversible multi-electron transfer per transition metal is necessary. In this thesis, we use first principles calculations to study the thermodynamics and kinetics of $AVOPO_4$ (A = Li, Na), one of the most promising multi-electron cathodes for alkali-ion batteries, with the aim of providing crucial insights into its electrochemical performance and suggesting further optimizations. This thesis comprises three complementary projects.

In the first project, we demonstrated the stable cycling of more than one Li in solid-state-synthesized ε-$LiVOPO_4$ for the first time. Using joint first-principles calculations and experimental measurements, we presented a comprehensive analysis of the thermodynamics,

kinetics, and structural evolution of ε-Li_xVOPO_4 over the entire lithiation range (x=0 ~ 2). We unveiled two intermediate phases at x = 1.5 and 1.75 in the low-voltage regime (x=1 ~ 2) and showed that the capacity limitation in the high-voltage region is likely driven by Li mobility limitations whereas the increasing polarization in the low-voltage region is the result of structural changes. Finally, we predicted that ε-Li_xVOPO_4 is likely a pseudo-1D ionic diffuser with low electronic conductivity using DFT calculations, which suggests that nanosizing and carbon coating are crucial to achieve good electrochemical performance in this material.

In the second project, we conducted a combined first-principles and experimental study to evaluate the thermodynamic stability, voltage, band gap and diffusion kinetics for Li and Na intercalation in the β, ε and α_I polymorphs of $VOPO_4$. We found that all $VOPO_4$ polymorphs remain reasonably stable with one alkali-ion insertion but are significantly destabilized with two alkali-ion insertion. We predicted that the α_I polymorph has higher Li^+ migration barriers and larger band gaps than the other polymorphs, which accounts for the relatively worse electrochemical cycling performance observed. On the other hand, only the layered α_I polymorph exhibits reasonably low barriers for Na^+ migration, which are consistent with observed electrochemical performances reported thus far in the literature. We also showed that differences in voltage, kinetics and rate capability of these different polymorphs for alkali-ion insertion can be ascribed to their fundamentally different VO_6/VO_5-PO_4 frameworks.

In the final project, we synthesized all three major polymorphs of $LiVOPO_4$ (α_I, β and ε) using a single precursor, $LiVOPO_4 \cdot 2H_2O$, thereby minimizing effects of synthesis on the properties of the materials. We demonstrated that $LiVOPO_4$ undergoes the following phase transitions upon heating: $LiVOPO_4 \cdot 2H_2O \rightarrow \alpha_I$-$LiVOPO_4 \rightarrow$ β-$LiVOPO_4 \rightarrow$ ε-$LiVOPO_4$. Metastable α_I-$LiVOPO_4$ forms initially due to its structural similarity to the $LiVOPO_4 \cdot 2H_2O$ precursor via H_2O removal.

Between the two almost energetically-degenerate β and ε polymorphs, formation of the β phase is favored in an oxidizing atmosphere, while ε is favored at high temperatures and an inert atmosphere. DFT defect calculations show that β-$LiVOPO_4$ is more stable in the presence of O interstitials, while ε-$LiVOPO_4$ is more stable in the presence of O vacancies. We also demonstrated that the calculated Wulff shape of β-$LiVOPO_4$ shows an increased presence of facets with superior surface ion kinetics in an oxidizing atmosphere, which explains its improved rate performance relative to ε-$LiVOPO_4$ in the high voltage regime.

In conclusion, the work completed in this thesis has provided critical new insights into the promising $AVOPO_4$ family of multi-electron cathodes. A tightly integrated DFT and experimental effort has shed light on the phase stability and equilibria and kinetics of these cathodes across the entire lithiation range. Leveraging on these insights, we have optimized synthesis to achieve close to full two-electron cycling in the β-$LiVOPO_4$ and ε-$LiVOPO_4$.

Chapter 1. Introduction

1.1 Background

With growing concerns over the environmental, climate, and health impacts caused by using fossil fuels, various renewable energy sources, such as wind, solar and hydroelectric, are believed to be promising alternatives to support more sustainable economic growth. However, most renewable energy sources are intermittent in nature and hence must be complemented with an energy storage solution. Li-ion batteries (LIB) is regarded as one of the near-term solutions because of its combination of high energy and power density. Nowadays, LIB are widely used for the portable electronic devices such as cell phone, laptop, etc., and aggressively enter the large-scale high-power market, particularly the domain of sustainable hybrid/full electric vehicle.[1]

In recent years, part of attention has been shifted to the Na-ion battery (NIB), due to the cost and abundance of Na.[2–5] Although the energy density of NIB may not reach that of LIB because Na is more than three times heavier than Li and the standard electrochemical potential of Na (2.71 V) is lower than Li (3.04 V) with respect to standard hydrogen electrode, NIB are competitive in the applications of a large grid support where the operation cost and longevity of the battery are more important aspects of a whole system.

Figure 1.1 shows the configuration of an alkali-ion battery (AIB), which is composed of cathode, anode and electronically insulating, ion-conducting electrolyte. Initially, all alkali ions are in the cathode sides and the battery system is assembled in "discharged" status. During charge, alkali ions are extracted from the cathode host, through the electrolyte, into the anode host. Meanwhile, electrons also move from cathode to anode through external electric circuit. The chemical potential of alkali ion is much higher in the anode than in the cathode and hence the electric energy is stored in the form of electrochemical energy. During discharge, the

electrochemical energy is released in the form of electric energy. Typical cathodes are transition metal oxides, while the most common form of anode is graphitic carbon.

The energy density of a rechargeable AIB is governed primarily by the capacity and voltage of the active electrode materials, which have been the main focus in battery research. In most commercial cathodes, the maximum number of electrons transferred per cycle is in general less than one per transition metal, which ultimately limits achievable capacity. For example, the commercial $LiCoO_2$ can merely utilize ~0.5 Li or electron because full extraction of Li will lead to structure instability even though it has high theoretical capacity of 272 mAh/g.[6] $LiFePO_4$ can achieve cycling of ~0.7 – 0.9 Li albeit with a lower voltage of ~3.45V.[6] To further increase the energy density, a potential avenue is to develop multielectron alkali-ion cathodes, which can cycle more than one electron per transition metal.

1.2 Review of multi-electron AIB cathode

Metal fluorides as multielectron cathodes were first reported by Arai *et al*; however, only one third of the theoretic capacity (236 mAh/g) of FeF_3 was demonstrated in a discharge voltage region from ~4.5 to 2 V, which was attributed to the poor electronic conductivity and questionable ionic conductivity.[7] Later, FeF_3 : C-based carbon metal fluoride nanocomposites was shown with a reversible specific capacity of ~600 mAh/g but with large stepwise voltage gaps leading to large fluctuation in the power output. Almost at the same time, Li *et al*. reported reversible lithium storage capacities of TiF_3 and VF_3 being realized as high as 500 – 600 mAh/g, due to a reversible formation and decomposition of LiF upon lithium insertion into the metal fluorides. Metal sulfides have also been investigated as potential positive-electrode materials.[8–11] The advantage of metal sulfides is that the sulfur might participate in the multielectron redox reaction in addition to the transition metal leading to high energy density although their typical voltages are lower than those

of oxides. For example, crystalline TiS_3 was reported with reversible capacities greater than 300 mAh/g, involving more than two electrons during cycling process.[8–11] However, the reversibility of TiS_3 was low, which might be attributed to the structural transformation from a trigonal prism to a more stable octahedron.[9–11] Later, amorphous TiS_3 was reported with improved electrochemical performance due to the three-dimensional framework, which would be favorable for stabilizing its structure against the large volume changes in cycling process.[12,13] Recently, Li_2TiS_3 and Li_3NbS_4 were reported with high gravimetric energy densities of 850 and 780 Wh/kg corresponding to 2.5- and 3.5-electron processes, which are much higher than the 660 Wh/kg of $LiCoO_2$.[14] Although Li_2TiS_3 exhibited high capacity retention, the capacity faded quickly within 10 cycles probably due to the volume change. For oxides, ω-$Li_xV_2O_5$, was reported enabling ~1.5 Li^+ per transition metal (~300 mAh/g) leading to high energy density of 800 Wh/kg although the voltage range was large (1.9V– 4V).[15] $VOPO_4$, with seven distinct polymorphs, was firstly systematically studied as Li^+ cathode by Azmi *et al*.[16] Although an approximately 4 V flat discharge potential were demonstrated in each phase, the cyclable capacities were far below its high theoretic capacity of ~160 mAh/g for one Li^+ cycling. Recently, Chen *et al*. demonstrated a novel multielectron cathode, disordered Li_2VO_2F, which can deliver up to ~1.8 Li^+ per transition metal (~420 mAh/g) at ~2.5V corresponding to a high gravimetric energy density of ~1000 Wh/kg.[17] Besides, it shows remarkable smooth voltage profile with no stepwise voltage gap and small increase in polarization. For multielectron NIB systems, $Na_3(VO_{1-x}PO_4)_2F_{1+2x}$ ($0 \leq x \leq 1$) was reported with high energy density (~520 Wh/kg) and good cycle life but with large voltage gap (~1.5V) due to $V^{3+} \leftrightarrow V^{5+}$ redox couples.[18] $Na_2CoFe(CN)_6$ was demonstrated with highly reversible two Na cycling (~150 mAh/g) and superior cyclability of 90 % over 200 cycles with reasonable voltage gap < 1V using both $Co^{2+} \leftrightarrow Co^{3+}$ and $Fe^{2+} \leftrightarrow Fe^{3+}$ redox couples.[19]

$Na_{1.5}VPO_{4.8}F_{0.7}$ was achieved with the highest energy density ~600 Wh/kg in NIB.[20] Besides, it showed excellent rate capability due to open two-dimensional diffusional framework and small volume change ~2.9%. Recently α_I-$VOPO_4$ was demonstrated as one of the most promising Na^+ cathodes with a high reversible capacity of ~110 mAh/g.[21] After incorporation of conductive graphene oxide, an impressive capacity of ~150 mAh/g was achieved.

1.3 Motivation and overview

The typical cathode used in today's rechargeable AIB operate on the transfer of a single-electron per transition metal, limiting achievable energy densities. Multi-electron polyanionic cathodes offer the potential to significantly increase energy densities by leveraging on the inductive effect of polyanion chemistries to increase voltage, and transfer of more than one electron per transition metal to increase capacity. In this thesis, we focus on the study of one of the most promising multi-electron cathode materials, $AVOPO_4$, using first-principles calculations. We aim to predict the thermodynamic stability, kinetics and provide insights to improve the electrochemical performance of $AVOPO_4$, as well as explain its experimental findings.

Project 1: Thermodynamics, Kinetics and Structural Evolution of ε-$LiVOPO_4$ over Multiple Lithium Intercalation. The majority of commercial cathodes today such as $LiFePO_4$ and $LiCoO_2$ operate on less than a single redox per transition metal, which limits capacities.[6] A potential path toward higher capacities is to develop multielectron cathodes that can reversibly cycle more than one electron per transition metal. Given ~4.5 V voltage limit of current commercial electrolytes stability, a previous high-throughput first-principles analysis has shown that only V and Mo have reasonable average voltages across multiple redox couples ($V^{3+} \rightarrow V^{5+}$ and $Mo^{3+} \rightarrow Mo^{6+}$) to be practical multielectron phosphate-based cathodes.[22] $VOPO_4$ is one of the promising multielectron cathode materials that can utilize $V^{3+} \rightarrow V^{5+}$ redox couples yielding a high

theoretical capacity of 305 mAh/g. However, the insertion/ deinsertion behaviors of the first and second Li exhibit differently which limits the reversible capacity.[23–25] In addition, there is disagreement over the number of intermediate phases in the low-voltage region.[23–25] In this project, we conduct joint first-principles calculations and experimental measurements to study the thermodynamics, kinetics, and structural evolution of ε-Li_xVOPO_4 over the entire lithiation range (x=0 ~ 2).

Project 2: Comparison of the polymorphs of $VOPO_4$ as multielectron cathodes for rechargeable alkali-ion batteries. One of the key differences between NIBs and LIBs is the alkali radii, which could affect the properties of structure. The electrochemical performance can be very different even with the same crystal framework and the performance of NIB may not be poorer than its Li counterpart. For example, Ong *et al*. found surprising evidence that the barriers for Na-ion migration can potentially be lower than that for Li-ion migration in the layered structures.[26] This is against the conventional belief that Na ion diffuses slower in the same host structures due to larger ionic size. Although the voltage of a sodium-ion cathode is generally ~0.5 V lower than that of its lithium counterpart, $VOPO_4$ remains a promising sodium-ion cathode with an expected high voltage of ~3.4 V yielding a high theoretical energy density of 258 mAh/g. Recently, one Na insertion into $VOPO_4$ phases are reported but there are still no studies for two Na insertions. In this thesis, we perform a combined first-principles and experimental study to evaluate the thermodynamic stability, voltage and diffusion kinetics for Li and Na intercalation in the β, ε and α_I polymorphs of $VOPO_4$.

Project 3: Rational Synthesis and Electrochemical Performance of $LiVOPO_4$ Polymorphs. Among the seven polymorphs of $VOPO_4$, α_I, β, and ε phases are the most well-studied as multi-electron Li-ion cathodes due to the promising electrochemical performances

demonstrated.[27,28] The α_I is the least reported among the various polymorphs due to difficulties in its synthesis. On the contrary, both the β and ε phases have been synthesized using a large plethora of methods, including hydrothermal,[29–31] solid-state,[31–33] and sol-gel.[32,34] We previously reported that α_I-$LiVOPO_4$ is metastable and β- and ε- $LiVOPO_4$ are stable with very similar thermodynamic stabilities. The close energies between β and ε phases might be one of the reasons for the observation of phase transformation between them in experiments.[34,35] However, this energetic degeneracy makes the obtainment of each pure phase, and hence optimization of electrochemical performance as well as direct comparisons between experiments and theories challenging. In this thesis, we synthesize the three phases using the same precursor, $LiVOPO_4 \cdot 2H_2O$, which is likely to minimize effects of synthesis on the properties such as stability and electrochemical performance. In addition, first-principles calculations are applied to study how O chemical potential affects $LiVOPO_4$ morphology and hence the electrochemical performance.

This thesis is divided into the following chapters:

- Chapter 2 presents a comprehensive analysis of the thermodynamics, kinetics, and structural evolution of ε-Li_xVOPO_4 over the entire lithiation range by combining first-principles prediction and experimental characterization.
- Chapter 3 presents a systematic first principles investigation, supported by careful electrochemical characterization and published experimental data, of the relative thermodynamic stability, voltage, band gap, and diffusion kinetics for alkali intercalation in β, ε and α_I polymorphs of $VOPO_4$.
- Chapter 4 presents a thorough study on the effects of temperature and atmosphere on the stability and formation of α_I-$LiVOPO_4$, β-$LiVOPO_4$ and ε-$LiVOPO_4$, using the same precursor, $LiVOPO_4 \cdot 2H_2O$. In addition, DFT surface calculations are applied to study the

effect of O chemical potential on $LiVOPO_4$ morphology and hence the electrochemical performance.

- Chapter 5 summarizes the key findings in this thesis and presents suggestions for future research.

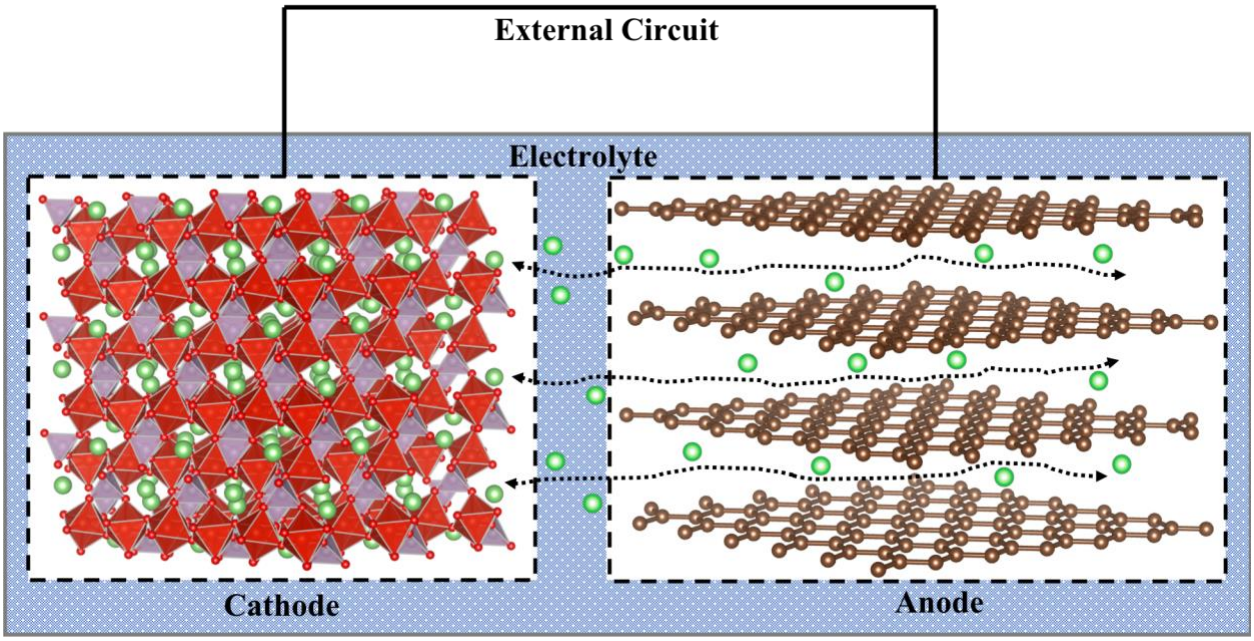

Figure 1.1 Schematic of the operation of alkali-ion battery.

Chapter 2. Thermodynamics, Kinetics and Structural Evolution of ε-$LiVOPO_4$ over Multiple Lithium Intercalation

2.1 Introduction

The rechargeable lithium-ion (Li-ion) battery[36–39] has become a dominant form of energy storage for the modern age. However, the energy densities, both gravimetric and volumetric, of today's Li-ion batteries are still far below that necessary to displace gasoline combustion engines. For example, the capacities of the layered $LiMO_2$ cathodes[38] which have the highest theoretical energy density of current commercial cathodes, are capped at around 180 mAh g^{-1}, leading to corresponding calculated energy densities of around 1 kWh kg^{-1} and 3 kWh L^{-1}.[40] Other commercial cathodes have significantly lower energy densities, e.g., the high rate $LiFePO_4$[39] cathode has maximum theoretical energy densities of 587 Wh kg^{-1} and 2 kWh L^{-1}. In commercial cells, the energy densities are even lower, the best not exceeding 250 Wh kg^{-1} and 0.6 kWh L^{-1}.[6]

The energy density of a cathode is given by the product of its voltage and its capacity. A push for high voltage reactions has motivated the strong interest in phosphate-based cathodes such as $LiFePO_4$ and $LiMnPO_4$ with increased voltage (relative to simple oxides) associated with the inductive effect of the PO_4^{3-} polyanion.[39] The majority of commercial cathodes today operate on a single redox per transition metal on average, which ultimately limits capacities. A potential path toward higher capacities is to develop multielectron cathodes that reversibly cycle more than one electron per transition metal. Given the fact that current organic carbonate electrolytes can only support voltages up to around 4.5 V,[41] a previous high-throughput first-principles analysis[22] has shown that only V and Mo have reasonable average voltages across multiple redox couples ($V^{3+} \rightarrow V^{5+}$ and $Mo^{3+} \rightarrow Mo^{6+}$) to be practical multielectron phosphate-based cathodes.

The vanadyl phosphates with formula $VOPO_4$ are an interesting class of multielectron cathode materials that utilize the $V^{3+} \leftrightarrow V^{4+} \leftrightarrow V^{5+}$ couple. Indeed, insertion of two Li into the ε polymorph of $VOPO_4$ has been demonstrated.[23–25,42] However, there are distinct differences between the insertion/deinsertion behaviors of the first and second Li. The insertion of the first Li at ~3–4.5 V[43] has been shown to be relatively facile and reversible with small overpotential. The insertion of the second Li, on the other hand, is associated with a much larger overpotential.[25] Although previous studies conclusively demonstrate that the first Li insertion takes place via a two-phase reaction, there is disagreement on the nature of the second Li insertion. Some works suggest the existence of several intermediate phases at ~ $Li_{1.5}VOPO_4$ and $Li_{1.75}VOPO_4$,[23,25] whereas Harrison *et al.*[24] suggest a single-phase region between $Li_{1.5}VOPO_4$ and Li_2VOPO_4.

In ε-Li_xVOPO_4, the VO_6 polyhedra share corners to form one-dimensional (1D) chains (see Figure 2.1) These chains are bridged by PO_4. All V ions are symmetrically equivalent in $VOPO_4$ (*Cc* spacegroup), whereas alternating V ions along the 1D chains are symmetrically inequivalent in $LiVOPO_4$ and Li_2VOPO_4 (*P*1 space group). It is only recently that a structure for the Li_2VOPO_4 end member has been proposed for a chemically lithated sample.[23,24] For historical reasons, the singly lithiated phase of ε-$VOPO_4$ is known as α-$LiVOPO_4$ based on the order of discovery. For the sake of clarity, we will adopt the convention proposed by Whittingham *et al.*[40] and refer to all lithiated members of ε-$VOPO_4$ with the ε prefix. Also, unless otherwise stated, formulas given without a prefix refer to the ε phase.

In this work, we demonstrate the stable cycling of more than one Li in solid-state-synthesized ε-$LiVOPO_4$ for more than 20 cycles for the first time. In contrast to previous work, we apply an integrated approach combining density functional theory (DFT) calculations, operando X-ray pair distribution function (PDF) and diffraction analysis, and extended X-ray

absorption fine structure (EXAFS) measurements to elucidate the thermodynamics, kinetics and structural evolution of ε-Li_xVOPO_4 over multiple Li intercalation. The main accomplishments include the identification of candidate stable structures for $Li_{1.5}VOPO_4$ and $Li_{1.75}VOPO_4$, the observation and explanation of a hysteretic V—O bond length evolution during low voltage cycling, and a discussion of the phase stability and ionic and electronic conductivity considerations in achieving good electrochemical performance in this material.

2.2 Experimental Methods

2.2.1 Synthesis

ε-$LiVOPO_4$ was prepared via solid state synthesis. Stoichiometric amounts of NH_4VO_3 (Aldrich, 99%), Li_2CO_3 (Fisher Scientific, ≥ 99%), and $NH_4H_2PO_4$ (Sigma-Aldrich, ≥ 99.99%) were mixed with acetone in a planetary ball mill for 4h. The isolated solid mixture was pressed into pellets and heated in argon atmosphere at 300 °C for 5h and then at 750 °C for 10h. The structure of the as-prepared material was verified using powder diffraction analysis and transmission electron microscopy (TEM). Nanocomposite ε-$LiVOPO_4$ was prepared by high energy ball-milling the as-synthesized material with Super P carbon black and PVDF (poly(vinylidene fluoride)) in a weight ratio of 75:15:10.

2.2.2 Electrochemistry

Electrodes were fabricated by casting the nanocomposite onto Al foil. Electrodes with 5–6 mg of active material of area 1.2 cm^2 were assembled into 2325-type coin cells with a Celgard 2400 separator (Hoechst Celanese), lithium metal foil (Aldrich) and liquid electrolyte (1 M $LiPF_6$ in 1:1 ethylene carbonate: dimethylcarbonate, EC:DMC). The thickness of the electrode was ~40 μm. The electrochemical properties were investigated using VMP multichannel potentiostat (Bio-Logic). Cells were cycled galvanostatically at C/50 (~0.01 mA/cm^2) in the high voltage (3.0–4.5

V), low-voltage (1.5–3.5 V) and whole voltage (1.6–4.5 V) regimes. Cells were also cycled at C/20 (~0.02 mA/cm^2) over the whole voltage range. The kinetics in the high- and low-voltage regimes were explored using GITT testing by applying C/50 current for 1.5 h followed by resting for 100 h at high voltage or 24 h at low voltage.

2.2.3 Operando Pair Distribution Function (PDF) and Diffraction Analysis

Operando X-ray scattering data were collected for ε-$LiVOPO_4$ based pellet electrodes within the AMPIX electrochemical cell.[44] 13 mm-diameter electrode pellets of 120–180 μm thick were prepared from the $LiVOPO_4$ nanocomposite as described previously. The electrode pellets were assembled into an electrochemical cell in an Ar-atmosphere glovebox with a glass fiber separator (Whatman GF/A), Li metal foil and liquid electrolyte (1 M $LiPF_6$ in 1:1 EC:DMC, from BASF). The cell was cycled galvanostatically at a constant current of 5 mA g^{-1}, in the voltage range of 3.5 V to 1.6 V to 3.5 V ($LiVOPO_4$ to Li_2VOPO_4 to $LiVOPO_4$).

X-ray scattering data were collected in 3 min exposures at beamline 11-ID-B at the Advanced Photon Source, Argonne National Laboratory, using high energy X-rays (~58 keV, λ = 0.2114 Å) in combination with a large amorphous-silicon based area detector (PerkinElmer). Data were collected at 15 min intervals alternating between PDF and pXRD optimized configurations (equivalent to 0.015 Li intervals for each) during the first lithiation and delithiation cycle. Total scattering data suitable for PDF analysis were collected to high values of momentum transfer (Q_{max} ~ 22 Å).[45,46] Diffraction data optimized for improved 2θ resolution were collected using a long sample-to-detector distance. The scattering images were reduced to one-dimensional data using fit2d.[47]

The large Q-range total scattering data were corrected for background scattering, Compton scattering and detector effects within pdfgetX2 and Fourier transformed to get $G(r)$, the PDF.[48]

Structure models were refined against the PDF data and the corresponding partial pair contributions to the PDFs calculated within PDFgui.[49] A spherical particle envelope parameter was used to model the particle size and/or length scale of ordering. The intensity and position of peaks corresponding to the V═O/P—O bond (ca. 2.0 Å) and the V—O bond (ca. 2.5 Å) were quantified by fitting Gaussian functions within fityk.[50] The evolution of the crystallographic lattice dimensions and average structure was evaluated based on Rietveld refinement of the powder diffraction data within TOPAS.

2.2.4 X-ray Absorption Spectroscopy

X-ray absorption data were collected for Li_xVOPO_4 electrodes recovered at different states of charge at beamline 9-BM-B of the Advanced Photon Source, Argonne National Laboratory. The V k-edge (E = 5.463 keV) XANES and EXAFS spectra were acquired in transmission mode. A k-range of 1–7 $Å^{-1}$ was used in the Fourier transformed R-space functions. Data were processed in Athena and Artemis from the Demeter software package version 0.9.21.[51]

2.2.5 XRD and TEM

High resolution X-ray synchrotron diffraction patterns were collected at beamlines X14A of National Synchrotron Light Source (NSLS) in Brookhaven National Laboratory (wavelengths 0.7801 Å) and 7B of APS (Advanced Photon Source) in Argon (wavelength 0.72775 Å). The Rietveld refinement of the X-ray diffraction patterns was done using the GSAS/EXPGUI package.

The morphology and particle sizes were first obtained by high resolution Scanning Electron Microscopy (SEM), ZeissSupra-55 field emission scanning electron microscope. Further transmission electron microscopy (TEM) characterization of the electrode particles was performed at Brookhaven National Laboratory. The powdered electrode sample was mixed in an alcohol solution in a small vial, and sonicated to ensure that the particles are well dispersed. The sample

was then drop-casted onto a lacey carbon TEM grid. The TEM images and selected area diffraction patterns (SAEDs) were obtained with a JEM-2100F (JEOL) operated at 200kV.

2.3 Computational Methods

All density functional theory (DFT) calculations were performed using the Vienna Ab initio Simulation Package (VASP)[52] within the projector augmented-wave approach.[53] Appropriate functionals and parameters for each analysis were selected based on accuracy and computational cost considerations. Initial candidate structures for ε-$VOPO_4$, $LiVOPO_4$ and Li_2VOPO_4 were obtained from the experimental literature.[23,54] Candidate intermediate structures Li_xVOPO_4 (x = 0.25, 0.5, 0.75, 1.25, 1.5 and 1.75) were derived by partially delithiating $LiVOPO_4$ or Li_2VOPO_4 and carrying out an enumeration[55] of all symmetrically distinct orderings. All analyses were performed using the Python Materials Genomics (pymatgen) library.[56]

2.3.1 Phase Equilibria and Voltage Profile

The energies of all Li_xVOPO_4 phases were calculated using the Perdew–Burke–Ernzerhof (PBE) generalized-gradient approximation[57] functional with the application of an effective Hubbard U[58–60] of 3.25 eV for vanadium (GGA+U). The calculation parameters were based on the parameters used in the Materials Project.[61] The key parameters are a plane wave energy cutoff of 520 eV and k-point density of at least 1000/(number of atoms in unit cell). All calculations were spin-polarized starting from a high-spin ferromagnetic configuration as a previous first-principles study has shown that the magnetic ordering has a small effect on the relative total energies in this system.[62] We assessed the phase stability of Li_xVOPO_4 by constructing the pseudobinary $VOPO_4$–Li_2VOPO_4 phase diagram, as well as the full Li–V–P–O quarternary phase diagram with data from the Materials Project.[63,64] The voltage profile was then constructed from the stable orderings.[65] We

also performed energy calculations using the screened hybrid Heyd–Scuseria–Ernzerhof (HSE) functional[66] to obtain more accurate structural parameters, electronic structure, and voltages. Given the much greater computational expense of HSE calculations, these calculations were limited to only the lowest energy orderings at each composition obtained from the GGA+*U* calculations.

We assessed the phase stability of Li_xVOPO_4 using two criteria.

- **Formation energies relative to end members.** We constructed the pseudo-binary $VOPO_4$ – Li_2VOPO_4 phase diagram by computing the formation energies $\Delta E(x)$ of Li_xVOPO_4 for $x = 0 - 2$ relative to the end members. $\Delta E(x)$ is given by the following equation:

$$\Delta E(x) = E(Li_xVOPO_4) - \frac{2-x}{2} \times E(VOPO_4) - \frac{x}{2} \times E(Li_2VOPO_4) \quad (1)$$

- **Comparison with all known phases in the Li-V-P-O system.** To determine how the thermodynamic stability of Li_xVOPO_4 changes with lithiation, we constructed the Li-V-P-O quarternary phase diagram.[64] The pre-computed energies of all Li-V-P-O phases were automatically queried using the Materials Project Application Programming Interface (API).[63]

We then added the Li_xVOPO_4 phases calculated in this study, and determined the energy above the convex hull, Ehull, of each phase of interest, which is a measure of the thermodynamic stability of a material at 0K. From the stable orderings along the lithiation path, we can calculate the average voltage for each adjacent pair of stable phases, $Li_{x_1}VOPO_4$ and $Li_{x_2}VOPO_4$ as follows:[65]

$$V = \frac{E(Li_{x_2}VOPO_4) - E(Li_{x_1}VOPO_4) - (x_2 - x_1)E(Li)}{(x_2 - x_1)\, e} \quad (2)$$

Where E is the total energy as calculated using DFT, and e is the absolute value of the electron charge.

2.3.2 Vacancy Migration Barriers

Activation barriers for vacancy (v_{Li}^{+}, a lower case *v* is used to denote a vacancy) migration in $LiVOPO_4$ were calculated using the climbing image nudged elastic band method (CI-NEB).[67,68] To avoid ambiguity regarding the localization of electrons, the standard PBE GGA functional (without application of the Hubbard *U*) was used, in line with the well-established practice in the literature.[69]The CI-NEB calculations were carried out using a 2 × 2 × 2 supercell with formula $Li_{31}V_{32}O_{32}P_{32}O_{128}$ (32 formula units with a Li vacancy) to minimize the interactions between periodic images. A Γ 1 × 1 × 1 *k*-point grid was used, and each image is relaxed until the forces on each atom are less than 0.02 eV/Å. Investigation of vacancy migration in Li_2VOPO_4 was not carried out as the introduction of a vacancy leads to a substantial rearrangement of Li atoms in the crystal due to the large number of Li atoms in the unit cell.

2.3.3 Electronic Conductivity

The electronic conductivity of Li_xVOPO_4 was assessed by calculating the band gaps and small polaron migration barriers using the HSE functional.[70,71] A slow moving electron or hole in a dielectric crystal induces a local lattice distortion, which acts as a potential well that causes the charge carrier to become self-trapped. The quasiparticle formed by the charge carrier and its self-induced distortion is called a small polaron if the range of the lattice distortion is of the order of the lattice constant. In this work, we adopted the same methodology used previously by one of the coauthors to study of polarons in the $LiMPO_4$ (M = Fe, Mn) olivines.[72] In Li_xVOPO_4, we can assume that electron transfer is confined within each 1D chain with no charge transfer through the PO_4 polyanions. The maximum barrier calculated for the charge to move from one V atom to its nearest periodic image along the chain is an upper limit for the migration barrier. In $VOPO_4$, polaronic charge carriers are electrons on V^{5+} sites. In $LiVOPO_4$, polaron charge carriers can either

be holes or electrons on V^{4+}, forming a localized V^{5+} or V^{3+} state, respectively. In Li_2VOPO_4, it is assumed that polaronic charge carriers are holes on V^{3+} sites given the fact that further reduction of V beyond a two-electron process has thus far not been demonstrated. The polaron migration barriers were calculated using a ferromagnetic structure. Supercells containing 16 formula units (2 × 1 × 2 for $VOPO_4$ and 2 × 2 × 1 for $LiVOPO_4$ and Li_2VOPO_4) were used to minimize the interaction between periodic images while keeping computational costs at a reasonable level. The HSE functional was used for the polaron calculations. Similar to the $LiMnPO_4$ olivine studied previously,[72] we found that a polaron cannot be localized in Li_xVOPO_4 with the GGA+*U* functional, likely due to the strong hybridization between V and O. A fairly tight energy convergence criteria of 0.001 eV was used, with a minimal Γ 1 × 1 × 1 *k*-point grid.

2.3.4 Small polaron migration

In this work, we adopted the same methodology used previously by one of the co-authors to study of polarons in the $LiMPO_4$ (M = Fe, Mn) olivines.[72] A hole (electron) polaron was formed on one of the transition metal ions by removing (adding) an electron to the fully relaxed Li_xVOPO_4 supercell. Overall charge neutrality was preserved via a compensating background charge. If $\{q_i\}$ and$\{q_f\}$ denote the initial and final ion positions respectively, the migration of the polaron can then be described by the transfer of the lattice distortion over a one-dimensional Born-Oppenheimer surface, with a energy maximum at a configuration between $\{q_i\}$ and $\{q_f\}$. To determine this maximum, we computed the energies for a set of cell configurations $\{q_x\}$ linearly interpolated between $\{q_i\}$ and $\{q_f\}$, i.e.,

$$\{q_x\} = (1-x)\{q_i\} + x\{q_f\} \text{ where } 0 \leq x \leq 1.$$

The polaron migration barriers were calculated using a ferromagnetic structure. Supercells containing 16 formula units (2×1×2 for $VOPO_4$ and 2×2×1 for $LiVOPO_4$ and Li_2VOPO_4) were

used to minimize the interaction between periodic images, while keeping computational costs at a reasonable level. The HSE functional was used for the polaron calculations. Similar to the $LiMnPO_4$ olivine studied previously,[72] we found that a polaron cannot be localized in Li_xVOPO_4 with the GGA+U functional, likely due to the strong hybridization between V and O. A fairly tight energy convergence criteria of 0.001 eV was used, with a minimal Γ 1×1×1 k-point grid.

2.4 Results

2.4.1 Electrochemistry of ε-$LiVOPO_4$

The first effort of this work was to optimize the solid state synthesis of ε-$LiVOPO_4$ as the method originally proposed by Ateba Mba *et al*. was for $LiVOPO_4F$.[73] NH_4VO_3 was used as a V^{5+} precursor, and pure ε-$LiVOPO_4$ was readily obtained at 750 °C. The high resolution X-ray diffraction pattern and TEM image of the as-synthesized and high energy ball-milled ε-$LiVOPO_4$ are given in Figure 2.2. After ball milling with super P carbon black, the micron-size as-synthesized $LiVOPO_4$ particles are fragmented, forming an agglomerate of smaller multigrained particles with a thin layer of carbon (thickness ∼2 nm) on the surface. The resulting clusters are less than 100 nm in size (see Figure 2.2e).

Figure 2.3a and b show the galvanostatic cycling of ball milled ε-$LiVOPO_4$ in the high- (3.0–4.5 V) and low-voltage (1.5–3.5 V) domains, respectively. The high-voltage $V^{4+/5+}$ plateau consistently delivers a reversible capacity of ∼105 mAh/g for up to 35 cycles, which corresponds to ∼0.65 Li. The charge–discharge profiles are similar after 25 cycles (insert of Figure 2.3a), but the initial charge curve is different. Electrolyte decomposition above 4.2 V leads to the initial capacity loss, as seen in Figure 2.3a These results are comparable with most previous reports on the cycling of $VOPO_4$ and $LiVOPO_4$.[24,53,74] In the low-voltage region, the capacity from the $V^{3+/4+}$ couple is close to 1 Li and stable for 25 cycles (see Figure 2.3b). The discharge–charge profiles

with steps are in agreement with many reports, suggesting the existence of intermediate phases at 1.5 and 1.75Li.[23,24,74] The inset of Figure 2.3b compares the curves of the 1st, 10th, 20th, and 25th cycles.

The cells were also cycled over the whole voltage range (1.6–4.5 V), as shown in Figure 2.3c and d. A high capacity of ~240 mAh/g can be achieved for up to 20 cycles, corresponding to 1.65 Li with little dependence of capacity on the rate. Both plateaus deliver a similar capacity as when cycled separately. From Figure 2.3e, we see that the profiles of C/50 cycling evolve from step-like to more slope-like, especially at low-voltage, and the difference between voltage plateaus increases progressively, suggesting changes in the local structure. At C/20, this effect is more pronounced. These observations clearly suggest inherent kinetic limitations, particularly in the high-voltage regime. Indeed, sluggish kinetics in the high-voltage regime have been recently considered responsible for pronounced Li gradients and reduced capacity in hydrothermally synthesized ε-$VOPO_4$.[75] Overall, the electrochemical performance is consistent with previous reports, indicating that it is easier to intercalate Li into than to remove Li from ε-$LiVOPO_4$. This is the first time cycling of multiple Li^+ in phosphates has been achieved for up to 20 cycles.

The kinetics in the high and low voltage regimes were explored using GITT testing. Figure 2.4a and b plot the capacity-voltage graph in the high- and low-voltage regions respectively, which is similar to the constant rate charge–discharge curves. The overpotentials and relaxation of the reactions in the high- and low-voltage plateaus in the green box are shown in Figure 2.4c. At low voltage, the discharge overpotential is ~32 mV, three times less than the high-voltage charge process (~108 mV), and is comparable to the high-voltage discharge process (~41 mV). This observation implies the intercalation process at high-voltage has to overcome a higher energy barrier than at low-voltage, which restricts the amount of lithium that can be reversibly extracted.

Electrolyte decomposition during high-voltage charging may further limit the amount of Li extracted. The transitions between V^{3+}/V^{4+} and V^{4+}/V^{5+}, where more energy is needed for nucleation, always manifest the highest overpotentials. The voltage at low plateau region is stable in 24 h, and 100 h relaxation is insufficient for the high-voltage reaction to reach equilibrium. These observations conclusively demonstrate the faster kinetics reaction at the low-voltage region, indicating that it is easier to intercalate Li into than to remove Li from ε-$LiVOPO_4$.

Figure 2.5a shows the 0 K pseudobinary $VOPO_4$–Li_2VOPO_4 phase diagram calculated using the GGA+*U* and screened hybrid HSE functionals. For $0 \leq x \leq 1$, the phase diagram predicts that there are no stable intermediate phases, consistent with the two-phase behavior observed in our high-voltage cycling (see Figure 2.3a) and previous results.[23,24,62,75] Two stable intermediate phases are predicted at $x = 1.5$ and 1.75 for $1 \leq x \leq 2$, which is again consistent with the three plateaus observed during low voltage cycling (see Figure 2.3b). We find that the average voltages calculated using the HSE functional are in much better agreement with experiments compared to those calculated using GGA+*U*, possibly due to a better description of the strongly hybridized V—O bonds and the fact that the Hubbard *U* value is a fitted average. Overall, we find that our computed HSE voltage profile is in fairly good agreement with the electrochemically measured profile (see Figure 2.3e) and values in the literature (see Table 2.1). This agreement gives us confidence that the intermediate structures obtained in our approach are reasonably close to the true ground state structures.

Figure 2.5b shows the calculated GGA+*U* E_{hull} relative to all known Li–V–P–O phases for the stable orderings in the $VOPO_4$–Li_2VOPO_4 pseudobinary. The E_{hull} is an estimate of the thermodynamic stability of a phase; stable phases have an E_{hull} of 0, whereas increasing E_{hull} indicates decreasing thermodynamic stability. We observe that although the E_{hull} remains relatively

low up to $x = 1$, it rapidly increases upon further lithiation, which indicates that highly lithiated Li_xVOPO_4 phases are thermodynamically unstable. All highly lithiated Li_xVOPO_4 are predicted to be unstable with respect to a linear combination of $Li_3V_2(PO_4)_3$, Li_3PO_4, and vanadium oxides.

Figure 2.6 shows the symmetrically distinct VO_6 environments extracted from the stable HSE-relaxed structures. In general, the HSE lattice parameters are in excellent agreement with the experimental lattice parameters[23] (see Table 2.2)As the atomic positions of the intermediate $Li_{1.5}VOPO_4$ and $Li_{1.75}VOPO_4$ phases have not been reported previously, the DFT relaxed positions are given in Table 2.3 and Table 2.4. In agreement with previous findings,[23,24] both the predicted $Li_{1.5}VOPO_4$ and $Li_{1.75}VOPO_4$ structures have $P\bar{1}$ symmetry, though the lowest energy $Li_{1.75}VOPO_4$ structure is a supercell that is twice the size of the primitive cell of Li_2VOPO_4. It is, however, likely that Li disorder is present in $Li_{1.75}VOPO_4$ given the presence of multiple orderings that are close in energy (and hence, potentially thermodynamically accessible at finite temperatures) to the ground-state ordering (see Figure 2.5a).

The calculated models of all intermediates were compared to the data collected for the ex-situ samples recovered from coin cells from electrochemical cycling and to the selected points of the operando data. Refinement of the lattice parameters (Figure 2.7) yielded a good fit for the long-range structure (beyond 15 Å), though significant deviations in the local structure remain. Further refinements of oxygen coordinates yielded excellent fits over all length scales (see Figure 2.8).

Partial pair contributions to the PDFs were calculated based on the refined model to identify the atom–atom pairs associated with different features in the experimental data (see Figure 2.9). The V has an asymmetric coordination environment, with one short V—O bond (1.62 Å) and five longer V—O bonds (~1.99 Å). In the total PDF, the short V—O bond at ~1.6 Å overlaps with

the contribution from the P—O distance within the PO_4^{3-} anion. These bond lengths are in excellent agreement with the HSE-relaxed VO_6 environments for $LiVOPO_4$.

The operando PDF data, collected during lithiation and delithiation between $x = 1$ and $x = 2$, revealed marked changes in the local atomic structure and V coordination (Figure 2.10a). Continuous shifts in the 1.6 and 2.0 Å peak positions reflect changes in the average bond lengths, whereas the changes in peak areas correspond to changes in the average coordination number. Discontinuous changes were observed for the peak at ~3.3 Å, corresponding to the V(—O—)P distance. This likely reflects changes in the V—O—P angle associated with a relative rotations of the VO_6 and PO_4 polyhedra during the structural phase transitions. The changes in the local structure were quantified by fitting Gaussian functions to features in the PDFs up to 4 Å. Although the contributions from the P—O and short V—O bonds are not well resolved in the operando data, the PO_4 polyatomic anion geometry is not expected to change during cycling, so all changes in the feature at ca. 1.6 Å can be entirely attributed to changes in the V═O bond. The intensity and position of the feature associated with the P—O bond was fixed for the analysis.

More pronounced changes were observed for the V═O bond length compared to the V—O bond (Figure 2.10b). During the initial stage of reaction, corresponding to the transition between $LiVOPO_4$ and $Li_{1.5}VOPO_4$, the short terminal V═O bonds elongate rapidly by 0.15 Å, whereas longer V—O interactions increase only by 0.008 Å. The elongation of the V═O bond is accompanied by a decrease in the relative intensity of this peak and a small, but not equivalent, increase in the intensity of the V—O feature at 2.0 Å. Once the V═O correlations are effectively eliminated, the longer V—O bond grows more rapidly. The average V—O bond lengthens most rapidly between $Li_{1.5}VOPO_4$ and $Li_{1.75}VOPO_4$ (2.014 Å to 2.026 Å), with slower changes again between $Li_{1.75}VOPO_4$ and Li_2VOPO_4 (2.026 Å to 2.034 Å). The intensity weighted average of V—

O distance changes more continuously. The overall changes in V—O distance are reversed upon delithiation. These observations are consistent between the PDF measurements and the DFT computed structures (Figure 2.6).

Clear hysteresis is observed for the V—O features between lithiation and delithiation (Figure 2.11a). The V—O bond contracts more rapidly during delithiation compared to the elongation during lithiation. Correspondingly, stable intermediates appear to form ~0.1 Li earlier during delithiation than during lithiation ($Li_{1.6}VOPO_4$ vs $Li_{1.5}VOPO_4$) as is reflected by the relevant plateaus in the electrochemistry. The hysteresis within each V—O bond is noticeable throughout the entire composition range. The shorter V interactions exhibit large hysteresis associated with only the first $Li_{1.5–1.6}VOPO_4$ intermediate.

The V—O coordination number for V—O bonds of less than ~2.2 Å drops during the reaction (Figure 2.11b), which reflects either under-coordination of V or the formation of a long ~2.4 Å V—O bond. The initial V local environment has 1 short V═O and 5 longer V—O correlations on average. During the transformation from $LiVOPO_4$ to $Li_{1.5}VOPO_4$, the total intensity in the V—O features at 1.6 and 2.0 Å reduces from 6 to 5.5 O neighbors, suggesting that up to half of the V have an elongated V—O bond. This is supported by an increase in intensity for the features at 2.5 and 2.8 Å, which are primarily assigned to O—O distances. During charge, the V—O coordination drops to 5.5 beyond 1.75 Li, but this is not reversed by 1 Li.

The local V coordination environment for a set of ex-situ samples was determined via EXAFS. The Fourier transformed k^2 weighted data is plotted (offset for clarity) in Figure 2.12a. The peak around 1.5 Å is associated with the first coordination shell around the central absorbing atom. First coordination shell fits were performed using a model for the VO_6 octahedron, which included long and short apical bonds (created by displacing the central V along the *z* axis) as well

as four equivalent equatorial bonds. Bond lengths were determined by fitting unique ΔR values for all scattering paths and all samples. Coordination number (N) and amplitude reduction (S_0^2) were taken to be constant. A single Debye–Waller factor (σ^2) and energy shift (E_0) were used for all scattering paths and samples. Consistent with the PDF analysis, we identify a short and equatorial V—O radial distance at ~1.6 and 2.0 Å respectively. The presence of a long bond around 2.4–2.5 Å is also apparent from Figure 2.12c. The long bond length increases with increasing state of discharge and then recovers (with a clear overpotential) upon recharge. The observation of a long V—O bond length at ~2.4 Å in our PDF and EXAFS measurements is consistent with previous EXAFS results by Allen *et al.*[74]

2.4.2 Ionic Conductivity

We investigated the migration barriers for v_{Li+} hopping in $LiVOPO_4$ using CI-NEB calculations. The unit cell of $LiVOPO_4$ contains two crystallographically distinct Li sites (labeled Li1 and Li2) that form percolating 1D chains, as shown in Figure 2.13. We investigated all hops between nearest neighbor Li sites (A → B, B → C, D → E, E → F, A → G and A → H, see Figure 2.13a for labeling scheme). The results are shown in Figure 2.14.

For the 1D path A → B → C, both hops A → B and B → C involve the migration through the space between two VO_6 octahedra, resulting in fairly similar activation barriers of 244 and 214 meV respectively. For the 1D path D → E → F on the other hand, the migration local environments are extremely different for hops D → E and E → F. The D → E hop takes place through two VO_6 octahedra (similar to hops A → B and B → C), but the much smaller channel size results in a significantly higher migration barrier of 600 meV. Unlike the previous hops, the E → F hop passes through two PO_4 tetrahedra instead of VO_6 octahedra. In fact, the midpoint of E → F hop is found to be lower in energy than the end points, which we attribute to a reduction in the electrostatic

repulsion between nearest neighbor Li^+ with the introduction of a vacancy. Overall, we find that the effective migration barriers (across the entirety of each path) for the Li1 (A → B → C) and Li2 (D → E → F) paths are 244 and 703 meV respectively. This suggests that v_{Li+} migration is likely to be relatively facile at least along the Li1 1D chains. Interchain vacancy migration barriers (A → G and A → H) are found to be significantly higher at 815 and 1199 meV.

We may estimate the diffusion coefficient D of $LiVOPO_4$ using transition-state theory as follows: $D = a^2 \times \upsilon \times \exp(-E_a/k_BT)$ (1) where a is the length of a diffusion jump, υ is the attempt frequency, E_a is the activation energy, and k_BT is Boltzmann's constant times the temperature.[76] Using a typical phonon frequency of 10^{12} Hz, the diffusion coefficient at 300 K for $LiVOPO_4$ in the dilute limit is estimated to be 6.73×10^{-8} cm^2 s^{-1} (based on the lowest activation energy 1D channel), which is in relatively good agreement with the lithium chemical coefficient obtained from GITT or electrochemical impedance spectroscopy measurements (10^{-10} to 10^{-9} cm^2 s^{-1}).[42]

2.4.3 Electronic Conductivity

The calculated densities of states (DOSs) of Li_xVOPO_4 are shown in Figure 2.15. We find that all Li_xVOPO_4 phases have a fairly large band gap (2.25–2.99 eV), though the band gap decreases with increasing lithiation. The calculated band gap of $LiVOPO_4$ (2.63 eV) is comparable with previous experimental measurements and theoretical calculations (2.13 and 2.78 eV respectively).[77]

Figure 2.16 summarizes the calculated migration barriers for the various polarons in Li_xVOPO_4 and provides a comparison to polaron migration barriers previously calculated for the olivine $LiFePO_4$ and $LiMnPO_4$ cathode materials[72] using the same computational methodology. In

general, we find that the polaron migration barriers in the Li_xVOPO_4 to be higher than those in $LiFePO_4$ and comparable to those in $LiMnPO_4$.

2.5 Discussion

ε-$VOPO_4$ is a highly promising cathode material due to its potential ability to intercalate two Li per vanadium to achieve a very high theoretical capacity of 318 mAh g^{-1}.[23–25,42] In contrast to previous efforts, we have demonstrated in this work the stable cycling of solid-state synthesized ε-$LiVOPO_4$ over more than one Li for more than 20 cycles. Furthermore, our combined DFT, operando PDF, and EXAFS analysis have yielded new insights into the thermodynamic and kinetic factors influencing the electrochemical performance in this material.

In general, the electrochemical performance obtained in this work is consistent with the earlier reports.[23,24,42,78] The discharge–charge profiles, with steps at ∼3.9, 2.5, 2.2, and 2.0 V, suggest the existence of intermediate phases at x = 1.5 and 1.75. It should be noted that there is some minor disagreement on the low voltage regime in the experimental literature. Although previous works[23,24,78] agree on the existence of an intermediate phase at x = 1.5, these works disagree on whether there is a second intermediate phase at x = 1.75,[23,78] or a solid solution regime for $1.5 \leq x \leq 2$.[24] Our results support the former findings, though the x = 1.75 phase is only slightly below the tie-line formed by the $Li_{1.5}VOPO_4$ and Li_2VOPO_4 phases.

From our electrochemical cycling data in Figure 2.3, we may make the observation that it is somewhat easier to intercalate Li into $LiVOPO_4$ than to remove Li from $LiVOPO_4$. However, intercalation of Li into $LiVOPO_4$ is associated with increasing polarization with cycling. Our results suggest that the limitation in extracting Li from $LiVOPO_4$ at high voltage is kinetic in nature, whereas the increasing polarization during intercalation at low voltage is probably due to thermodynamically driven structural changes.

From NEB calculations, we find that $LiVOPO_4$ is a pseudo-1D vacancy diffuser, with much lower effective migration barriers for the Li1 path (244 meV) than for the Li2 path (703 meV). The barriers for the Li1 path are also significantly lower than the Li migration barriers in the charged $VOPO_4$ material (463 meV) calculated by Mueller *et al.*[69] This suggests that (a) initial extraction of Li is likely to take place from the Li1 channel, and (b) there may be asymmetry in the kinetics between charge and discharge for $0 \leq x \leq 1$. This observation is consistent with the results of our GITT measurements, which find much lower overpotentials for high-voltage discharge compared to high-voltage charging. It could account for why full extraction of Li from $LiVOPO_4$ is difficult, as well as the larger polarization observed at the end of charge in most experiments.[23,25,42] It should be noted that the computed vacancy migration barriers in this work are different from those recently calculated by Ling *et al.*,[62] who concluded that vacancy migration in $LiVOPO_4$ follows a 2D network. However, as noted by the authors themselves, the relaxed $LiVOPO_4$ structure in Ling *et al.*[62] swork shows significant deviation from the experimental structure, and their GGA+*U* NEB migration barriers are for a combination of ionic and electron migration.

The DFT calculations, PDF and EXAFS analysis provide strong evidence of thermodynamically driven structural changes during Li insertion into $LiVOPO_4$. First, the DFT calculated phase diagram show that the Li_xVOPO_4 phases are highly unstable for $x > 1$, with E_{hull} as high as 81 meV per atom for the Li_2VOPO_4 end member. Second, operando PDF and EXAFS data show evidence of a clear hysteresis in VO_6 local environments during low-voltage cycling. In particular, an irreversible increase in a V—O long bond at >2.4 Å is observed. The long V—O bond at >2.4 Å found in both PDF and EXAFS local structure analysis of the cycled samples, as well as in a previous EXAFS study by Allen *et al.*,[74] but it is not reflected in the VO_6 environments

of the DFT-relaxed or experimentally derived Li_xVOPO_4 structures. VO_6 environments with a long V—O bond close to that observed (>2.3 Å) are known for $HVOPO_4$, which shares the same VO_6—PO_4 connectivity as ε-Li_xVOPO_4.[79] DFT relaxations of both $HVOPO_4$ and H_2VOPO_4 derived by substituting H for Li in $LiVOPO_4$ and Li_2VOPO_4, respectively, also show a significant extension in certain V—O bond lengths. Accordingly, we speculate that the observed >2.4 Å V—O bond is associated with H incorporation into the Li_xVOPO_4 structure, perhaps as a H/Li solid solution. Hydride formation is known to occur for V-based catalysts in organic solution.[80,81] Here, we believe the H likely results from electrolyte decomposition. A recent detailed study of the thermal stability of cathodes by some of the authors provides strong evidence that the charged $VOPO_4$ tends to oxidize the electrolyte to form H_xVOPO_4.[82] The structural distortions resulting from this H incorporation may provide an explanation for the increasing polarization during cycling. The investigation of this hypothesis will be the subject of future work.

The DFT results on the ionic and electronic conductivity in Li_xVOPO_4 emphasize the importance of nanosizing and carbon coating in achieving good electrochemical performance. The pseudo-1D nature of the diffusion pathways in Li_xVOPO_4 (this work and the work of Mueller *et al.*[69]), similar to the olivine Li_xMPO_4 cathodes,[83,84] makes nanosizing crucial for maintaining facile Li conduction, given the fact that inevitable channel blocking defects at the macroscopic limit would limit the conductivity in 1D diffusers.[85] We also find Li_xVOPO_4 to be a large band gap insulator throughout the entire lithiation range, and calculated polaron migration barriers are similar to those in the olivine $LiMPO_4$ systems. Therefore, carbon-coating and nanosizing are essential for electronic conductivity as well.[82,86–89] It should be noted that this result is contrary to the previous measurements of Song *et al.*,[42] who found $VOPO_4$ (10^{-6} S cm^{-1}) to have a much higher electronic conductivity compared to $LiFePO_4$ (10^{-8}–10^{-10} S cm^{-1}).[51,90,91] It is our wish that future

experiments into the electronic conductivity across different states of charge, especially for the $x = 1$ and $x = 2$ end members, would be carried out to more conclusively verify the first-principles predictions and previous experimental results.

2.6 Conclusion

To conclude, we have demonstrated that solid-state synthesized $LiVOPO_4$ can be stably cycled over 1.65 Li for more than 20 cycles. About 65% of the theoretical capacity was achieved during delithiation from $LiVOPO_4$ to $VOPO_4$ in the high-voltage regime, whereas almost 100% of theoretical capacity was obtained during lithiation of $LiVOPO_4$ to Li_2VOPO_4 in the low-voltage regime, albeit with increasing polarization. Using a combination of DFT calculations, GITT measurements, operando PDF analysis and EXAFS spectra, we show that the capacity limitations during delithiation is likely to be driven by Li mobility limitations, whereas the increasing polarization during lithiation is the result of structural changes. We also show that Li_xVOPO_4 is likely to be a pseudo-1D ionic conductor with low electronic conductivity, for which nanosizing and carbon coating is essential to achieve good electrochemical performance.

Chapter 2 is, in full, a reprint of the material "Thermodynamics, Kinetics and Structural Evolution of ε-$LiVOPO_4$ over Multiple Lithium Intercalation" as it appears in Chemistry of Materials, Y.-C. Lin, B. Wen, K. M. Wiaderek, S. Sallis, H. Liu, S. H. Lapidus, O. J. Borkiewicz, N. F. Quackenbush, N. A. Chernova, K. Karki, F. Omenya, P. J. Chupas, L. F. J. Piper, M. S. Whittingham, K. W. Chapman and S. P. Ong, 2016, 28, 1794–1805. The dissertation author was the primary investigator and author of this paper. All calculations and corresponding data analysis were done by the author. The experimental portion of the work – synthesis, characterization and data analysis were done by collaborators, B. Wen, K. M. Wiaderek, S. Sallis, H. Liu, S. H. Lapidus, O. J. Borkiewicz, N. F. Quackenbush, K. Karki, F. Omenya, P. J. Chupas.

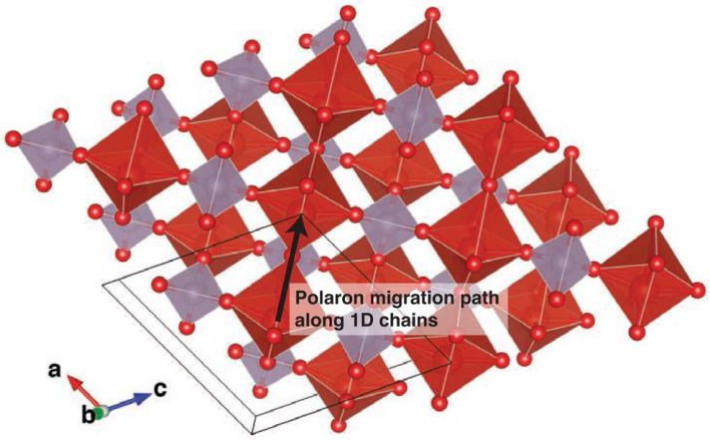

Figure 2.1 Crystal structure of $VOPO_4$, showing polaron migration along 1D VO_6 chains.

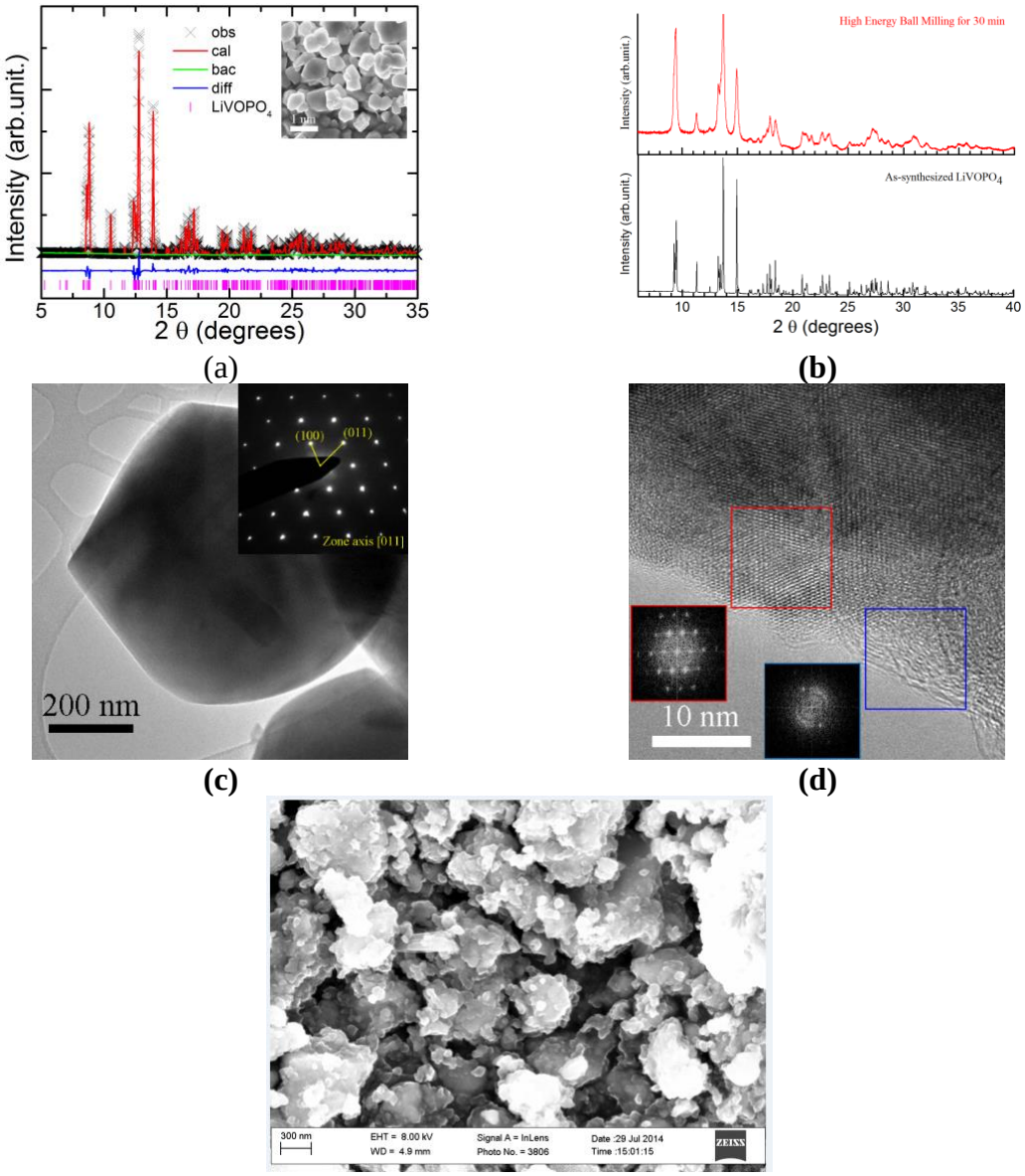

Figure 2.2 (a) High-resolution X-ray diffraction pattern of ε-$LiVOPO_4$ (wavelength λ=0.72775 Å); (b) High resolution X-ray diffraction patterns of as-synthesized and high energy ball milled ε-$LiVOPO_4$ (wavelength λ = 0.78013 Å); (c) TEM image of ε-$LiVOPO_4$ Particles.

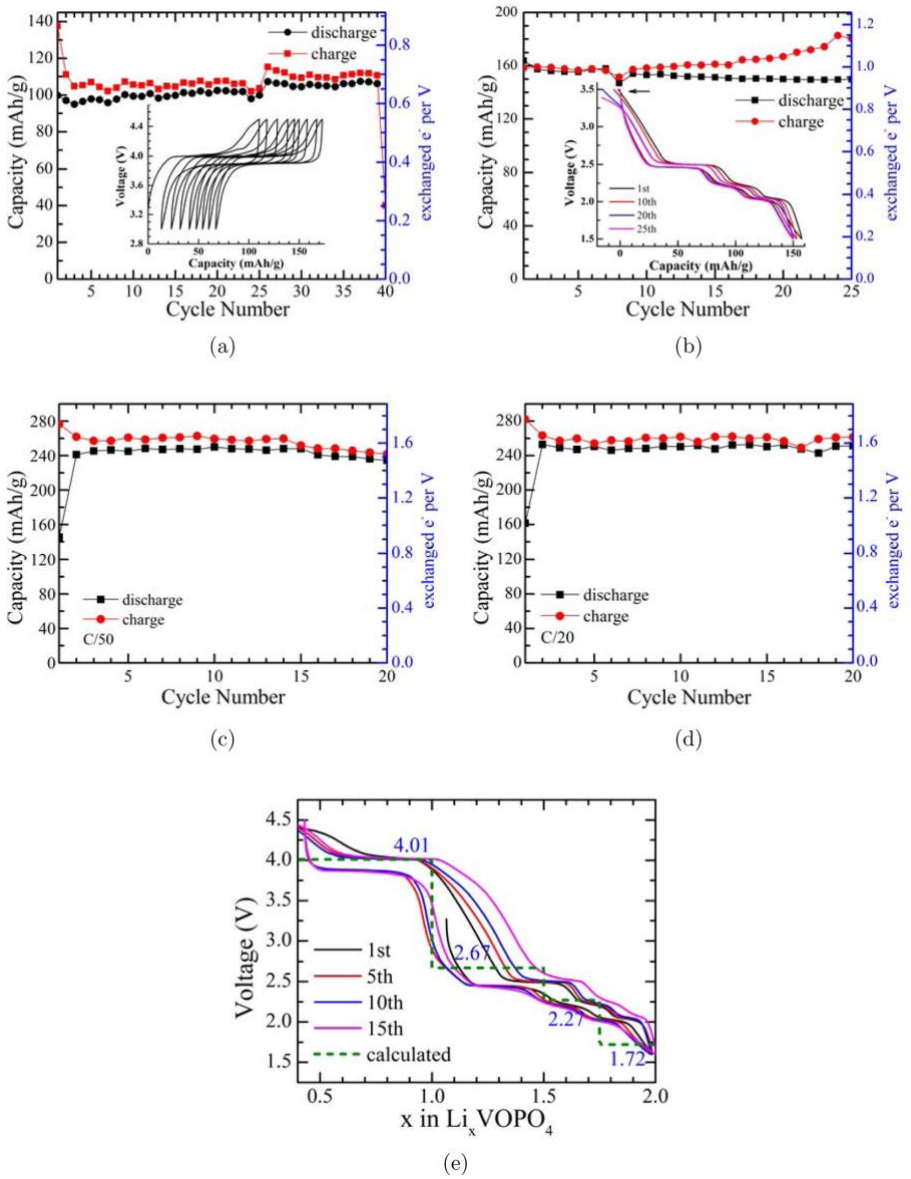

Figure 2.3 Galvanostatic charge–discharge cycling of ε-LiVOPO$_4$: (a) high voltage cycling within 3–4.5 V (C/50) and (b) low voltage cycling in the range of 1.5–3.5 V (C/50). Two lithium cycling from 1.6 to 4.5 V (c) at C/50 and (d) C/20 (1C = 159 mA/g); (e) Comparison between experimental voltage curve at 50C and HSE calculated voltage profile.

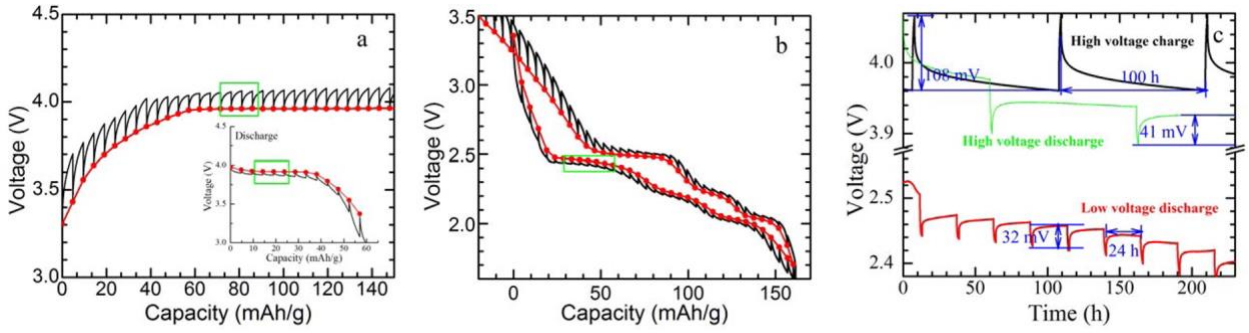

(a) (b) (c)

Figure 2.4 GITT capacity-voltage profiles of ε-$LiVOPO_4$ in the (a) high voltage and (b) low-voltage domains. (c) Voltage vs time graph of the magnified marked region. C/50 current was applied for 1.5 h before rest; 24 h relaxing for low voltage and 100 h for high voltage.

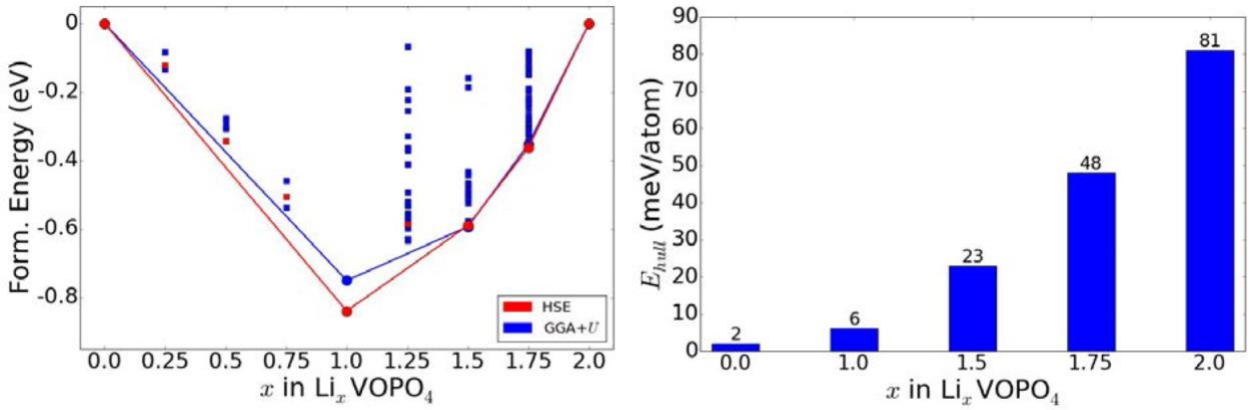

(a) $VOPO_4$-Li_2VOPO_4 phase diagram (b) Energies above convex hull for Li_xVOPO_4

Figure 2.5 (a) Calculated pseudobinary $VOPO_4$–Li_2VOPO_4 phase diagram using the HSE (blue) and GGA+U (green) functionals. Squares, unstable structures; circles, stable structures; lines, convex hull. (b) Calculated energies above the convex hull for stable orderingsin the pseudobinary $VOPO_4$–Li_2VOPO_4 system in GGA+*U*. The convex hull is calculated withrespect to all phases in the full Li–V–P–O calculated phase diagram.

Table 2.1 Comparison of calculated and experiment voltage steps for Li_xVOPO_4.

	Average Voltage (V)			
Voltage step $(x_1 - x_2)$	GGA+U	HSE	Expt.	Literature
0 – 1	3.80	4.01	3.80 – 4.50	6 – 12
1 – 1.5	2.73	2.67	2.37 – 2.50	7 – 9
1.5 – 1.75	2.08	2.27	2.18 – 2.24	7 – 9
1.75 – 2	1.63	1.72	1.89 – 2.04	7 – 9

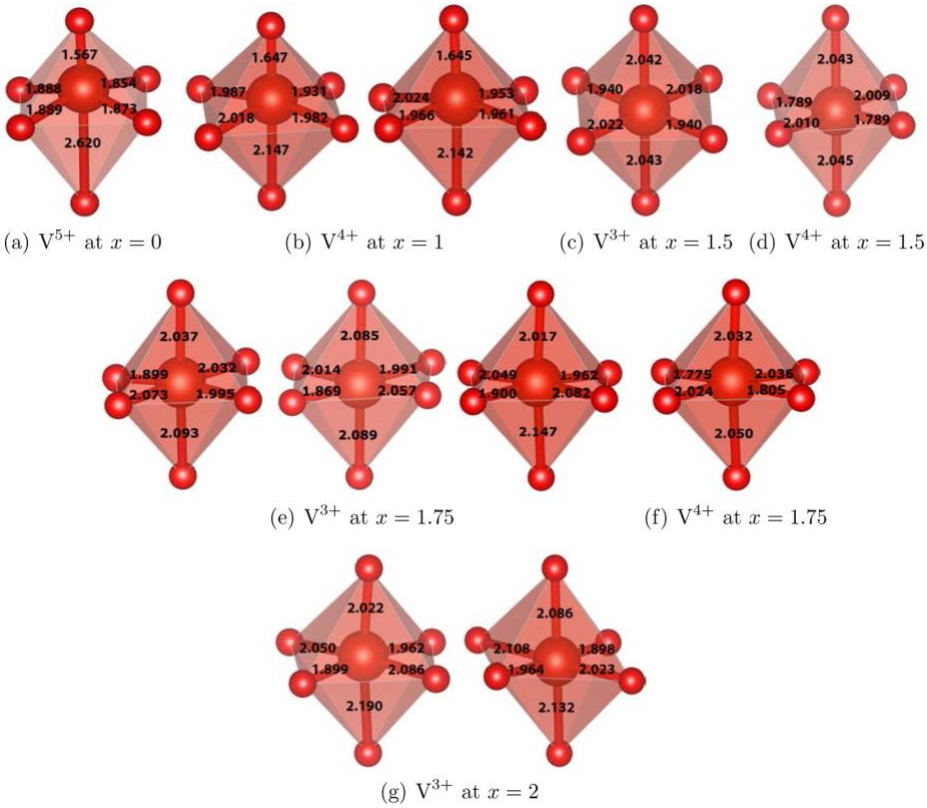

Figure 2.6 Symmetrically distinct VO_6 local environments in Li_xVOPO_4 from structures relaxed using HSE calculations. Large sphere: vanadium ion. Small sphere: oxygen ion.

Table 2.2 Comparison of calculated lattice parameters of stable Li_xVOPO_4 structures with the experimental lattice parameters.

x		a (Å)	b (Å)	c (Å)	α (°)	β (°)	γ (°)	Volume (Å^3)
0	Exp.	7.266	6.893	7.265	90.00	115.30	90.00	329.10
	GGA+*U*	7.344	7.067	7.388	90.00	115.29	90.00	346.71
	% Diff	1.08	2.53	1.69	0.00	0.00	0.00	5.35
	HSE	7.246	6.966	7.308	90.00	114.62	90.00	335.36
	% Diff	-0.27	1.06	0.60	0.00	-0.59	0.00	1.90
1	Exp.	6.734	7.196	7.918	89.81	91.27	116.91	342.04
	GGA+*U*	6.952	7.150	7.954	89.80	91.30	116.66	353.28
	% Diff	3.24	-0.63	0.46	-0.01	0.03	-0.22	3.29
	HSE	6.870	7.159	7.825	89.79	91.31	117.24	342.06
	% Diff	2.02	-0.52	-1.17	-0.02	0.03	0.28	0.01
1.5	Exp.	6.982	6.992	7.789	89.57	89.90	115.72	342.54
	GGA+*U*	7.106	7.055	7.919	89.42	89.73	115.53	358.15
	% Diff	1.77	0.89	1.67	-0.17	-0.19	-0.16	4.56
	HSE	6.968	7.014	7.770	89.65	89.08	116.22	340.58
	% Diff	-0.21	0.31	-0.23	0.09	-0.91	0.43	-0.57
1.75	Exp.	7.100	7.044	7.783	89.81	89.75	116.01	349.82
	GGA+*U*	7.140	7.189	7.921	89.59	89.51	116.18	364.80
	% Diff	0.55	2.05	1.78	-0.25	-0.27	0.15	4.28
	HSE	7.041	7.104	7.796	89.72	89.47	116.21	349.83
	% Diff	-0.83	0.85	0.17	-0.10	-0.32	0.17	0.00
2	Exp.	7.195	7.101	7.775	89.82	89.79	116.34	356.00
	GGA+*U*	7.333	7.196	7.853	89.54	89.91	116.24	371.65
	% Diff	1.92	1.34	0.99	-0.31	0.13	-0.09	4.40
	HSE	7.250	7.106	7.714	89.68	90.01	116.34	356.16
	% Diff	0.77	0.07	-0.79	-0.19	0.25	0.00	0.04

Table 2.3 HSE-relaxed atomic coordinates of $Li_{1.5}VOPO_4$.

Atom	*x*	*y*	*z*
Li	0.1716	0.6556	0.0631
Li	0.1756	0.1532	0.5621
Li	0.5000	0.0000	0.0000
Li	0.5000	0.5000	0.5000
V	0.4999	0.7500	0.7502
V	0.0000	0.7501	0.7500
P	0.2445	0.7670	0.3923
P	0.2445	0.2670	0.8922
O	0.9061	0.9399	0.1985
O	0.2511	0.2750	0.3331
O	0.5839	0.2614	0.5013
O	0.7488	0.2241	0.1666
O	0.3441	0.9255	0.2463
O	0.0939	0.5598	0.3019
O	0.1178	0.8472	0.5104
O	0.3448	0.4256	0.7465
O	0.4155	0.2380	0.9988
O	0. 1175	0. 3470	0. 0101

Table 2.4 HSE-relaxed atomic coordinates of $Li_{1.75}VOPO_4$.

Atom	*x*	*y*	*z*
Li	0.8973	0.2981	0.7654
Li	0.3684	0.7852	0.2660
Li	0.4911	0.3519	0.0948
Li	0.4207	0.8571	0.7101
Li	0.8546	0.2819	0.2717
Li	0.7878	0.7586	0.7385
Li	0.7265	0.7442	0.2608
V	0.7507	0.7519	0.0051
V	0.2543	0.2557	0.4907
V	0.9983	0.9972	0.2503
V	0.4960	0.5002	0.7440
P	0.8138	0.4379	0.9571
P	0.3119	0.9340	0.4510
P	0.3074	0.9338	0.9549
P	0.8132	0.4335	0.4579
O	0.7351	0.3902	0.6199
O	0.2143	0.8893	0.1152
O	0.5123	0.8317	0.9176
O	0.0150	0.3328	0.4126
O	0.9015	0.8464	0.3290
O	0.4030	0.3340	0.8239
O	0.3199	0.5838	0.6130
O	0.8074	0.0852	0.1291
O	0.3219	0.0852	0.9099
O	0.8281	0.5864	0.4127
O	0.6635	0.4242	0.8957
O	0.1854	0.9165	0.3757
O	0.6665	0.9147	0.5967
O	0.1833	0.4066	0.0906
O	0.0110	0.3385	0.9062
O	0.5144	0.8314	0.4162
O	0.7349	0.3948	0.1173
O	0.2222	0.8972	0.6118
O	0.9095	0.8468	0.8222
O	0.4122	0.3289	0.3103

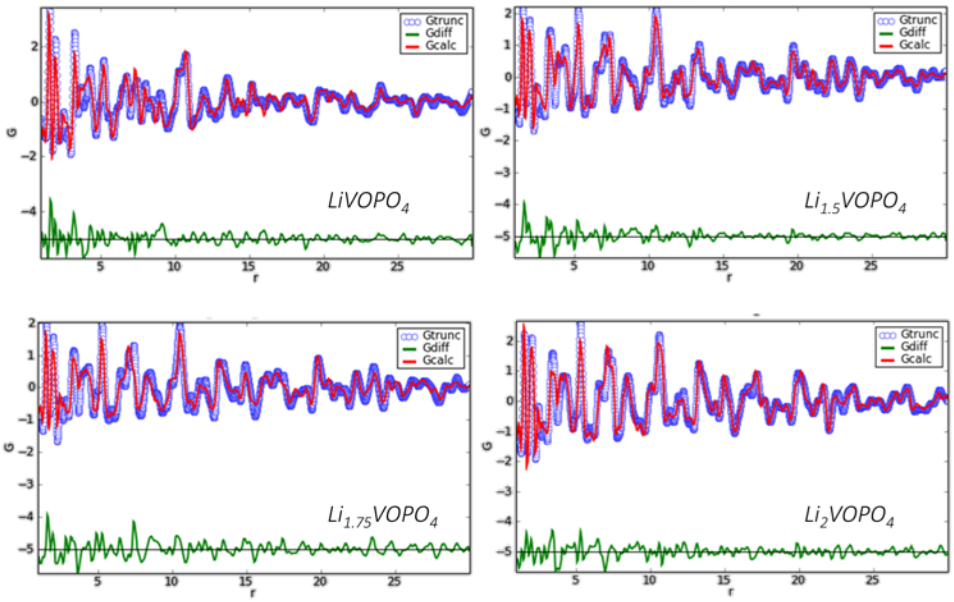

Figure 2.7 Refinements of all Li_xVOPO_4 based on the calculated structures, lattice parameters refined, atomic positions fixed.

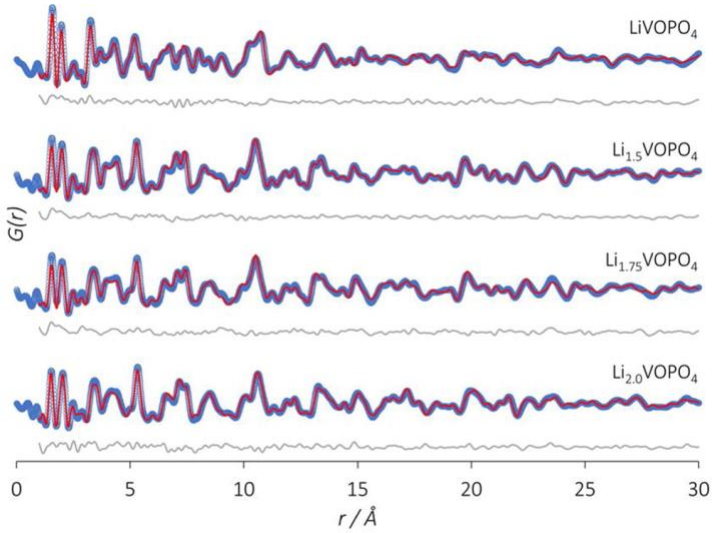

Figure 2.8 Refinements of all intermediates based on the HSE-relaxed structures, lattice parameters, and oxygen atomic positions.

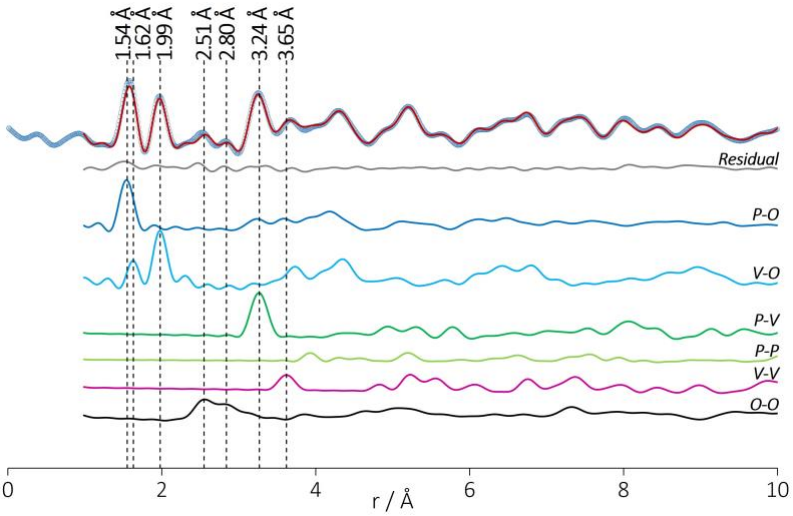

Figure 2.9 Structural model of $LiVOPO_4$.

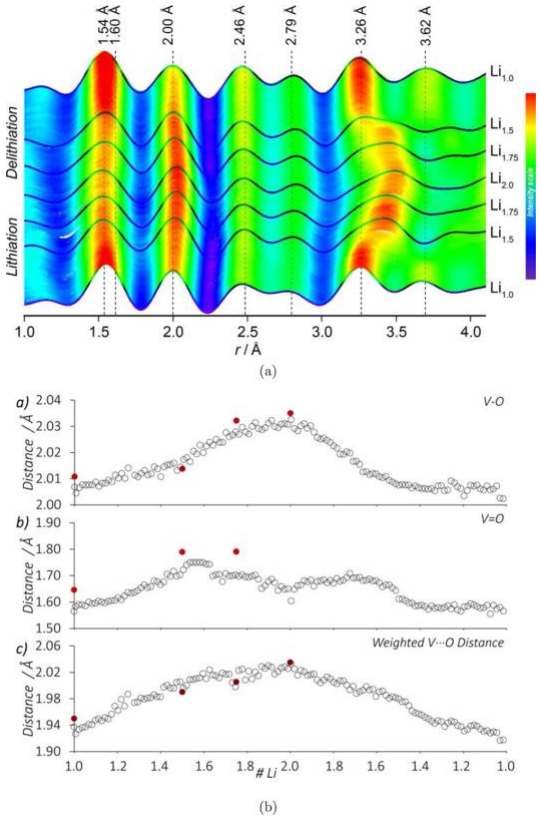

Figure 2.10 (a) Operando PDF data obtained during cycling of $LiVOPO_4$ in the range 3.5–1.6–3.5 V. (b) Peak positions corresponding to the V—O and V═O bonds, and the intensity-weighted average value. Experimental data, open markers; HSE calculated distances, red closed markers.

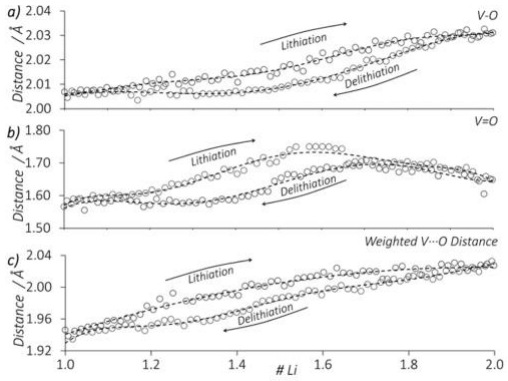

(a) Local V environment changes.

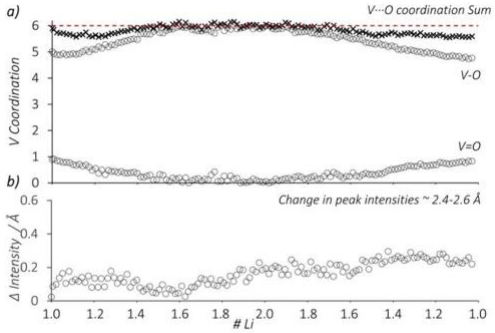

(b) Average coordination number of V based on the intensity of selected peaks within the PDFs.

Figure 2.11 Changes in V—O bond lengths and coordination showing hysteresis during lithiation and delithiation.

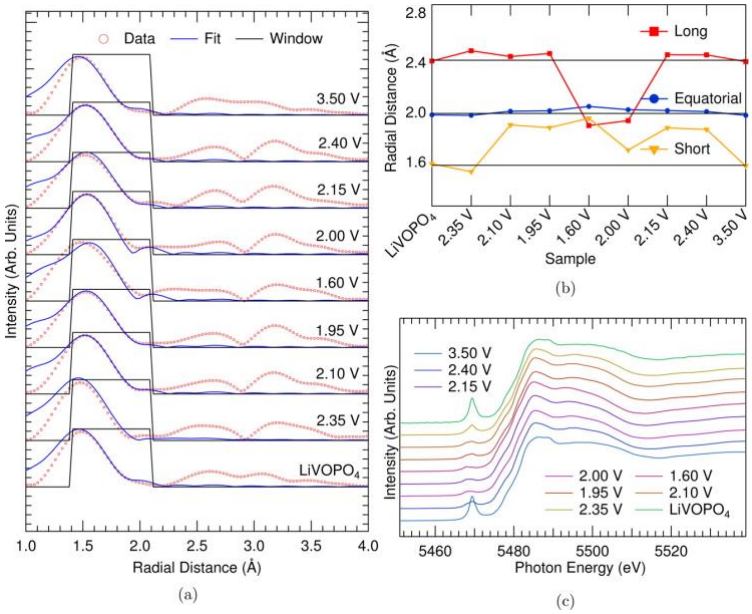

Figure 2.12 EXAFS analysis of ex-situ $LiVOPO_4$ cathodes at various states of charge. (a) First shell fits using an asymmetric model for the VO_6 octahedron including long and short apical bonds, and four equivalent equatorial bonds. (b) V—O bond lengths at different states of charge. (c) Normalized XANES spectra used for the fitting.

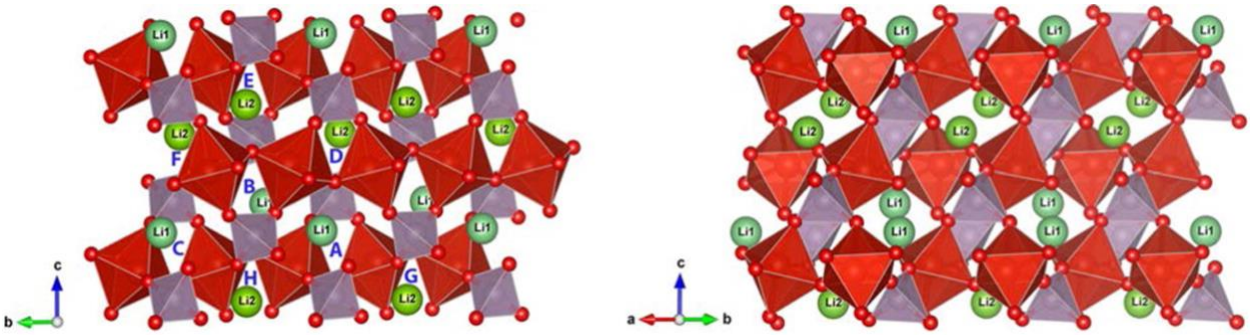

(a) [100] direction. (b) [110] direction.

Figure 2.13 Crystallographically distinct Li in $LiVOPO_4$ and investigated diffusion paths in $LiVOPO_4$ viewed along (a) [100] and (b) [110] directions. A total of six different vacancy hops were investigated. Using the labeling scheme in (a), hops A → B and B → C form a 1D channel comprising only Li1 sites, whereas hops D → E and E → F form a similar 1D channel comprising only Li2 sites. In addition, hops from one 1D channel to another (hops A → G and A → H) were also investigated.

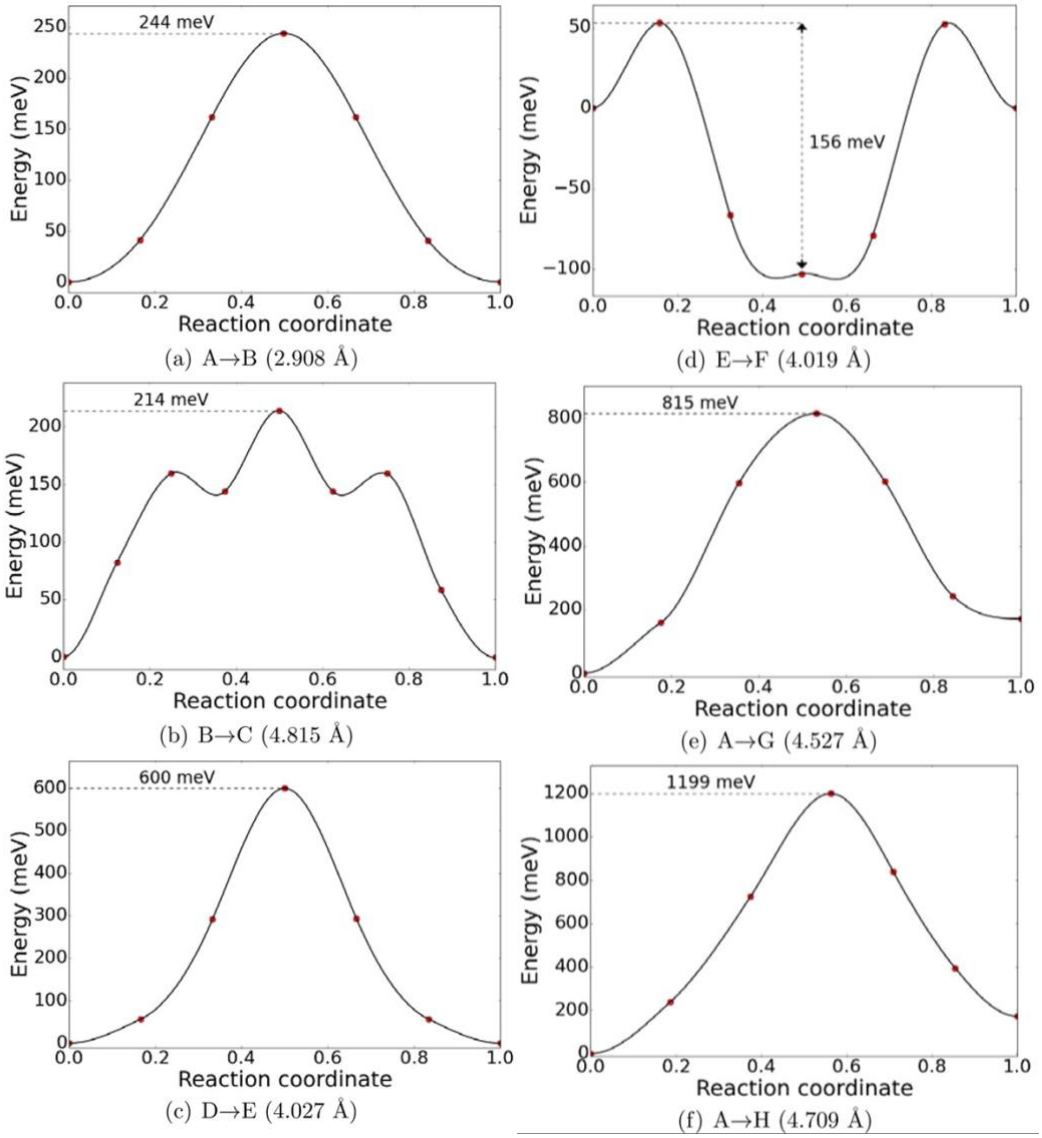

Figure 2.14 Calculated GGA CI-NEB migration barriers for various vacancy hops in $LiVOPO_4$.

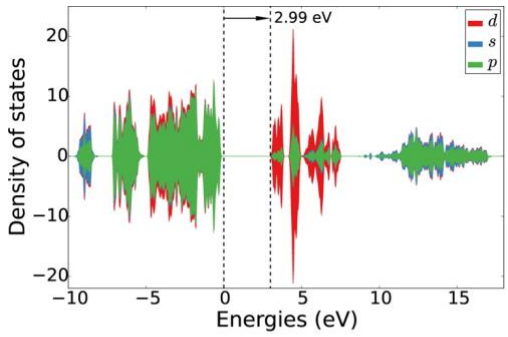

(a) $VOPO_4$

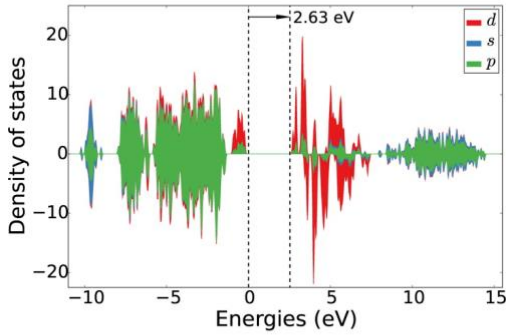

(b) $LiVOPO_4$

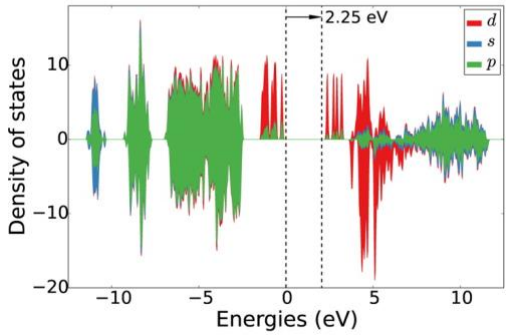

(c) Li_2VOPO_4

Figure 2.15 Orbital projected densities of states of Li_xVOPO_4 from HSE calculations.

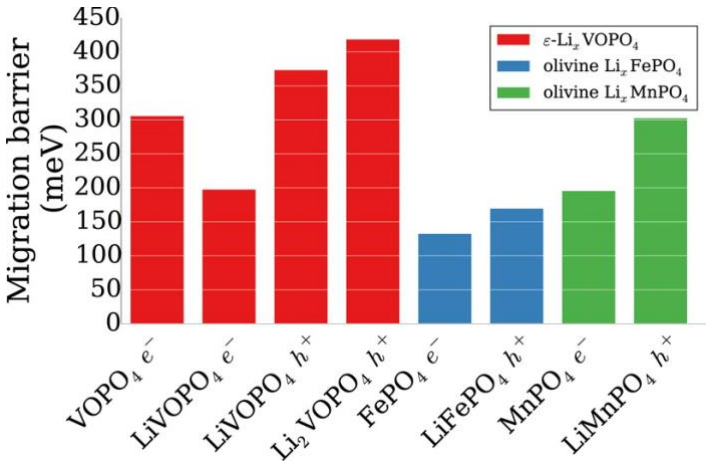

Figure 2.16 Comparison of calculated HSE polaron migration barriers for Li_xVOPO_4 with olivine $LiFePO_4$ and $LiMnPO_4$ from ref [72].

Chapter 3. Comparison of the polymorphs of $VOPO_4$ as multi-electron cathodes for rechargeable alkali-ion batteries

3.1 Introduction

The typical cathode used in today's rechargeable alkali-ion batteries are layered oxides with formula A_xMO_2, where A is an alkali-ion (Li/Na) and M is a transition metal or mixture of transition metals.[92,93] These cathodes, as well as other common cathodes such as $LiFePO_4$,[94] operate on the transfer of a single-electron per transition metal, limiting achievable energy densities. Multi-electron polyanionic cathodes offer the potential to significantly increase energy densities by leveraging on the inductive effect of polyanion chemistries to increase voltage, and the transfer of more than one electron per transition metal to increase capacity.

Several families of materials have been investigated as potential multi-electron polyanionic cathodes for rechargeable alkali-ion batteries. For example, the Li_2MSiO_4 (M = Fe, Co, Mn) silicates have theoretic capacities > 333 mAh/g,[95] but exhibit poor rate capability due to poor intrinsic ionic conductivity.[96–99] In phosphates, a previous high-throughput first-principles study has shown that only V and Mo can attain reasonable average voltages across multiple redox couples ($V^{3+} \rightarrow V^{5+}$ and $Mo^{3+} \rightarrow Mo^{6+}$) as practical multi-electron cathodes.[100] Extensive studies have been carried out on $Li_3V_2(PO_4)_3$, $Li_5V(PO_4)_2F$, $Li_9V_3(P_2O_7)_3(PO_4)_2$,[101–105] but achieving reversible cycling remains a challenge, especially for with the high V^{4+}/V^{5+} redox couple. $Na_3V_2(PO_4)_3$ has been reported with excellent rate capability and good cycling performance up to ~1.4 Na due to open NASICON structure, but with low theoretical capacity of ~120 mAh/g.[106] $Na_3V_2(PO_4)_2F_3$ has been demonstrated promising with reversible capacity ~128 mAh/g at ~3.75V using $V^{3+/}V^{4+}$ along with good rate capability and capacity retention.[107,108]

Among the candidate multi-electron polyanionic chemistries, the A_xVOPO_4 (A = Li, Na)

vanadyl phosphates are among the most promising, with good electrochemical performance having been achieved for both lithium and sodium-ion insertion.[62,109–118]. By utilizing both the $V^{3+/4+}$ and $V^{4+/5+}$ redox couples, $VOPO_4$ has a high theoretical capacity of 305 mAh / g Li_2VOPO_4 or 258 mAh / g Na_2VOPO_4. Depending on synthesis conditions, $VOPO_4$ can crystallize in one of seven polymorphs, namely, α_I (P4/*n*), α_{II} (*P4/n*), β (*Pnma*), δ (*P4*$_2$*/mbc*), ε (*Cc*), ω (*P4*$_2$*/mmc)* and γ *(Pbam)*.[62,119,120] We will henceforth refer to all lithiated/sodiated phases of $VOPO_4$ polymorphs using the prefix associated with the $VOPO_4$ phase, as proposed by Whittingham *et al*.[92] For example, even though the singly lithiated phase of ε-$VOPO_4$ is designated as α-$LiVOPO_4$ in the literature based on the order of discovery, we will instead refer to this phase as ε-$LiVOPO_4$ to establish a clear correspondence between the phases at different levels of intercalation. Among the seven polymorphs, the β, ε and α_I forms are arguably the most well-studied as multi-electron cathodes for both Li-ion and Na-ion chemistry.[121–123] For Li-ion chemistry, reasonable multi-electron cycling has been achieved in all three phases, with reversible capacities of up to ~80, ~225 and ~240 mAh/g having been achieved for β, ε and α_I respectively.[121,124] For Na-ion chemistry, on the other hand, electrochemical cycling performance has been mixed. Monoclinic $NaVOPO_4$, which is structurally similar to ε-$LiVOPO_4$, was first reported by Song *et al*.[125] with a reversible capacity of ~90 mAh/g. More recently, He *et al*. investigated α_I-$NaVOPO_4$ and β-$NaVOPO_4$ obtained from corresponding Li phases and showed that while a relatively high capacity of ~150 mAh/g can be achieved in α_I-$NaVOPO_4$ with the incorporation of reduced graphene oxide, a large irreversible capacity loss is observed during the cycling of β-$NaVOPO_4$.[111,112]

It is evident from these previous studies that different polymorphs with the same chemistry

($VOPO_4$) can exhibit radically different electrochemical performances for Li-ion and Na-ion chemistry. The $VOPO_4$ polymorphs therefore present a unique opportunity for us to probe the interplay between host structure and alkali-ion chemistry, and its corresponding effect on thermodynamic stability, voltage and diffusion kinetics. To our knowledge, no other cathode chemistry present a similarly diverse polymorphism.[93]

In this work, we performed a systematic first principles investigation, supported by careful electrochemical characterization and published experimental data, of the relative thermodynamic stability, voltage, band gap, and diffusion kinetics for alkali intercalation in β, ε and α_I polymorphs of $VOPO_4$. The primary effort is focused on the relative electrochemical performance of Li^+ insertion in the different polymorphs of $VOPO_4$, for which both density functional theory (DFT) data and experimental results are presented. To further probe the relationship between structure and electrochemical properties, we have also investigated the insertion of the larger Na^+ ion into the same hosts using DFT calculations only. We find that all three $VOPO_4$ polymorphs remain reasonably stable with one alkali-ion insertion, but become significantly less stable with two alkali-ion insertion. We will show that the significantly different cycling performances for Li^+ insertion in the different $VOPO_4$ polymorphs can be linked to the differences in Li^+ migration barriers, which in turn can be correlated to topological descriptors such as bottleneck size. Finally, we will demonstrate that the migration of the larger Na^+ ion is much more sensitive to bottleneck size compared to Li^+, and discuss this effect in the context of electrochemical performances already reported in the literature. These results provide crucial insights, such as the importance of structural selection, into the design of new multi-electron cathodes for Li-ion and Na-ion batteries.

3.2 Computational methods

All density functional theory (DFT) calculations were performed using the Vienna Ab

initio Simulation Package (VASP)[126] within the projector augmented-wave approach,[127] and all analyses were performed using the Python Materials Genomics (pymatgen) library[128] and the pymatgen-diffusion add-on.[129]

3.2.1 Generating initial structures

Initial structures of ε-$VOPO_4$ (ICSD # : 415924), ε-$LiVOPO_4$ (ICSD # : 184602), monoclinic $NaVOPO_4$, (ICSD # : 188088), β-$VOPO_4$ (ICSD # : 9413), β-$LiVOPO_4$ (ICSD # : 80613), and α_I-$VOPO_4$ (ICSD # : 108983) were obtained from Inorganic Crystal Structure Database (ICSD).[119] The initial structure for ε-Li_2VOPO_4 is based on that reported by Bianchini *et al.*[116] It should be noted that the monoclinic form of $NaVOPO_4$ is structurally similar to ε-$LiVOPO_4$, albeit with a different space group and only one symmetrically distinct Na site (instead of two symmetrically distinct Li sites in ε-$LiVOPO_4$). Henceforth, we will refer to this monoclinic form as ε-$NaVOPO_4$. As the structures of β-Li_2VOPO_4, β-Na_2VOPO_4, ε-Na_2VOPO_4, α_I-$NaVOPO_4$, α_I-Li_2VOPO_4 and α_I-Na_2VOPO_4, have not yet been reported, we obtained candidate structures by identifying potential alkali intercalation sites using a Voronoi tessellation-based algorithm, followed by an enumeration of all symmetrically distinct alkali orderings. It should be noted that it is known that the α_I polymorph exhibits alkali-ion site disorder,[111,114,130] and all sites with non-zero occupancies reported in experiments were considered in the structural enumeration. The structure with the lowest energy computed via DFT was then used as the representative structure for subsequent studies of voltage and migration barriers.

3.2.2 Total energy calculations

The total energies of all A_xVOPO_4 (x = 0, 1, 2) polymorphs were calculated using the Perdew−Burke−Ernzerhof (PBE) generalized-gradient approximation (GGA)[131] functional with

the application of an effective Hubbard U[94,132,133] of 3.25 eV for vanadium (GGA+U), similar to that used in the Materials Project.[134] All calculations were spin-polarized starting from a high-spin ferromagnetic configuration given that previous works have found magnetic effects to have a minimal impact on relative energies.[62] Similar to parameters used in the Materials Project,[134] a plane wave energy cutoff of 520 eV and k-point density of at least 1000/(number of atoms in unit cell) was used for all calculations. To estimate the thermodynamic stability of A_xVOPO_4 polymorphs, we evaluated their energy above the hull (E_{hull}) by constructing the corresponding A-V-P-O quaternary phase diagrams[135], wherein the energies of compounds other than those of primary interest in this work were extracted from Materials Project using the Materials Application Programming Interface.[136] Stable phases have an E_{hull} of 0, whereas increasing E_{hull} indicates decreasing thermodynamic stability.

3.2.3 Electronic structure calculation

The electronic band gap of all A_xVOPO_4 polymorphs (x = 0, 1 and 2) were calculated using the screened hybrid Heyd-Scuseria-Ernzerhof functional (HSE06)[137,138] with a k-point density of 500 per atoms in the unit cell.

3.2.4 Climbing-image nudged elastic band calculations

The barriers for A^+ ion and alkali vacancy v_{A^+} (lower case v is used to denote an alkali vacancy to distinguish it from upper case V for vanadium) migration in $VOPO_4$ and $AVOPO_4$ polymorphs, respectively, were calculated using the climbing image nudged elastic band (CI-NEB) method.[139,140] To avoid ambiguity regarding the localization of electrons, the PBE functional without Hubbard U was used, in line with the well-established practice in the literature.[141] For v_{A^+} migration calculations, the CI-NEB calculations were carried out using 2 × 2 × 2 supercells with

formula $A_{31}V_{32}O_{32}P_{32}O_{128}$ (32 formula units) for the β and ε polymorphs, and $A_{15}V_{16}O_{32}P_{16}O_{80}$ (16 formula units) for α_I polymorph to minimize the interactions between periodic images. Likewise, 2 × 2 × 2 supercells with formula of $A_1V_{32}O_{32}P_{32}O_{128}$ for ε and β polymorphs, and $A_1V_{16}O_{32}P_{16}O_{80}$ for α_I polymorph were used to calculate single A^+ ion migration barriers. A Γ-centered 1 × 1 × 1 *k*-point grid was used for ε and β polymorphs, while a 2 × 2 × 2 *k*-point grid was used for the α_I polymorph. The image-dependent pair potential approach was used to obtain better initial guesses of the NEB paths.[129,142] The atomic coordinates in each image were relaxed until the force components on each atom were less than 0.03 eV/Å. No compensating background charge was applied.

It should be noted that we did not attempt to study v_{A^+} migration in A_2VOPO_4. We find that the creation of a vacancy results in significant rearrangement of the alkali ions in A_2VOPO_4 due to the large number of the alkali ions in proximity with one another.

3.3 Experimental methods

β-, ε- and α_I-$LiVOPO_4$ were synthesized from $LiVOPO_4{\cdot}2H_2O$ precursor obtained by a hydrothermal method modified from previous reports.[7,18] V_2O_5 (Aldrich, ≥99.6%), oxalic acid (Sigma-Aldrich, ≥99.0%), and phosphoric acid (Fisher Scientific, 85%) were stirred in ethanol and water for 18 hours. $LiOH{\cdot}H_2O$ (Sigma, ≥99.0%) was then added, and the mixture was stirred for another 4 hours. The mixture was then placed in a 4748 Type 125 mL PTFE-lined reactor (Parr Instrument Co.) and heated to 160 °C for 48 hours. The hydrothermally synthesized $LiVOPO_4{\cdot}2H_2O$ was filtered and washed with water, ethanol, and acetone, then dried at 80 °C. The different $LiVOPO_4$ phases were then synthesized by annealing the hydrated precursor in different environments for 3 hours:

- β-$LiVOPO_4$: At 600 °C in O_2
- ε-$LiVOPO_4$: At 750 °C in Ar
- α_I-$LiVOPO_4$: At 300 °C in Ar

Powder X-ray diffraction (XRD) data were collected at room temperature with a Bruker D8 Advance diffractometer with Bragg-Brentano geometry using a Cu $K\alpha$ source ($K\alpha 1$ = 1.54053 Å, $K\alpha 2$ = 1.54431 Å). This instrument utilizes a Lynx-Eye 1D position sensitive detector (192 channel Si strip detector) with a primary and secondary radius of 280 mm. Routine pattern indexing and phase identification was done using the PDF-2015 software package, while the TOPAS software package (Bruker AXS, version 5.0) was used for Rietveld refinement.

Electrodes were prepared by high-energy ball-milling $LiVOPO_4$ with graphene for 30 minutes. Polyvinyldiene fluoride (PVDF) was then added to the mixture, resulting in a $LiVOPO_4$:graphene:PVDF ratio of 75:15:10. A slurry was formed by dissolving the mixture in n-methyl-2-pyrrolidinone (NMP), which was then cast onto a carbon-coated Al foil and dried at 60 °C. Electrodes with areas of 1.2 cm^2 and active mass loadings of 2-3 mg were punched and assembled into 2325-type coin cells with pure lithium chip (MTI) as the counter and reference electrodes, a Celgard 2400 separator (Hoechst Celanese) as the separator, and 1 M $LiPF_6$ in 1:1 v/v ethylene carbonate (EC) and dimethyl carbonate (DMC) as the electrolyte. Electrochemical tests were conducted using a VMP multichannel potentiostat (Bio-Logic). Capacities were measured through galvanostatic charge-discharge tests from 3 to 4.5 V at current densities from 5 $\mu A/cm^2$ (C/50) to 250 $\mu A/cm^2$ (C/1, where C is defined as 158.57 mAh/g). Diffusion coefficients were estimated from cyclic voltammetry (CV) data using the Randles–Sevcik equation.[143] Cells were run through CV at 0.05, 0.1, 0.2, and 0.5 mV/s, between 1.5 and 4.5 V.

3.4 Results

3.4.1 Crystal structures of A_xVOPO_4 polymorphs

Figure 3.1 shows the fully-relaxed, lowest-energy structures of A_xVOPO_4 polymorphs (x = 0, 1) from GGA+U calculations. The alkali orderings for the lowest energy structures are similar for the Li and Na forms of the ε and β polymorphs. For α_I, the lowest energy orderings are different for Li and Na, though we have found that the energy is not especially sensitive to the alkali ordering; there are > 10 structures with energies within 10 meV of the ground state. It is well-established in the literature that α_I-$LiVOPO_4$ and α_I-$NaVOPO_4$ are disordered at room temperature,[111,114] and our calculations support these observations.

We have synthesized β-, ε- and α_I-$LiVOPO_4$ polymorphs, and the X-ray diffraction patterns (see Figure 3.2) confirm the formation of pure β-, ε- and α_I-$LiVOPO_4$ phases. Overall, the measured cell parameters of the as-synthesized $LiVOPO_4$ polymorphs (see Table 3.1) are in good agreement with the DFT counterparts, with the largest volume difference being ~5.6% in the case of α_I-$LiVOPO_4$. Our calculated cell parameters for the Na_xVOPO_4 polymorphs are also in good agreement with those reported in literature.[110–112]

3.4.2 Thermodynamic stability and intercalation voltage

We evaluated the thermodynamic stability of A_xVOPO_4 polymorphs (x = 0, 1, and 2) by computing their energy above convex hull (E_{hull}).[135] The results are shown in Figure 3.3a. For $VOPO_4$, we find that the most stable polymorph is β, whereas the most stable polymorphs of $AVOPO_4$ for Li and Na versions are β and ε, respectively. For $LiVOPO_4$, Ling *et al.*[62] previously found that ε-$LiVOPO_4$ is ~10 meV/atom lower in energy than β-$LiVOPO_4$, whereas our calculations find that β-$LiVOPO_4$ is ~ 5meV/atom lower in energy than ε-$LiVOPO_4$. This is likely

due to different parameters, e.g. U value utilized in the calculations. Nevertheless, such small energy differences indicate that both ε- and β- have similar thermodynamic stability. All A_xVOPO_4 (x = 0 and 1) polymorphs have an E_{hull} of ~30 meV/atom or less up to one alkali insertion, indicating that they are likely metastable and can be stabilized at finite temperatures. This is consistent with their synthesizability in experiments.[122,123,125,144,145] β-$VOPO_4$ forms upon heating of ε-$VOPO_4$, indicating that β-$VOPO_4$ is more stable, while the opposite is true for $LiVOPO_4$ polymorphs. In our experiments, β-$LiVOPO_4$ forms at 600 °C in O_2, while further heating to 700 °C leads to the formation of ε-$LiVOPO_4$. The reports on direct synthesis methods of α_I-$VOPO_4$ are scarce and variable, which makes it difficult to evaluate its stability.[146–148] α_I-$LiVOPO_4$ can be formed at lower temperatures either from structurally related precursor $LiVOPO_4{\cdot}2H_2O$[121] or in microwave-assisted hydrothermal synthesis[118], indicating that it is the least stable among the three considered $LiVOPO_4$ phases. This is consistent with the higher calculated E_{hull} of α_I compared with the β and ε phases, and we speculate that the known alkali-ion disorder in α_I may play a role in entropically stabilizing this polymorph.

Of the three $NaVOPO_4$ polymorphs, direct high-temperature synthesis has only been reported for ε-$NaVOPO_4$ as of now[125]; the β- and α_I- polymorphs are formed by ion exchange from the Li counterparts,[111,112] which is consistent with our DFT calculations showing that ε-$NaVOPO_4$ is significantly more stable than the β and α_I equivalents. For A_2VOPO_4 polymorphs, our calculations clearly show that they have much higher E_{hull}, suggesting that they are thermodynamically more unstable compared to their $AVOPO_4$ counterparts. In particular, we note that the different polymorphs of Na_2VOPO_4 have extremely different E_{hull}, with the β form being the least stable and the ε form being the most stable. None of A_2VOPO_4 polymorphs have been synthesized directly so far; instead, they have been obtained by chemical and electrochemical

lithiation of corresponding $LiVOPO_4$ polymorphs.[109,114–117] This is consistent with the calculated reduced stability of $x = 2$ phases.

We have also constructed the 0K phase diagrams of $AVOPO_4$ polymorphs for Li and Na (see Figure 3.4). Our results show that there are no intermediate phases in the high voltage regime $VOPO_4$-$AVOPO_4$, which agree with experimental findings in literature.[62,109–112,114–116,121–123,144,146,149] In the low voltage region $AVOPO_4$-A_2VOPO_4, there are two intermediate phases at 1.5 and 1.75 for the ε polymorph intercalated with Li, which is in good agreement with previous experimental findings.[116,149] Although our calculations indicate that there is an intermediate phase for the β polymorph at $x = 1.5$ for both Li and Na, there is no clear experimental evidence so far. This might be due to the relatively poor crystallinity of the samples by either low-temperature synthesis method proposed by He *et al.* or ball-milling.[112]

Figure 3.3b shows the calculated voltage profiles of the different polymorphs for Li and Na insertions, respectively. We find that the average voltage for Li insertion is about 0.33-0.69 V higher than for Na insertion, in line with the observed voltage differences in other host structures.[93]

Figure 3.5 shows the cyclic voltammetry (CV) curves measured at several sweep rates over the 1.5 V to 4.5 V voltage range. Each peak at a specific voltage corresponds to an electrochemical reaction. In the high-voltage regime, all three polymorphs show a single peak for the $LiVOPO_4$ to $VOPO_4$ transformation at 4.2, 4.1, and 4.0 V for β-, ε-, and α_1-$LiVOPO_4$, respectively. The observed voltage trend of $\beta > \varepsilon > \alpha_1$ agrees with the trend from first principles calculations (see Figure 3.3b). The computed and measured average voltages for the first redox process ($V^{4+/5+}$) are also in excellent agreement with reported experimental voltages in the literature (β-$LiVOPO_4 \approx 3.9$ V, β-$NaVOPO_4 \approx 3.3$ V, ε-$LiVOPO_4 \approx 3.95$ V, ε-$NaVOPO_4 \approx 3.6$ V, α_1-$LiVOPO_4 \approx 3.7$ V, α_1-$NaVOPO_4 \approx 3.4$V).[110–112,114,149,150]

In the low-voltage region ~2V, only one peak is observed for β and α_1-$LiVOPO_4$, while three distinct peaks are observed for ε-$LiVOPO_4$ during charging/discharging. These findings suggest that there are no intermediate phases for insertion of Li in α_1- and β-$LiVOPO_4$, but there are two intermediate phases at ~ x = 1.5 and x = 1.75 for insertion of Li into ε-$LiVOPO_4$, which are in agreement with the calculated α_1-Li_xVOPO_4 phase diagram and our recent studies of ε-$LiVOPO_4$.[109,113,151] The voltages measured from the experimental CV data follows the trend $\alpha_1 > \varepsilon > \beta$, which is again in agreement with the first principles calculations.

3.4.3 Alkali ion migration barriers

β-A_xVOPO_4. There is only one symmetrically distinct v_{A+} diffusion path in β-$AVOPO_4$, which is denoted as path A-B along [010] direction (see Figure 3.6a). We find the barriers of v_{Li+} and v_{Na+} migrations in β-$LiVOPO_4$ and β-$NaVOPO_4$ are 239 and 255 meV, respectively, and the barriers of Li^+ and Na^+ migration in β-$VOPO_4$ are 346 and 541 meV, respectively.

For β-A_xVOPO_4 (x = 0, 1), both Li^+ and Na^+ exhibit 1D diffusion along the [010] direction, in line with the previous simulation and experimental results.[62,112] We notice that our computed v_{Li+} diffusion barrier in β-$LiVOPO_4$ (239 meV) differs substantially from a previous study by Ling *et al*. (150 meV).[62] This may be due to the fact that the GGA+*U* functional was employed in that study, whereas we used GGA functional in the current study to avoid any mixing of the diffusion barrier with a charge transfer.

ε-A_xVOPO_4. The barriers for v_{Li+} migration in ε-$LiVOPO_4$ have already been reported in our recent work,[109] and we will briefly summarize the key results here. The two 1D paths, path A→B→C (formed by Li1 sites) and path D→E→F (formed by Li2 sites) in Figure 3.7a, have

barriers of 244 and 703 meV, respectively. Significantly higher barriers of > 800 meV are found for inter-chain migration (paths A→G and A→H). In comparison, the migration barriers for v_{Na+} in ε-$NaVOPO_4$ are much higher, with barriers exceeding 1eV for all paths (Figure 3.7b). We have tested the sensitivity of this result to the functional used; similar results are obtained with the PBEsol functional[152], even though the lattice parameters are much closer to that of the experimental values.

At the beginning of discharge, there are three distinct paths for A^+ diffusion in ε-$VOPO_4$. For paths A→B, A→C and A→D, the barriers for Li^+ migrations are 271, 629 and 637 meV, respectively, and those for Na^+ migrations are 516, 674, and 694 meV, respectively (see Figure 3.8a). We note that our calculated Li^+ migration barriers are somewhat lower than the values of 463 (1D), 738 (2D), 1215 (3D) meV previously reported by Mueller *et al.*[141] We believe that the difference is due to the fact that a delithiated ε-$LiVOPO_4$ framework with triclinic symmetry was used in Mueller *et al.*'s work, whereas the experimentally observed ε-$VOPO_4$ with monoclinic symmetry is used in this work.

α_I-A_xVOPO_4. For α_I-$LiVOPO_4$, there are four distinct v_{Li+} diffusion paths, denoted as paths A→B, A→C, A→D and A→E in Figure 3.9a, with calculated barriers of 728, 762, 449, and 328 meV, respectively. In α_I-$NaVOPO_4$, there are three distinct v_{Na+} diffusion paths, denoted as paths A→B, A→C and A→D in Figure 3.9b, with calculated barriers of 263, 1409 and 565 meV, respectively. The much higher barrier of 1409 meV in path A→C is likely due to the much shorter distance of the two VO_6 octahedra to the path (see Table S1 in SI). As it is well-established that alkali ions in α_I-$AVOPO_4$ are disordered, we also evaluated the v_{Na+} migration barriers for the v_{Li+} paths shown in Figure 3.9a. We find that the v_{Na+} migration barriers for A→B, A→C, A→D

and A→E are 651, 548, 261 and 123 meV, respectively, which in all instances are lower than the corresponding v_{Li+} migration barriers.

For α_1-$VOPO_4$, three distinct diffusion paths for Li^+ are identified, denoted as paths A→B, A→C and A→D in Figure 3.10a with calculated barriers of 276, 282 and 284 meV, respectively. Such similar barriers are likely due to the similar local environments of barrier bottlenecks of these three paths (see Table 3.2). In the case of single Na^+ migration, the barriers of A→B, A→C and A→D are 438, 2308 and 427 meV, respectively. The much higher barrier of the A→C path is likely due to the much shorter Na-O and Na-V distances than those in the A→B and A→D paths (see Table 3.2).

3.4.4 Electronic band gap

Figure 3.13 shows the calculated electronic band gaps of A_xVOPO_4 (x = 0, 1 and 2) polymorphs. All polymorphs are found to have band gaps > 2.1 eV, indicating that they are insulators. The electronic band gaps of the β and ε polymorphs decrease with alkalination, but the electronic band gap of α_1 polymorph increases by > 0.6 eV upon the insertion of first alkali ion and then decreases by ~1 eV when the second alkali ion is inserted. We will discuss the reasons for this different behavior in the Discussion section. Overall, our electronic band gap calculations suggest that carbon coating is critical for improving the electron conduction in these polymorphs.

3.4.5 Electrochemical performance

We have performed a rate test for all the three $LiVOPO_4$ polymorphs and calculated Li diffusion coefficients from the cyclic voltammetry data. Figure 3.14 shows the electrochemical performance for one-Li cycling between $LiVOPO_4$ and $VOPO_4$ (3 to 4.5 V) at various current densities. Though the high-voltage capacities for all polymorphs fall short of the theoretical 159 mAh/g, β-$LiVOPO_4$ exhibits the highest capacity of all the three phases (~ 90 mAh/g) at C/20,

followed by ε-$LiVOPO_4$ and α_I-$LiVOPO_4$, both exhibiting capacities of ~80 mAh/g. At a higher rate of C/10, the β polymorph does not experience significant capacity loss, while the capacities of ε and α_I polymorphs drop to below 70 mAh/g. With further current increase to 1C, the β and ε polymorphs show similar capacity retention of about 50%, while the α_I polymorph retains only 40% of its capacity. When the current rate is decreased to C/50, all the polymorphs show similar capacities, around 90 mAh/g. These observations indicate that the ε and α_I polymorphs clearly suffer more capacity loss at high rates, which are indicative of poorer Li diffusion kinetics in these polymorphs relative to the β polymorph.

The high-voltage cycling of β- and ε-$LiVOPO_4$ at C/10 have previously been reported by Allen *et al*.[124] The capacities for β-$LiVOPO_4$ reported in that work are similar to our measurement. The ε-phase shows higher capacity of about 120 mAh/g, but it should be noted that a significant part of this capacity comes from the sloping part of the electrochemical curve, which is absent in our sample (see Figure 3.15). The true high-voltage plateau at about 3.86 V is the same in both works. The electrochemistry of α_I-$LiVOPO_4$ at C/10 was also reported previously,[113,121] but in a larger voltage range between 2.5 V and 4.4 V, resulting in capacities of 100 to 120 mAh/g. Such differences in the electrochemical performances may be attributed to differences in morphology (see Figure 3.16) caused by different synthesis and ball-milling methods, and by the electrode preparation technique, in particular the amount and kind of carbon used. Our data obtained for three different polymorphs synthesized from the same precursor and employing the same electrode preparation indicates that β-$LiVOPO_4$ exhibits the highest capacity, followed by ε-$LiVOPO_4$ then α_I-$LiVOPO_4$. We will discuss the observed electrochemical performance in the context of the calculated alkali migration barriers and band gaps.

From the CV, we estimated the apparent diffusion coefficient from the plot of the current versus the square root of the scan rate ($v^{1/2}$) (see Figure 3.17) via the Randles–Sevcik equation:

$$i_p = (2.69 \times 10^5) n^{\frac{3}{2}} A D^{\frac{1}{2}} C v^{\frac{1}{2}} \quad (1)$$

where i_p is the current at an electrochemical reaction, n is the number of electrons participating in one mole of the reaction, which is one in this case. A is the electrode-electrolyte interface area, D is the apparent diffusion coefficient, C is the mole concentration of Li-ions in the electrode, and v is the scan rate. In our calculations, the electrode-electrolyte interface is approximated to be the electrode area. Special care was also taken so that cells would have similar mass loadings to avoid introducing variations in the current experienced by the materials due to differences in mass loading.

Table 3.3 shows the estimated apparent diffusion coefficients for the insertion of Li to $VOPO_4$ and the removal of Li from $LiVOPO_4$. These values are calculated from the peaks in the CV curves above 3V. Specifically, the insertion of Li to $VOPO_4$ is observed as a peak with a negative current while the removal of Li from $LiVOPO_4$ is observed as a peak with a positive current. We find that the β polymorph has the highest diffusion coefficient at the start of both charge and discharge in the high voltage regime, followed by α_1 and then ε. Quantitative comparison of these results with the CI-NEB migration barriers summarized in Figure 3.12 is difficult, given that the diffusion coefficients estimated from the CV are total diffusivities for the polycrystalline electrode, while the calculations are based on perfect crystals. Nevertheless, we may make several useful qualitative observations. In general, the CI-NEB calculations predict the β polymorph has the lowest migration barriers for Li^+, albeit only in 1D. This agrees with the experimentally observed diffusion coefficients in Table 3.3. Between the ε and α_1 polymorphs, the effective barriers for 1D Li^+ diffusion are very similar in these two phases, while the effective

barriers for >1D Li^+ diffusion are significantly lower in the α_I phase. Therefore, we speculate that >1D diffusion may account for the higher diffusivity observed in the α_I phase in experiments. Nevertheless, we observe that all three polymorphs have reasonably low diffusion barriers for Li^+.

3.5 Discussion

The lithium vanadium phosphate Li_xVOPO_4 polymorphs have been studied as potential multi-electron cathodes that can enable high energy-density lithium-ion batteries.[109,114–117] Their Na analogs, on the other hand, have been explored only fairly recently as potential cathode materials for Na-ion batteries.[110–112] In this work, we have attempted to provide a systematic assessment of the three most common $VOPO_4$ polymorphs – β, ε and α_I – in terms of key properties such as stability, voltage and alkali migration barriers using first principles calculations supported by experimental characterization in this work as well as those in literature.

We find that all three $VOPO_4$ polymorphs show reasonable stability for one Li insertion, though the insertion of a second Li is accompanied by a significant decrease in stability with relatively high E_{hull} of ~80 meV/atom. All polymorphs are predicted to show two-phase behavior in the high voltage regime. In the low-voltage regime, β phases are predicted to have intermediate phases of β-$A_{1.5}VOPO_4$ while there are ε-$Li_{1.5}VOPO_4$ and ε-$Li_{1.75}VOPO_4$ for ε phases. For α_I phases, they are predicted to still exhibit two-phase behavior. We suspect that the absence of β-$Li_{1.5}VOPO_4$ in our experiment might be due to the poorer crystallinity from ball-milling. Another reason may be that we used relatively fast charge rate.

We may interpret the measured electrochemistry for Li intercalation in the context of the calculated Li^+ migration barriers and the electronic band gap. The calculated v_{Li+} and Li^+ migration barriers for minimally 1D diffusion are relatively similar between the β (239 meV and 255 meV, respectively, see Figure 3.12) and ε (244 meV and 271 meV, respectively) polymorphs. The α_I

(328 meV and 276 meV, respectively) polymorph has somewhat higher barriers, especially at the beginning of charge. The calculated band gap for α_I $LiVOPO_4$ is also significantly higher than that of β and ε. We would speculate that the better performances of the β and ε over α_I for Li^+ intercalation can be attributed to their lower barriers for Li^+ and smaller band gap (higher electronic conductivity).

In contrast, the three polymorphs are predicted to have very different performances as Na-ion multi-electron cathodes. Of the three polymorphs, β polymorph becomes extremely unstable with two Na insertion (E_{hull} = 126 meV), and it also exhibits high barriers at the beginning of discharge. Though the ε polymorph remains the most stable for up to two Na^+ insertion, the barriers for Na^+ migration are extremely high, especially at the beginning of charge from ε-$NaVOPO_4$ (> 1.5 eV). On the contrary, α_I polymorph is predicted to show a combination of reasonable stability and sufficiently low barriers for 2D Na^+ migration. These findings are in general agreement with the observed electrochemical performance reported in the literature which shows that β-$NaVOPO_4$ and ε-$NaVOPO_4$ have comparatively worse reversibility and lower cycling capacity.[112,125] In contrast, cycling of α_I-Na_xVOPO_4 has been demonstrated with relatively high capacity of ~150 mAh/g.[111]

We may attribute the differences in the electrochemical performance for Li and Na of the $VOPO_4$ polymorphs to their fundamentally different arrangements of VO_6/VO_5-PO_4 frameworks. β and ε polymorphs have rigid 3D VO_6-PO_4 frameworks where the barriers of alkali migration are determined to a large degree by void space between the structural framework. The significantly higher density of ε–$VOPO_4$ and ε–$NaVOPO_4$ compared to β–$VOPO_4$ and β–$NaVOPO_4$ (see Table 3.1) leads to much higher barriers for Na^+ migration. On the contrary, the α_I polymorph has a layered structure, with 2D layers of alkali ions sandwiched between layers of VO_5-PO_4 stacked in

the *a* lattice direction. Such a structure, which bears significant similarity to the layered AMO_2 structures, can expand to accommodate the larger Na^+ ion, leading to low migration barriers and reasonable electrochemical performance. Indeed, we find that α_1-$NaVOPO_4$ has a much larger inter-layer spacing of ~3.70 Å compared to α_1-$LiVOPO_4$ (~3.02 Å), which has been shown to strongly affect the alkali migration barrier in the O3 and P2 layered AMO_2 materials.[93,153]

We should also point out that the inter-layer spacing of the α_1 polymorph is substantially reduced by ~0.7 Å upon full de-alkalination. This implies that the alkali ion migration at fully de-alkaliated α_1-$VOPO_4$ may be less facile, especially for Na^+ due to its larger ionic radius as compared to Li^+. Indeed, this is in line with our migration barrier calculations for α_1-$NaVOPO_4$.

To further elaborate the correlation between the framework topology and alkali ion migration, we have estimated the bottleneck size (r_c), which is defined as the radius of the largest free sphere that can pass through the diffusion network formed by the structural framework, of all the $AVOPO_4$ polymorphs using the open source Zeo++ software[154,155] (see Figure 3.12). In general, we find that the computed bottleneck size is approximately inversely correlated to the *lowest percolating* migration barrier when comparing between close-packed β and ε polymorphs. We also note that while the vacancy migration barrier in $NaVOPO_4$ is lower than that for Na^+ migration in $VOPO_4$ for the β and α_1 polymorphs due to a significant increase in channel size with one Na insertion, the vacancy migration barriers in ε-$NaVOPO_4$ are much higher than that for Na^+ migration in ε-$VOPO_4$ as there is negligible change in bottleneck size with on Na insertion. However, although the layered α_1 always has the largest bottleneck size among the alkaliated and fully dealkaliated $AVOPO_4$ polymorphs (e.g 1.57 Å and 1.61 Å for α_1-$LiVOPO_4$ and α_1-$NaVOPO_4$, respectively), the associated lowest percolating migration barrier can be higher than that in the other two polymorphs, as shown in the case of $LiVOPO_4$. This suggests that the migration barrier

does not barely depend on r_c, but also the local VO_6/VO_5-PO_4 arrangement.

The VO_6/VO_5-PO_4 arrangement may also account for the electronic structure changes with alkali insertion. As can be seen from Figure 3.13, the band gap of α_1 sharply increases with the insertion of the first Li/Na (x = 1), followed by a sharp decrease with the insertion of the second Li/Na (x = 2). In contrast, the band gaps of β and ε follow a monotonic decreasing trend upon alkali insertion. We speculate that there are two possible reasons for the observed trends. First, V is in a square pyramidal VO_5 environment in α_1, and in octahedral VO_6 environment in β and ε. From the DOS of the different A_xVOPO_4 polymorphs (see Figure 3.18), we may observe that the vbm and cbm of the $AVOPO_4$ (x = 1) are dominated by V d orbitals. The d_{xz} and d_{yz} orbitals in a square pyramidal environment lie below the t_{2g} orbitals of the octahedral environment due to the breaking of the degeneracy of the t_{2g} orbitals from the distortion. This may have resulted in additional stabilization for the first electron added to α_1, resulting in an increase in the band gap. Second, as highlighted earlier, α_1 comprises layers of VO_5-PO_4 stacked in the a crystallographic direction, while β and ε comprises 3D networks of interconnected VO_6-PO_4. α_1 undergoes an expansion in the a crystallographic direction upon the insertion of the first Li/Na (see Table 3.1), which may have contributed to the increase in band gap.

Finally, the DFT and experimental insights suggest several avenues for improving the performance of $VOPO_4$ polymorphs for alkali intercalation. We note that the β and ε exhibit low alkali diffusion barriers only in 1D, and only the α_1 has low alkali barriers in 2D. All three polymorphs are predicted to be large band gap insulators, with α_1 exhibiting a particular large increase in band gap for the single alkali insertion. These features – fast 1D conduction and electronic insulator – are similar to the well-known $LiFePO_4$ cathode. Similar to $LiFePO_4$, we

expect that nanosizing is critical in the $VOPO_4$ polymorphs to minimize the occurrence of blocking defects that causes capacity loss[85], as well as to shorten conduction length scales in view of their insulating nature. However, these requirements need to be balanced against the higher reactivity of $VOPO_4$ compared to $FePO_4$, which we expect to be exacerbated with nanosizing. Enhancing the electronic conductivity of $VOPO_4$ through coating with conductive materials (e.g., various forms of carbon)[156,157] would also be critical, and some coating materials may have the additional benefit of serving as a protective layer to mitigate reactions with the electrolyte.

3.6 Conclusion

In summary, we have conducted a combined first-principles and experimental study to evaluate the thermodynamic stability, voltage, band gap and diffusion kinetics for Li and Na intercalation in the β, ε and α_1 polymorphs of $VOPO_4$. We find that the three $VOPO_4$ polymorphs remain reasonably stable with one alkali insertion, but become significantly less stable with two alkali insertion. For Li^+ insertion, either ionic or electronic conduction can be the limiting factor in performance. For Na^+ insertion, performance is likely to be diffusion-limited, with only the α_1 polymorph exhibiting reasonable migration barriers for Na^+ migration. The main reason is that larger size of the Na^+ makes it particularly sensitive to changes in bottleneck size as a result of the fundamentally different VO_6/VO_5-PO_4 frameworks of the different polymorphs. These results provide crucial insights, such as the importance of structural selection, into the design of new multi-electron cathodes for Li-ion and Na-ion batteries.

Chapter 3 is, in full, a reprint of the material "Comparison of the polymorphs of $VOPO_4$ as multi-electron cathodes for rechargeable alkali-ion batteries" as it appears in Journal of Materials Chemistry A, Y. C. Lin, M. F. V. Hidalgo, I. H. Chu, N. A. Chernova, M. Stanley Whittingham and S. P. Ong, 2017, **5**, 17421–17431. The dissertation author was the primary investigator and

author of this paper. All calculations and corresponding data analysis were done by the author. The experimental portion of the work – synthesis, characterization and data analysis were done by collaborator, M. F. V. Hidalgo.

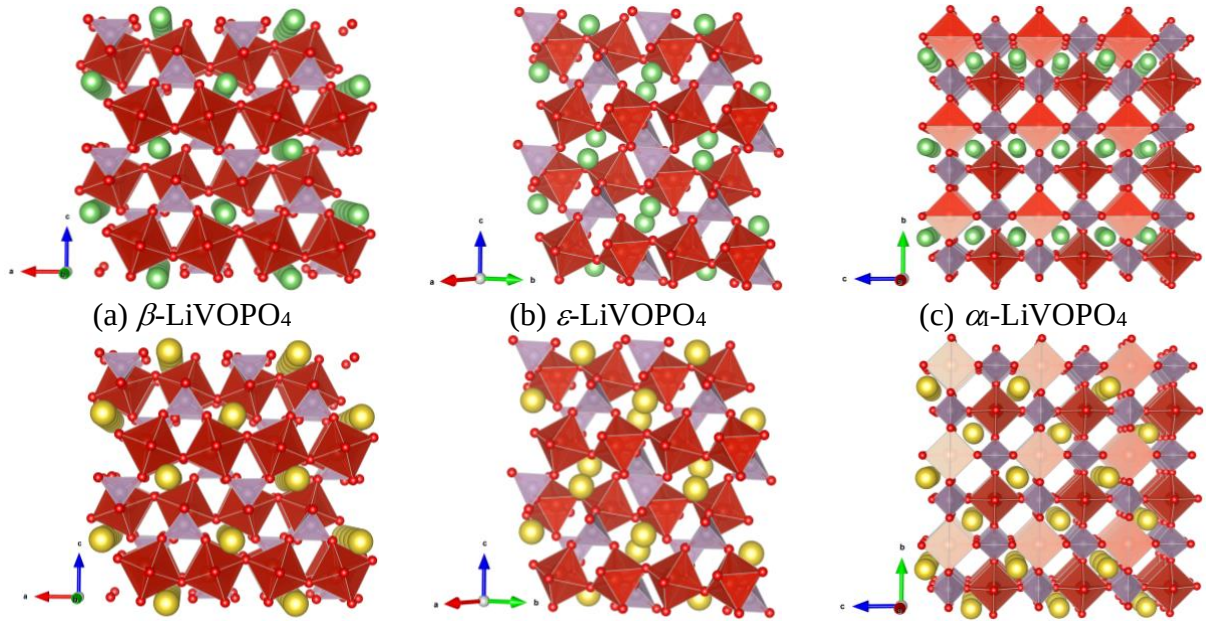

(a) β-$LiVOPO_4$ (b) ε-$LiVOPO_4$ (c) α_1-$LiVOPO_4$

(d) β-$NaVOPO_4$ (e) ε-$NaVOPO_4$ (f) α_1-$NaVOPO_4$

Figure 3.1 Lowest-energy structures of $AVOPO_4$ polymorphs (A=Li, Na). Yellow and green spheres denote Na^+, and Li^+ respectively. The red octahedrons refer to VO_6 unit and the purple tetrahedrons refer to PO_4 units.

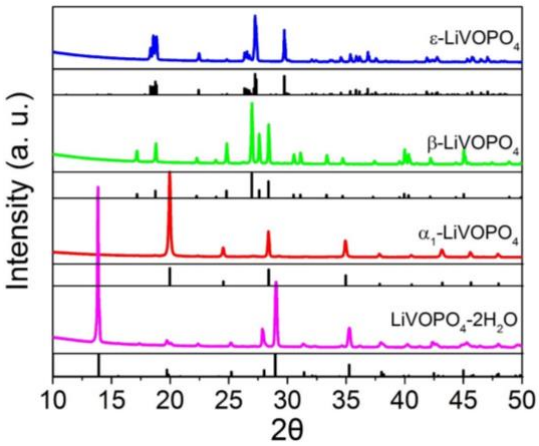

Figure 3.2 XRD patterns for all $LiVOPO_4$ polymorphs synthesized in this work.

Table 3.1 Calculated and experimental (in brackets, where available) lattice parameters for A_xVOPO_4.

	A	x	a (Å)	b (Å)	c (Å)	α (°)	β (°)	γ (°)	Density (g/cm^3)	Ref.
β	Li/Na	0	7.817	6.240	7.215	90.00	90.00	90.00	3.06	
			(7.770)	(6.143)	(6.965)	(90.00)	(90.00)	(90.00)	(3.24)	[158]
	Li	1	7.409	6.391	7.371	90.00	90.00	90.00	3.21	
			(7.444)	(6.300)	(7.174)	(90.00)	(90.00)	(90.00)	(3.33)	[159]
			(7.439)	(6.277)	(7.164)	(90.00)	(90.00)	(90.00)	(3.35)	This work
		2	7.809	6.515	7.415	90.00	90.00	90.00	3.10	
	Na	1	7.439	6.487	7.844	90.00	90.00	90.00	3.24	
			(7.539)	(6.374)	(7.621)	(90.00)	(90.00)	(90.00)	(3.35)	[112]
		2	7.455	6.945	8.567	90.00	90.00	90.00	3.11	
ε	Li/Na	0	7.347	7.060	7.383	90.00	90.00	115.43	3.11	
			(7.266)	(6.893)	(7.265)	(90.00)	(90.00)	(115.30))	(2.92)	[160]
	Li	1	6.952	7.150	7.954	89.80	91.30	116.66	3.17	
			(6.731)	(7.202)	(7.923)	(89.86)	(91.26)	(116.89)	(3.27)	[161]
			(6.736)	(7.195)	(7.913)	(89.83)	(91.30)	(116.92)	(3.28)	This work
		2	7.333	7.196	7.853	89.54	89.91	116.24	3.14	
			(7.199)	(7.101)	(7.777)	(89.82)	(89.81)	(116.32)	(3.27)	[116]
	Na	1	6.656	8.571	7.085	90.00	90.00	114.73	3.35	
			(6.518)	(8.446)	(7.115)	(90.00)	(90.00)	(115.25)	(3.47)	[125]
		2	6.708	8.964	8.755	90.00	90.00	107.94	2.76	
α_I	Li/Na	0	6.252	6.252	4.660	90.00	90.00	90.00	2.95	
			(6.200)	(6.200)	(4.110)	(90.00)	(90.00)	(90.00)	(3.06)	[147]
	Li	1	6.339	6.386	4.607	90.00	90.00	93.02	3.01	
			(6.291)	(6.291)	(4.445)	(90.00)	(90.00)	(90.00)	(3.19)	[130]
			(6.290)	(6.290)	(4.443)	(90.00)	(90.00)	(90.00)	(3.20)	This work
		2	6.595	6.643	4.176	90.00	89.90	90.00	3.19	
			(6.479)	(6.479)	(4.213)	90.00	90.00	90.00	(3.30)	[114]
	Na	1	6.336	6.336	5.372	90.00	90.00	90.00	2.85	
			(6.298)	(6.298)	(5.119)	(90.00)	(90.00)	(90.00)	(3.03)	[111]
		2	6.473	6.712	5.064	89.96	90.00	90.00	3.14	

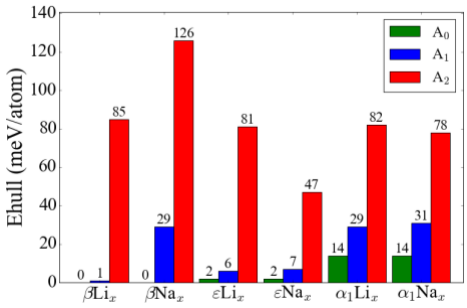

(a) E_{hull} of polymorphs

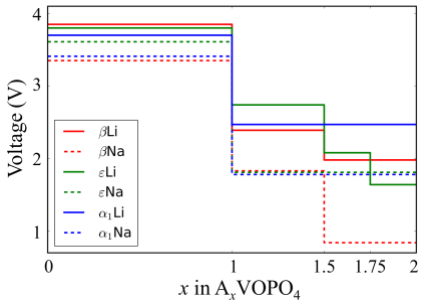

(b) Voltage profile of polymorphs

Figure 3.3 (a) Calculated E_{hull} for A_xVOPO_4 polymorphs (A=Na and Li; x=0, 1 and 2). (b) GGA+U average voltages of A_0VOPO_4-A_1VOPO_4 and A_1VOPO_4-A_2VOPO_4 polymorphs.

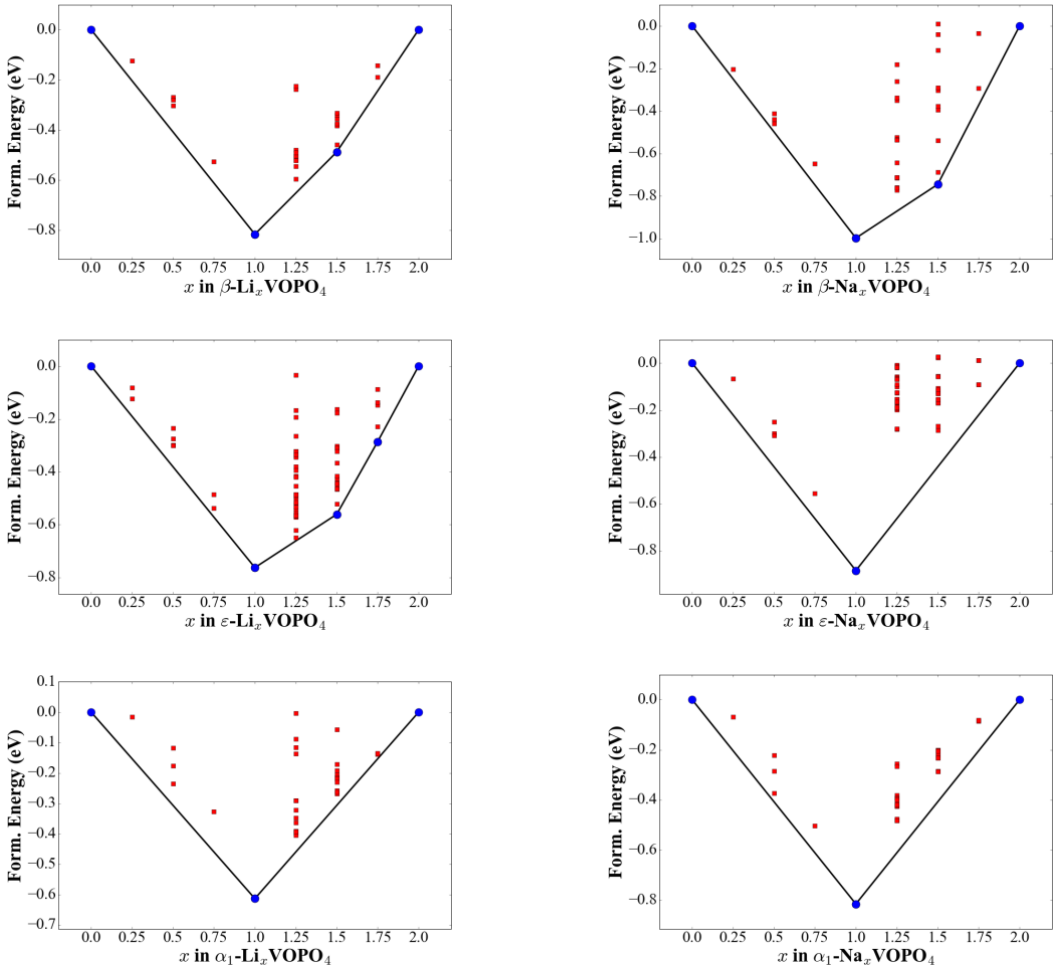

Figure 3.4 Pseudo-binary phase diagram for A_xVOPO_4 (A=Li and Na) polymorphs. The red squares and blue circles denote unstable and stable structures, respectively. The black line is the convex hull.

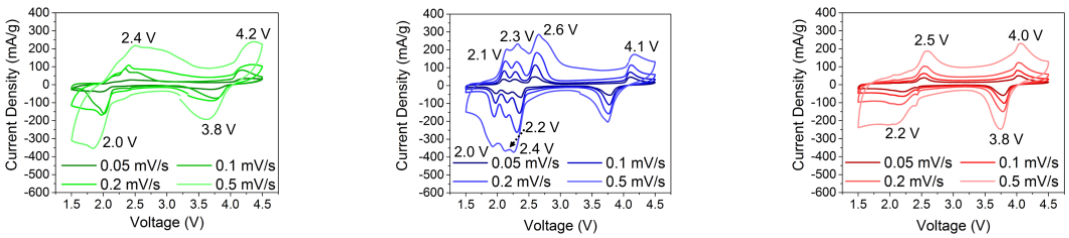

(a) β (b) ε (c) α_I

Figure 3.5 Cycling voltammetry for (a) β, (b) ε, and (c) α_I polymorphs of Li_xVOPO_4.

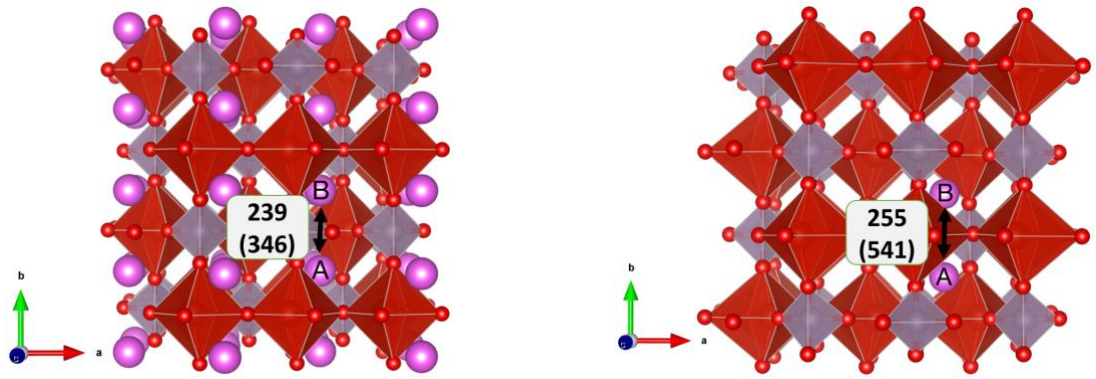

(a) (b)

Figure 3.6 Migration paths and barriers for (a) v_{A+} and (b) A^+ migration in β-$AVOPO_4$ and β-$VOPO_4$, respectively. The labeled values in (a) and (b) are the corresponding barriers for Li^+ (Na^+) and v_{Li+} (v_{Na+}) migrations in meV. Purple spheres denote A^+.

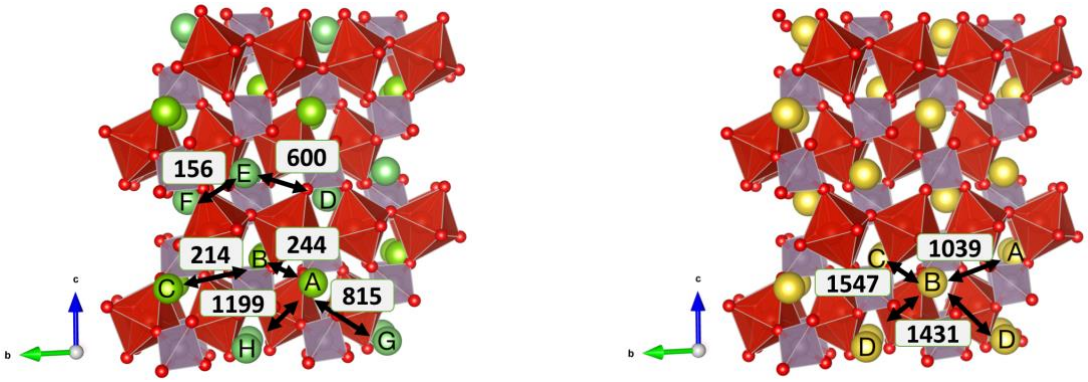

(a) (b)

Figure 3.7 Migration paths and barriers for (a) v_{Li+} in ε-$LiVOPO_4$ and (b) v_{Na+} in ε-$NaVOPO_4$. The labeled values are the corresponding CI-NEB migration barriers in meV. Green and yellow spheres denote Li^+, and Na^+, respectively.

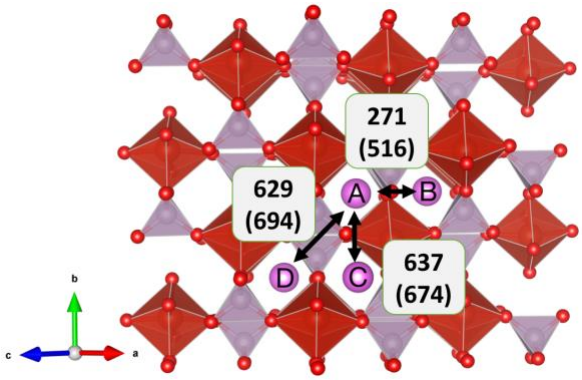

Figure 3.8 Migration paths and barriers for A^+ in ε-$VOPO_4$. The labeled values are the corresponding CI-NEB barriers for Li^+ (Na^+) migration in meV. Purple spheres denote A^+.

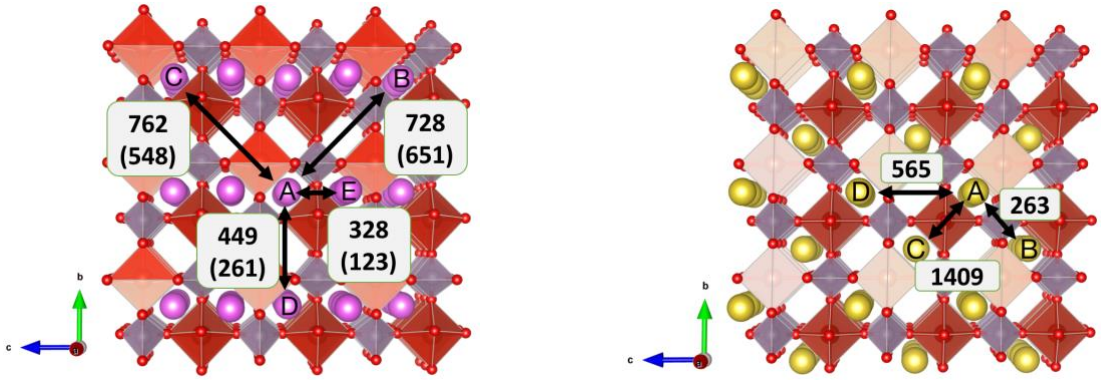

(a) (b)

Figure 3.9 (a) Migration paths and barriers for v_{A+} in the lowest energy alkali ordering for (a) α_I-$LiVOPO_4$ and (b) α_I-$NaVOPO_4$. Purple and yellow spheres denote alkali ions. The labeled values in (a) are barriers of v_{Li+} (v_{Na+}) migration and those in (b) are barriers of v_{Na+} migration in meV.

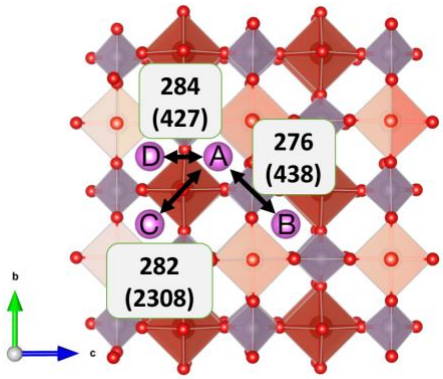

Figure 3.10 Migration paths and barriers for A^+ in α_I-$VOPO_4$. The labeled values are the corresponding barriers of Li^+ (Na^+) migration in meV. Purple spheres denote A^+.

Table 3.2 The CI-NEB migration barriers and the associated local environment information in A_xVOPO_4. A* stands for the alkali-ion in the transition state of a migration path. The minimum distances from A* to oxygen, vanadium and phosphorus are abbreviated as Min A*-O, Min A*-V and Min A*-P, respectively.

A_xVOPO_4 (x = 0, 1)	Path	Barrier (meV)	Min A*-O (Å)	Min A*-V (Å)	Min A*-P (Å)
β-$LiVOPO_4$ +v_{Li+}	A→B	239	1.869	2.887	2.635
β-$VOPO_4$ + Li^+	A→B	255	1.878	2.993	2.629
ε-$LiVOPO_4$ + v_{Li+}	A→B	244	1.826	2.874	3.076
	B→C	214	1.998	2.571	3.239
	D→E	600	1.803	2.593	3.063
	E→F	156	1.876	2.968	2.883
	A→G	815	1.899	2.819	2.441
	A→H	1199	1.931	3.415	2.295
ε-$VOPO_4$ + Li^+	A→B	271	1.853	2.870	2.703
	A→C	637	1.945	2.672	2.563
	A→D	629	1.803	2.619	2.226
α_I-$LiVOPO_4$ + v_{Li+}	A→B	728	1.868	2.969	2.555
	A→C	762	1.856	2.943	2.484
	A→D	449	1.827	3.060	2.468
	A→E	328	1.802	3.176	2.473
α_I-$VOPO_4$ + Li^+	A→B	276	1.856	3.119	2.619
	A→C	282	1.856	3.105	2.623
	A→D	284	1.855	3.095	2.629
β-$NaVOPO_4$ + v_{Na+}	A→B	346	2.111	3.211	2.699
β-$VOPO_4$ + Na^+	A→B	541	2.131	3.117	2.683
ε-$NaVOPO_4$ + v_{Na+}	A→B	1039	2.013	2.938	3.156
	B→C	1547	1.999	2.720	3.140
	B→D	1431	2.056	3.314	2.512
ε-$VOPO_4$ + Na^+	A→B	516	2.062	3.051	2.922
	A→C	674	2.155	2.981	2.648
	A→D	694	2.156	3.233	2.648
α_I-$NaVOPO_4$ + v_{Na+}	A→B	263	2.166	3.523	2.988
	A→C	1409	2.045	2.560	4.023
	A→D	565	2.152	3.217	2.865
α_I-$NaVOPO_4$* + v_{Na+}	A→B	651	2.198	3.030	2.818
	A→C	548	2.195	3.004	2.762
	A→D	261	2.163	3.312	2.819
	A→E	123	3.637	2.176	2.940
α_I-$VOPO_4$ + Na^+	A→B	438	2.176	3.754	2.744
	A→C	2308	1.889	2.257	3.886
	A→D	427	2.112	3.430	2.743

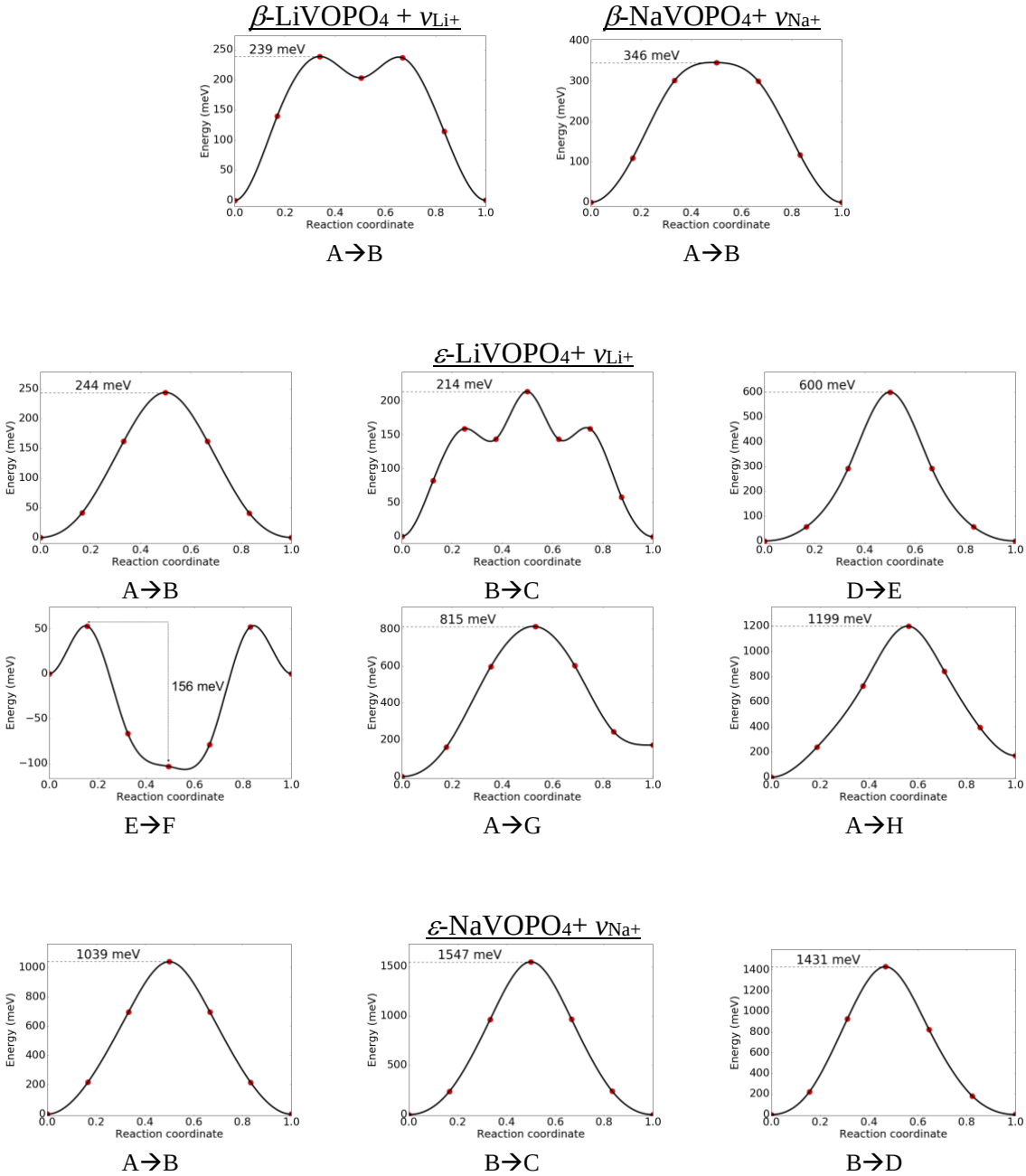

Figure 3.11 Calculated CI-NEB migration barriers in A_xVOPO_4 polymorphs (A=Li and Na; x=0 and 1). The labels are associated with those in Table 3.2.

α_I-$LiVOPO_4$+ v_{Li+}

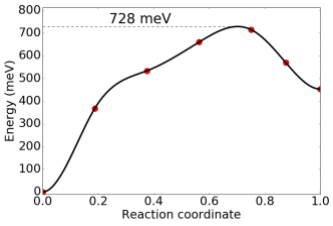

A→B

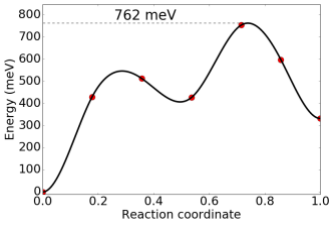

A→C

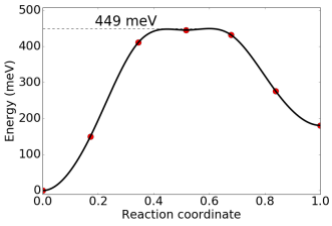

A→D

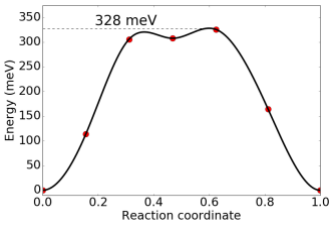

A→E

α_I-$NaVOPO_4$+ v_{Na+}

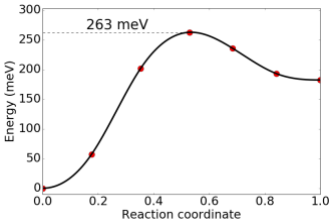

A→B

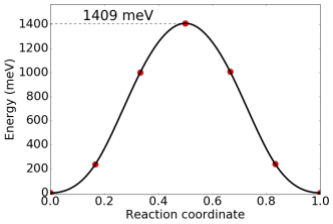

A→C

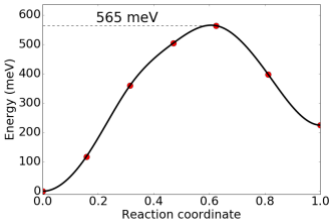

A→D

α_I-$NaVOPO_4^*$+ v_{Na+}

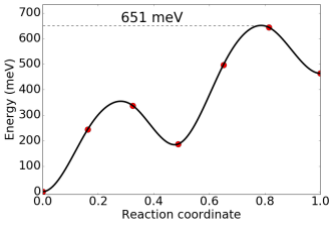

A→B

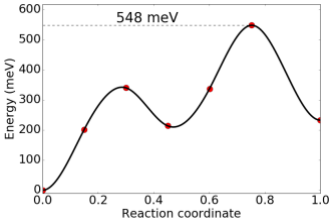

A→C

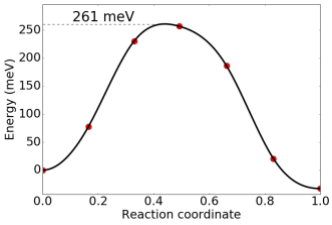

A→D

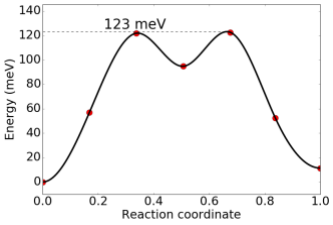

A→E

Figure 3.11 Calculated CI-NEB migration barriers in A_xVOPO_4 polymorphs (A=Li and Na; x=0 and 1). The labels are associated with those in Table 3.2. (Continued)

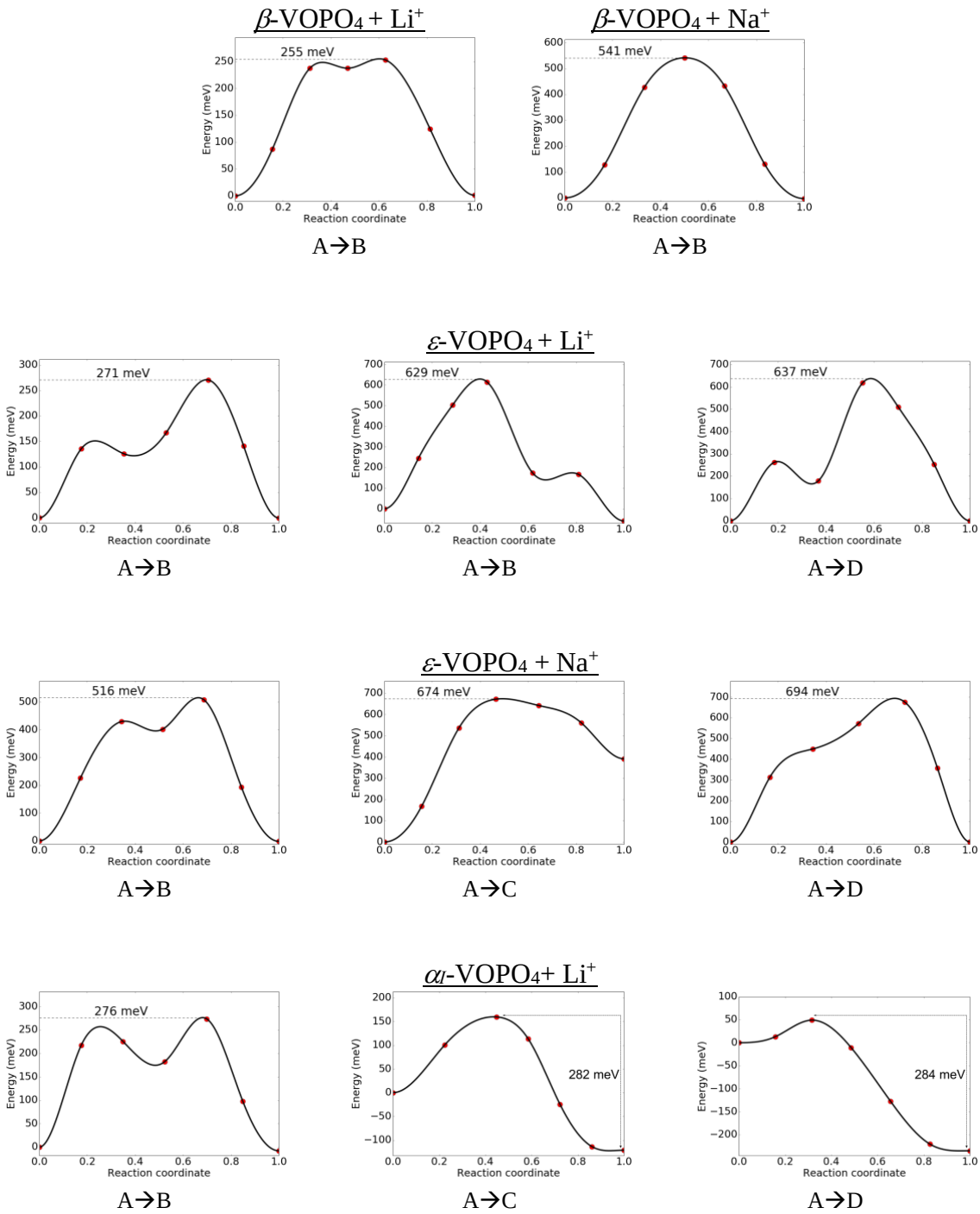

Figure 3.11 Calculated CI-NEB migration barriers in A_xVOPO_4 polymorphs (A=Li and Na; x=0 and 1). The labels are associated with those in Table 3.2. (Continued)

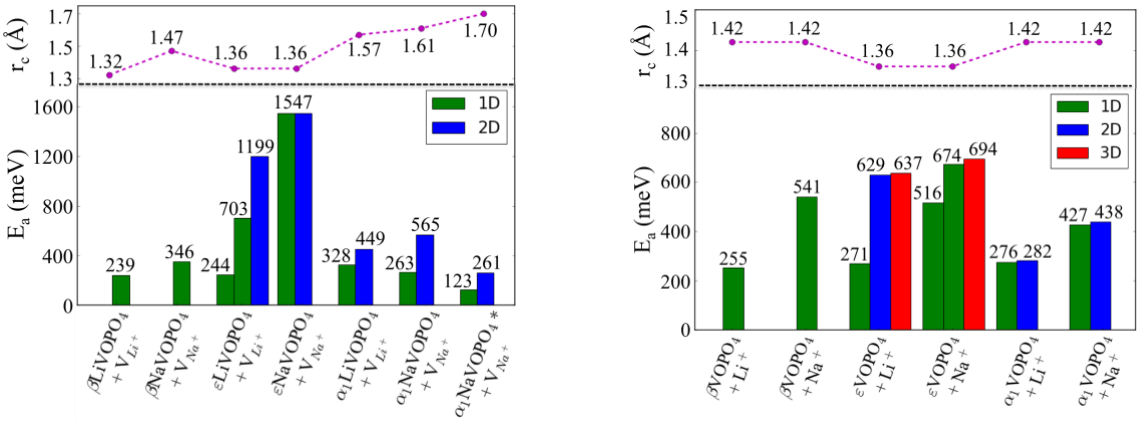

(a) (b)

Figure 3.12 Calculated bottleneck size (top) and migration barriers (bottom) of (a) v_{A+} in $AVOPO_4$, and (b) A^+ in $VOPO_4$ in which bottleneck size and migration barrier are denoted as r_c and E_a, respectively. α_I-$NaVOPO_4$ with the same alkali ordering as the α_I-$LiVOPO_4$ is denoted as α_I-$NaVOPO_4^*$. The dashed lines in the bottleneck size plot are drawn only to guide the eyes.

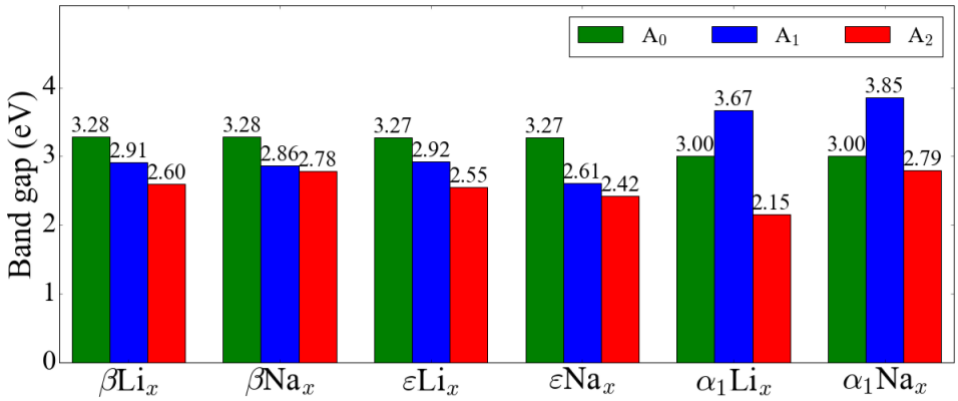

Figure 3.13 Calculated band gaps from the HSE density of states of A_xVOPO_4 polymorphs (x = 0, 1, 2).

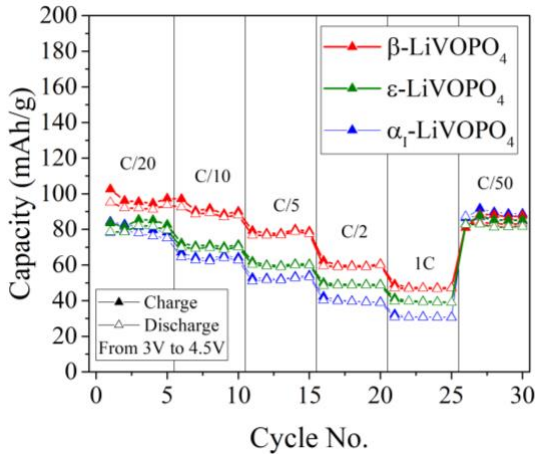

Figure 3.14 Electrochemical performance of $LiVOPO_4$ polymorphs at different current densities.

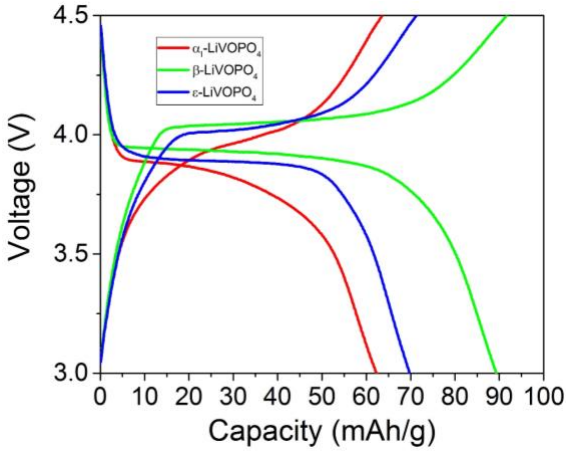

Figure 3.15 Galvanostatic charge-discharge curves for different $LiVOPO_4$ polymorphs at a charge-discharge rate of C/10.

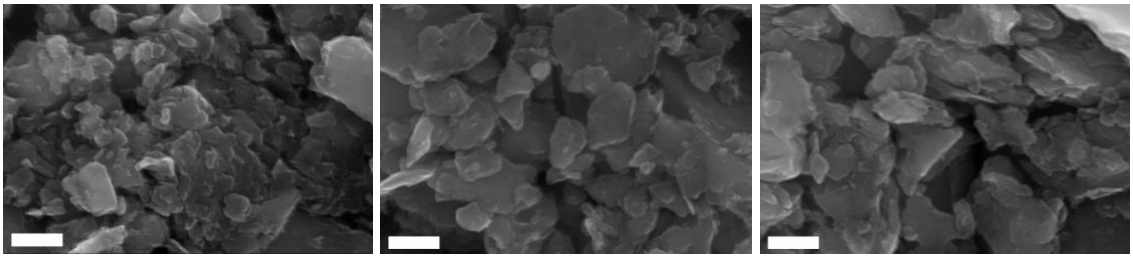

Figure 3.16 SEM images of (left to right) β-, ε-, and α_I- $LiVOPO_4$ after ball-milling. Scale bars are 200 nm.

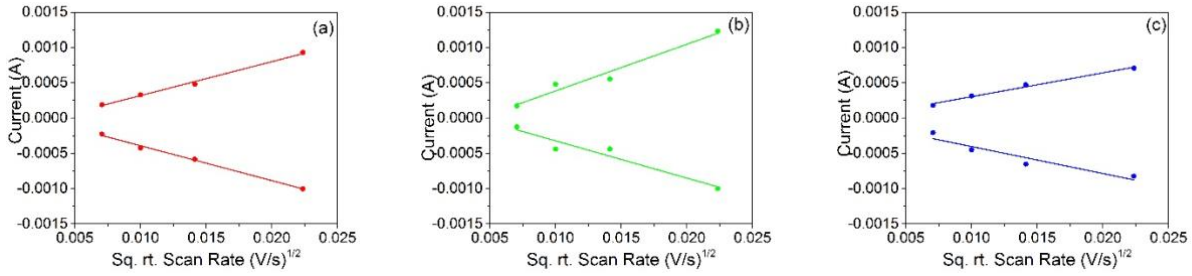

Figure 3.17 Current vs $v^{1/2}$ plots for the high-voltage transformation in (a) α_I-, (b) β-, and (c) ε-$LiVOPO_4$.

Table 3.3 Apparent diffusion coefficients from CV data.

Phase	Diffusion Coefficient (10^{-11} cm^2 s^{-1})	
	$x = 1$ (Li vacancy diffusion)	$x = 0$ (Li ion diffusion)
β-Li_xVOPO_4	11 ± 3	7 ± 3
ε-Li_xVOPO_4	3 ± 1	4 ± 2
α_I-Li_xVOPO_4	6 ± 1	6 ± 1

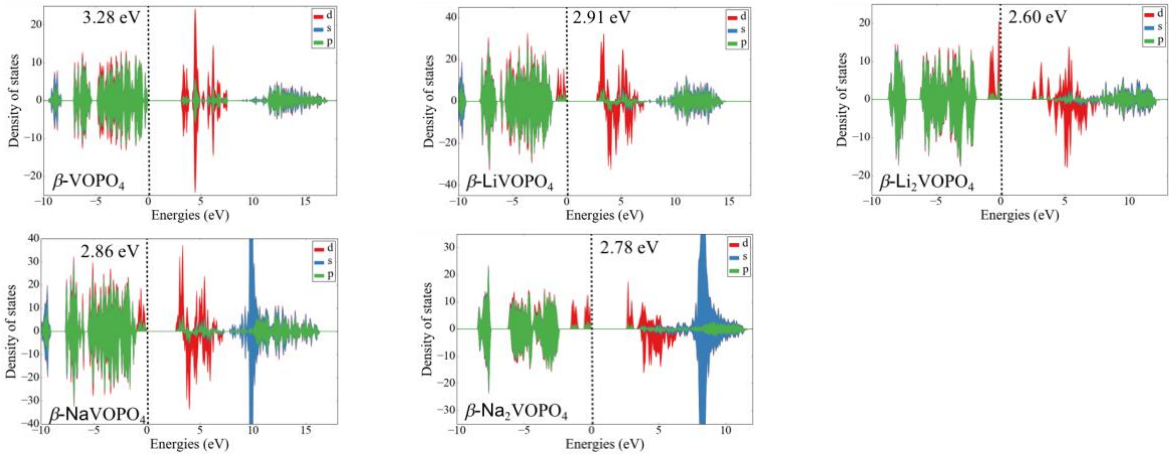

(a) β-A_xVOPO_4

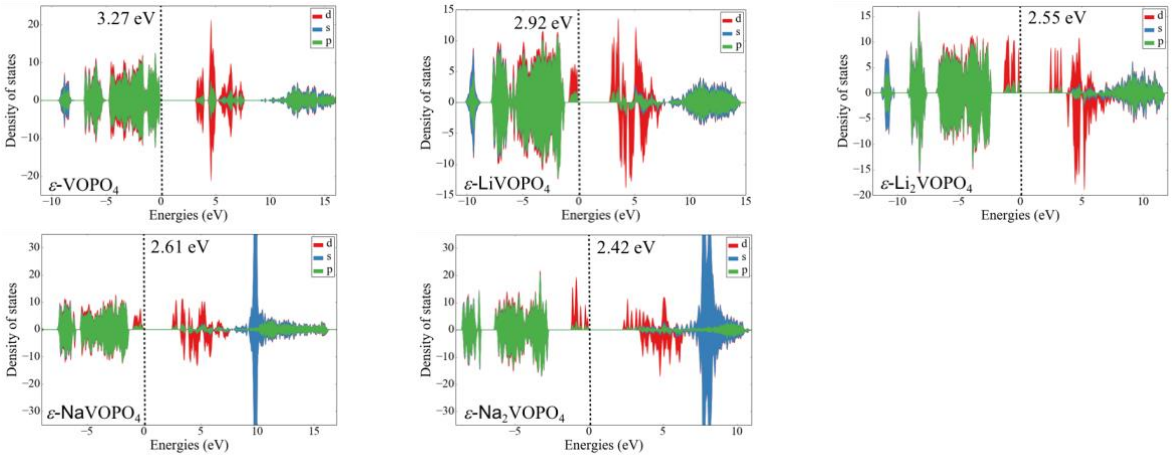

(b) ε-A_xVOPO_4

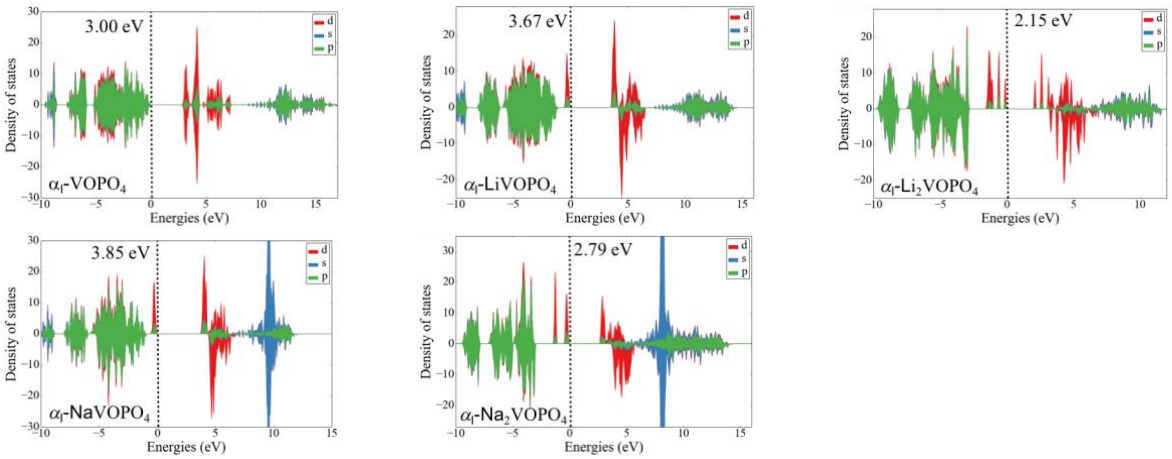

(c) α_I-A_xVOPO_4

Figure 3.18 Calculated hybrid HSE density of states of A_xVOPO_4 polymorphs (A=Li and Na; x=0, 1, 2). The computed band gaps are also labeled in the each of the sub-figures.

Chapter 4. Rational Synthesis and Electrochemical Performance of $LiVOPO_4$ Polymorphs

4.1 Introduction

Li-ion batteries utilizing intercalation chemistry are currently the most prominent form of energy storage for portable electronic devices and electric vehicles due to their high energy density.[162–167] Unfortunately, the capacity of most commercially available cathode materials is limited by the fact that the cathode material can only store up to one Li^+ ion per redox center. Thus, there is a large interest in materials which can intercalate multiple electrons per redox center.[168–175] One such material is lithium vanadyl phosphate, or $LiVOPO_4$.[29,176,177] The V^{5+}/V^{4+} and V^{4+}/V^{3+} redox couples at 4.0 V and 2.5 V, respectively, allow for the intercalation of up to two Li^+ ions per vanadium through the formation of $VOPO_4 \leftrightarrow LiVOPO_4 \leftrightarrow Li_2VOPO_4$ during the operation of the battery. This results in a high theoretical capacity of 305 mAh/g and a specific energy of over 900 Wh/g.[30,178,179]

Three major polymorphs of $LiVOPO_4$, α_I-, β-, and ε-$LiVOPO_4$, have been previously reported and synthesized through different methods. The α_I phase (tetragonal, P4/nmm)[27,180–182] has a layered structure exhibiting 2D Li diffusion, and is the least reported among the different polymorphs due to difficulties in its synthesis. On the other hand, the β phase (orthorhombic, Pnma)[183–185] has 1D diffusion channels while the ε phase (triclinic, P-1)[29,33,184,186,187] has pseudo-1D diffusion channels. Unlike α_I, both the β and ε phases have been synthesized using a large plethora of methods, including hydrothermal,[29–31] solid-state,[31–33]and sol-gel.[32,34]

A complete understanding of the differences between these phases is essential to identifying which polymorph is best suited as a cathode material in a Li-ion battery. Thermodynamic calculations have reported previously that α_I is metastable relative to both β and

ε, which have very similar stabilities.[176,187] Additionally, the different phases have been observed and reported either transforming between one another or appearing as impurities.[34,35,184,188] However, since the difference in stability of these phases is small, minute differences in synthesis would greatly influence the individual properties of the polymorphs. This makes it difficult to conduct a thorough comparison of different properties of the polymorphs.

To address this challenge, we show in this study that all three polymorphs can be synthesized from a single precursor, $LiVOPO_4 \cdot 2H_2O$, through careful control of synthesis conditions. By utilizing a single precursor, it is possible to minimize effects of synthesis on the properties such as stability and electrochemical performance, allowing for more direct and accurate experimental and theoretical comparisons. In addition, we demonstrated that the limitations to the electrochemical performance of $LiVOPO_4$ due to electronic and ionic conductions can be remedied with carbon coating, nano-sizing and morphology control.[29,176] Guided by DFT surface calculations, we demonstrate how control of the O chemical potential may be used to control morphology to promote the formation of facets with facile Li intercalation[189–191] for high rate performance.

4.2 Experimental methods

4.2.1 Synthesis of $LiVOPO_4 \cdot 2H_2O$ and different $LiVOPO_4$ polymorphs

The $LiVOPO_4 \cdot 2H_2O$ precursor was synthesized using a hydrothermal method modified from previous reports.[42] V_2O_5 (Aldrich, >99.6%), oxalic acid (Sigma-Aldrich, >99.0%), and phosphoric acid (Fisher Scientific, 85%) were dissolved in ethanol and water, and stirred for 18 hours. $LiOH \cdot H_2O$ (Sigma, >99.0%) was then added, and stirred for another 4 hours. The solution was hydrothermally synthesized in a 4748 Type 125 mL PTFE-lined reactor (Parr Instrument Co.) and heated to 160 °C for 48 hours. The product was filtered and washed with water, ethanol, and

acetone, then dried overnight at 60 °C. The precursor was heated to different temperatures and environments for 3 hours in order to form the different $LiVOPO_4$ polymorphs. Specifically, α_I-$LiVOPO_4$ forms at 300 °C in Ar, β-$LiVOPO_4$ forms at 600 °C in O_2, and ε-$LiVOPO_4$ forms at 750 °C in Ar. Amorphized $LiVOPO_4 \cdot 2H_2O$ was prepared by subjecting the precursor to high-energy ball-milling for 30 minutes.

4.2.2 Materials characterization

Powder X-ray diffraction (XRD) data was collected using a Bruker D8 Advance diffractometer utilizing a Cu $K\alpha$ source ($K\alpha 1$ = 1.54053 Å, $K\alpha 2$ = 1.54431 Å) over the 2θ range of 10 ° – 80 ° and a step size of 0.02 °. Indexing, phase identification, and Rietveld refinement were conducted using the TOPAS software package (Bruker AXS, version 5.0) and the PDF-2015 software package. Thermogravimetric analysis coupled with mass spectrometry (TG-MS) was performed using a TG 209 F1 Iris coupled to a QMS 403 Aeolos Mass Spectrometer (260-TG/MS Netzsch). In-situ diffraction data were collected using high-energy X-rays (λ = 0.2113 Å) provided by beamline 11-ID-B at the Advanced Photon Source, Argonne National Laboratory. Diffraction images were recorded in transmission geometry using an amorphous Si detector, and integrated with GSAS-II[40] using a CeO_2 standard (SRM674b) as calibrant. Powder samples were loaded in quartz capillaries and slightly compressed between two plugs of quartz wool. Capillaries were placed in the flow-cell/furnace[41] and O_2 or He was flown (4 cc/min) through the capillary during the heating. When He was flown through the cell, a residual gas analyzer (Pfeiffer PrismaPlus QMG 220 M2 mass spectrometer) was attached to the outlet to monitor released gases. Transmission electron microscopy was conducted by dispersing the as-synthesized β- or ε-$LiVOPO_4$ particles in ethanol, sonicating thoroughly, and then dropping the solution onto the carbon film coated copper grid. Microstructure characterization was performed on a Talos F200X

S/TEM (Thermo fisher Scientific, USA) equipped with a field emission gun (FEG) operated at accelerating voltage of 200 kV.

4.2.3 Electrochemical Performance Testing

Electrochemical performance was evaluated by using the $LiVOPO_4$ as a cathode material in 2325-type coin cells. The cathodes were prepared by first subjecting the $LiVOPO_4$ with graphene to high-energy ball-milling for 30 minutes. Polyvinyldiene fluoride (PVDF) was then added to the mixture, resulting in an $LiVOPO_4$:graphene:PVDF ratio of 75:15:10, and formed into a slurry using n-methyl-2-pyrrolidinone (NMP) as the solvent. The slurry was cast onto a carbon-coated Al foil and dried at 60 °C. Electrodes with areas of 1.2 cm^2 and active mass loadings of ~2.5 – 4.5 mg were punched and served as the cathodes. The cell was assembled with a pure lithium chip (MTI) as the counter and reference electrodes, a Celgard 2400 separator (Hoechst Celanese) as the separator, and 1 M $LiPF_6$ in 1:1 v/v ethylene carbonate (EC) and dimethyl carbonate (DMC) as the electrolyte. The cells were cycled at a rate of C/40 (C defined as 317 mAh/g) using a VMP multichannel potentiostat (Bio-Logic) from 1.5 V to 4.5 V at current densities from 16 – 28 $\mu A/cm^2$. Rate tests were conducted from C/100 up to C/2, then back to C/100, at 5 cycles each. Galvanostatic Intermittent Titration Technique (GITT) runs were conducted by discharging the cells at C/100 for 1.5 hours and letting them rest for 100 hours (high-voltage region) or 50 hours (low-voltage region).

4.3 Computational methods

All first-principles calculations in this work were performed using the Vienna *ab initio* simulation package (VASP) with the projected augmented wave (PAW) method. The Hubbard U extension to the Perdew-Burke-Ernzerhof (PBE) generalized gradient approximation (GGA) functional with a *U* value of 3.25 V for vanadium was adopted,[39,58,59] and all calculations were

initialized in a ferromagnetic high spin configuration given that previous studies have shown that magnetic effects to have a minimal impact on relative energies.[62]A plane wave energy cutoff of 520 eV and k-point density of at least 1000/(number of atoms in the unit cell) were used for bulk relaxations of α_I-, β-, and ε-Li_xVOPO_4 (x = 0, 1). All other parameters are consistent with those used by the Materials Project for all calculations unless stated otherwise.[61] All data analysis was performed using the Python Materials Genomics (pymatgen) library.[56]

4.3.1 Gibbs free energy

Phonon calculations using density functional perturbation theory as implemented in the Phonopy code were carried out for β-, ε- and α_I-Li_xVOPO_4 (x = 0, 1).[192] The Gibbs free energy of each phase was then obtained based on the quasi-harmonic approximation. More stringent energy and force convergence criteria of 10^{-8} eV and 10^{-4} eV/Å, respectively, were used for these calculations.

4.3.2 Defect formation energy

The defect formation energies (E_d) of O-vacancy and O-interstitial defects were calculated using the following equations:

O-vacancy: $E_d = E_{Li_{32}V_{32}P_{32}O_{159}} - E_{Li_{32}V_{32}P_{32}O_{160}} + \Delta\mu_O$

O-interstitial: $E_d = E_{Li_{32}V_{32}P_{32}O_{161}} - E_{Li_{32}V_{32}P_{32}O_{160}} - \Delta\mu_O$

where $\Delta\mu_O = \mu_O - \frac{1}{2}\mu_{O2}^0$ being the oxygen chemical potential relative to μ_{O2}^0 (the reference chemical potential of O_2 gas at standard temperatures and pressure). The defect concentration of 3.125% was simulated by creating (vacancy or interstitial) defects in a 2 × 2 × 2 supercell for β- and ε-Li_xVOPO_4 and 4 × 2 × 2 supercell for α_I-Li_xVOPO_4 (x = 0, 1). The structure was relaxed until the energy and forces are converged to 10^{-4} eV and 0.05 eV/Å, respectively.

4.3.3 Surface

Surface energies were calculated using the slab method, with the specific implementation and parameters as described in Tran *et al.*[193] Similar to previous work on the $LiFePO_4$ cathode, only non-polar terminations that do no break P-O bonds were investigated.[190,194] Only surfaces up to a max Miller index of 2 were considered, resulting in 29, 18, 19 and 19 facets for ε-$LiVOPO_4$, ε-$VOPO_4$, β-$LiVOPO_4$, and β-$VOPO_4$, respectively. We investigated non-polar, symmetric O adsorption on both surfaces of the slab using the algorithm implemented in pymatgen.[195] Only slabs corresponding to the facets appearing on the clean Wulff shapes of β- and ε-$LiVOPO_4$ were investigated. To calculate the surface energy, we used the surface grand potential:

$$\gamma = \frac{1}{2A}[E^{slab} - \sum_i N_i \mu_i]$$

where E^{slab} is the total energy of the slab with i unique species, μ_i is the chemical potential of a specie i and N_i is the total number of i atoms in the slab. Further details are given in the SI for interested readers.

4.4 Results

4.4.1 Phase transformation upon heating $LiVOPO_4$

Pure-phase $LiVOPO_4 \cdot 2H_2O$ (Figure 4.1) is used as a precursor to form the different polymorphs of $LiVOPO_4$. From thermogravimetric analysis (TGA), we observe that both temperature and atmosphere are key factors which cause different changes within the precursor (Figure 4.2). We can directly identify these specific changes using in-situ XRD while heating $LiVOPO_4 \cdot 2H_2O$ (Figure 4.3) and use Rietveld refinement to quantify the relative amounts of each $LiVOPO_4$ polymorph at each specific temperature (Figure 4.4). Two major observations can be made. Firstly, we observe that heating $LiVOPO_4 \cdot 2H_2O$ results in the formation of α_I-$LiVOPO_4$,

followed by β-$LiVOPO_4$, then ε-$LiVOPO_4$. This trend is seen in both Ar and O_2. Secondly, we observe that a large amount of β-$LiVOPO_4$ can only form in an oxidizing atmosphere.

Ex-situ XRD of heated $LiVOPO_4 \cdot 2H_2O$ (Figure 4.5) and Rietveld refinement of these spectra (Figure 4.6) also show similar trends, where $LiVOPO_4 \cdot 2H_2O \rightarrow \alpha_I$-$LiVOPO_4 \rightarrow$ β-$LiVOPO_4 \rightarrow$ ε-$LiVOPO_4$, and higher amounts of β-$LiVOPO_4$ only form when the samples are heated in an oxidizing atmosphere. In fact, heating $LiVOPO_4 \cdot 2H_2O$ at 600 °C in Ar, air, and O_2 results in 48%, 93%, and 97% β-$LiVOPO_4$, respectively, with the remainder being ε-$LiVOPO_4$. The ex-situ runs also show that these phases are stable upon cooling, with the final phases with highest purity (Figure 4.7) taken for further testing.

The $LiVOPO_4 \cdot 2H_2O$ to α_I-$LiVOPO_4$ transformation can be attributed to fact that the α_I-$LiVOPO_4$ structure is analogous to the $LiVOPO_4 \cdot 2H_2O$ structure (Figure S6), but without the water and with a slight shift in the Li position.[27] At higher temperatures, the lack of α_I-$LiVOPO_4$ and the presence of β- and ε-$LiVOPO_4$ are in agreement with ex-situ heating of α_I-$LiVOPO_4$. This shows that α_I-$LiVOPO_4$ transforms into both β- and ε-$LiVOPO_4$ (Figure 4.9 & Figure 4.10) at these higher temperatures. Additionally, it is observed that the reverse reaction, that is, the transformation of β- and ε-$LiVOPO_4$ into α_I-$LiVOPO_4$, is not possible (Figure 4.11) In fact, when α_I-$LiVOPO_4$ is kept at 300 °C in Ar (the conditions for the $LiVOPO_4 \cdot 2H_2O \rightarrow \alpha_I$-$LiVOPO_4$ transformation) for extended periods, it slowly transforms into a mixture of β- and ε-$LiVOPO_4$. All these observations suggest that α_I-$LiVOPO_4$ is metastable relative to β- and ε-$LiVOPO_4$.

Figure 4.12 presents the calculated Gibbs free energies of α_I-, β-, and ε-$LiVOPO_4$ within the temperature range of 0 – 1000 K. We observe that the Gibbs free energies of ε-$LiVOPO_4$ and β-$LiVOPO_4$ are almost degenerate (within 3 meV/atom of each other) and much lower than that of α_I-$LiVOPO_4$ at all temperatures of interest. This clearly indicates that the α_I phase is the most

unstable phase, which is consistent with our experimental observations and previously reported calculations.[16,29]

The phase distribution when heated for extended periods in Figure 4.13 shows that β-$LiVOPO_4$ readily transforms into ε-$LiVOPO_4$ when heated at 750 °C in Ar. Similarly, ε-$LiVOPO_4$ also transforms into β-$LiVOPO_4$ when heated at 600 °C in O_2, albeit at a slower rate.

4.4.2 Role of Oxygen in the Phase Stability of the $LiVOPO_4$ Polymorphs

It is observed in both in-situ and ex-situ heating of $LiVOPO_4 \cdot 2H_2O$ that the presence of O_2 in the atmosphere during heating has a drastic effect on the relative ratios of β- and ε-$LiVOPO_4$. This effect of O_2 on stability can be more clearly demonstrated when heating amorphized $LiVOPO_4 \cdot 2H_2O$. Figure 4.14 shows that, when heated to 600 °C, amorphized $LiVOPO_4 \cdot 2H_2O$ forms β-$LiVOPO_4$ in O_2 or ε-$LiVOPO_4$ in Ar. This result shows that, independent of temperature, the preferential formation of β- or ε-$LiVOPO_4$ is largely dictated by the presence of O_2 in the atmosphere.

In order to further understand the effect of O_2 on the stability of these phases, we monitored the changes in the XRD patterns (Figure 4.15), weight (Figure 4.17), and release of gasses (Figure 4.16 & Figure 4.17) as β-$LiVOPO_4$ transforms into ε-$LiVOPO_4$. We observe from our in-situ XRD data that the onset of the β-to-ε transformation at around 630 °C matches well with the onset of O_2 release, as detected by the RGA (Figure 4.16). Additionally, the O_2 signal diminishes once the maximum amount of ε-$LiVOPO_4$ is formed. This alignment of the XRD and RGA data show that the formation of ε-$LiVOPO_4$ and the release of O_2 are related. Similarly, the loss of O_2 can be detected and quantified using a TG-MS. The maximum weight loss coincides with the maximum amount of detected O_2 loss, both at around 650 °C. This fits with the observations made from the β-to-ε in-situ XRD. Additionally, the thermogram shows that the amount of O_2 lost during heating

is ~0.078% of the total weight, which is ~0.0065 moles of O per mole of $LiVOPO_4$. These suggest that ε-$LiVOPO_4$ has more O-vacancies than β-$LiVOPO_4$, and that these vacancies affect the stability of both phases.

Figure 4.18 presents the calculated defect formation energies of O vacancies and interstitials in β- and ε-$LiVOPO_4$ relative to $\Delta\mu_O$. We find that at low oxygen chemical potentials (higher temperatures, reducing atmosphere), the most stable defect structure is that of ε-$LiVOPO_4$ with oxygen vacancies. Conversely, at high oxygen chemical potentials (lower temperatures, O_2 atmosphere), the most stable defect structure is that of β-$LiVOPO_4$ with oxygen interstitials.

The calculated dopant formation energies of O-vacancies in β-$LiVOPO_4$ are larger than that of ε-$LiVOPO_4$, while the energies of the O-interstitials of β-$LiVOPO_4$ are lower than that of ε-$LiVOPO_4$. These findings suggest that β-$LiVOPO_4$ is more likely to form in the presence of O-interstitials, and ε-$LiVOPO_4$ is preferred in the presence of O-vacancies. These calculation results are consistent with the experimental observations above.

4.4.3 Surface stability of $LiVOPO_4$ polymorphs

For β- and ε-$LiVOPO_4$, all facets remain non-polar after structural relaxations. It is shown that LiO_6 and VO_6 octahedral are cut through, leading to undercoordinated Li and V atoms on the surface in each orientation. The lowest-energy structures of each facet are provided in CIF format in Table 4.1.

Figure 4.19 plots the fractional areas of the different facets on the Wulff shape against $\Delta\mu_O$ for β- and ε-$LiVOPO_4$ along with insets of the Wulff shapes constructed based on surface energies in Figure 4.20. For a max Miller index of 2, there are 19 and 29 symmetrically distinct facets for the clean β- and ε-$LiVOPO_4$, respectively. However, only 11 and 12 of these facets are thermodynamically stable on the Wulff shapes of clean β- and ε-$LiVOPO_4$, respectively. The

calculated surface energies for most facets of β-$LiVOPO_4$ are on somewhat higher than those reported in a recent work by Li *et al.*[191], and we attribute these differences to slightly different parameter settings. One exception is the (101) facet of β-$LiVOPO_4$, which we calculate to be 0.98 J/m^2, (0.42 J/m^2 lower than the value reported by Li *et al*.). We also find that the (121), (102), (212), (211), (221), and (112) facets, which were not considered by Li *et al*., to contribute to the Wulff shape of clean β-$LiVOPO_4$ as well.

The Wulff shape of β-$LiVOPO_4$ becomes more anisotropic as $\Delta\mu_O$ increases, finally forming a rectangular rod under extreme oxidizing conditions enclosed by the (001), (100), and (010) planes. A similar behavior in the evolution of the Wulff shape for ε-$LiVOPO_4$ is observed as the fractional area of the (100) facet sharply increases as $\Delta\mu_O$ increases beyond -3 eV.

In Figure 4.21, TEM images of the particles of β- and ε-$LiVOPO_4$ show that the β-$LiVOPO_4$ is enclosed at the top by the (001) plane and to the sides with the (010) and (100) planes while ε-$LiVOPO_4$ is enclosed at the top by the (100) plane, both of which are in excellent agreement with the dominant facets on calculated Wulff shapes. However, the (210) facet which is present in the experimental particle morphology is not present in the Wulff shape evolution of β-$LiVOPO_4$ (Figure 4.19(a)).

4.4.4 Surface redox potentials

Table 4.2 shows the calculated redox potentials to extract Li from different facets on the Wulff shape of $LiVOPO_4$. The surface potentials vary from 4.51 to 3.03 V and 4.63 to 3.12 V for β-$LiVOPO_4$ and ε-$LiVOPO_4$, respectively. The calculated bulk redox potentials for β-$LiVOPO_4$ and ε-$LiVOPO_4$ are 3.83 and 3.80 V, respectively, which are in good agreement with the experimental voltage of ~4.0 V.[21,31,51]

4.4.5 Comparison of electrochemical performance of $LiVOPO_4$ polymorphs

Figure 4.22a shows the charge-discharge curve of the first cycle of each of the $LiVOPO_4$ polymorphs. We can observe that β-$LiVOPO_4$ has the highest capacity among the different phases, which may be attributed to its better kinetics,[16] and the higher rate capability on the surfaces of β-$LiVOPO_4$ as seen in the longer high-voltage plateau,. This larger capacity is maintained over several cycles, as seen in Figure 4.22b. Figure 4.23 also shows that the experimental voltage of each plateau for both the high- and low-voltage regions also fits well with theoretical voltage calculations which we reported previously.[176]

The high-voltage rate capability test in Figure 4.24a shows that all three phases experience the expected capacity loss as they are cycled at higher rates, and regain this lost capacity when cycled at lower rates. This is in agreement with the GITT data in Figure 4.24b, which shows that each phase experiences comparable voltage changes when reaching equilibrium upon rest. A similar analysis can be conducted in the low-voltage region, shown in Figure 4.25a. First, we observe that α_I-$LiVOPO_4$ experiences a similar loss in capacity when cycled at higher rates. Interestingly, β- and ε-$LiVOPO_4$ show barely any loss of capacity when cycled at higher rates in the low-voltage region. This is also observed in the GITT in Figure 4.25b, where both β- and ε-$LiVOPO_4$ only experience a small overpotential, while α_I-$LiVOPO_4$ experiences a large change in voltage. This indicates that both β- and ε-$LiVOPO_4$ have better kinetics in this low-voltage regime. We also observe for all polymorphs that the low-voltage region nearly reaches the full theoretical capacity, while the high-voltage region is still lacking in capacity.

4.5 Discussion

In summary In our previous study[176], we showed that, in regard to thermodynamic stability, α_I-$LiVOPO_4$ <<< ε-$LiVOPO_4$ ≤ β-$LiVOPO_4$ at 0 K. In this study, we found the phase stability

from 0 – 1000 K exhibits the same trend for the three phases via calculating Gibbs free energies. In particular, β- and ε- $LiVOPO_4$ show little difference in Gibbs free energy, which explains why there is a small amount of ε-$LiVOPO_4$ always involved when synthesizing β-$LiVOPO_4$ at low temperatures in either O_2 or Ar atmospheres. Additionally, the energetics suggests that it might be possible to reversibly transform between these two phases. We can observe this transformation by taking ex-situ XRD of β-$LiVOPO_4$ heated in the conditions used to synthesize ε-$LiVOPO_4$ and vice versa.

We have also clearly shown that O_2 plays an important role in the formation of β-$LiVOPO_4$ over ε-$LiVOPO_4$. The lower O-interstitial formation energy in β-$LiVOPO_4$ indicates that it forms more favorably in O-rich environments. In contrast, ε-$LiVOPO_4$ is the preferred phase in O-deficient environments due to its lower O-vacancy formation energy. Consequently, at high temperatures above 750 ℃ in Ar atmosphere, we can achieve pure ε-$LiVOPO_4$. In addition, we found that the rate of transformation from β-$LiVOPO_4$ into ε-$LiVOPO_4$ at 750 ℃ is much faster than that of the reverse process at 600 ℃. This is likely because the transformation from β-$LiVOPO_4$ into ε-$LiVOPO_4$ via O_2 release at high temperatures is kinetically more favorable than the reverse reaction via O_2 incorporation at low temperatures. Furthermore, the rate of atom rearrangement for transformation is faster at higher temperature.

For β-$LiVOPO_4$, we found that (001), (100), and (010) are the dominant facets on the Wulff shape under extreme oxidizing conditions, which are confirmed via TEM. In addition, we found that the (100) and (010) facets have redox potentials of 3.18 V and 3.71 V, respectively, lower than the 3.83 V of the bulk, in agreement with the results reported by Li *et al.*[191] The lower surface redox potentials can lead to easier Li-ion extraction and hence increasing the surface area of these two facets in oxidizing environments would facilitate the rate capability of β-$LiVOPO_4$ on the

surface. In contrast, the dominant facet of ε-$LiVOPO_4$ is (100) under the extreme oxidizing condition, which has a redox potential of 3.82 V, higher than 3.80 V of bulk. This indicates oxidizing atmosphere is likely with little effect on improving the performance of ε-$LiVOPO_4$. The improved rate capability of β-$LiVOPO_4$ on the surface along with its better ionic kinetics[176] may explain why it achieves the best electrochemical performance among the three phases studied.

4.6 Conclusion

In summary, we conducted a thorough study on the effects of temperature and environment on the stability and formation of the different polymorphs of $LiVOPO_4$ using a single precursor, $LiVOPO_4 \cdot 2H_2O$ (Figure 4.26). Heating the precursor resulted in the following transformation: α_I-$LiVOPO_4 \rightarrow$ β-$LiVOPO_4 \leftrightarrow$ ε-$LiVOPO_4$. The phase stability from 0 – 1000 K via Gibbs free energy calculations for the three phases is: α_I-$LiVOPO_4$ <<< ε-$LiVOPO_4 \leq$ β-$LiVOPO_4$, which is consistent with the experimental phase transformation process. The higher O-interstitial and lower O-vacancy defect formation energies of β-$LiVOPO_4$ and ε-$LiVOPO_4$, respectively, indicate that β-$LiVOPO_4$ and ε-$LiVOPO_4$ preferentially form in O-rich and O-deficient environments, respectively. Consequently, we can achieve the largest amount of β-$LiVOPO_4$ phase in oxidizing atmospheres and pure ε-$LiVOPO_4$ phase in Ar atmospheres at high temperatures (> 750 °C). The evolution of Wulff shapes with O chemical potentials indicates that only the surface rate performance of β-$LiVOPO_4$ can be improved by synthesis under O-rich environments. The calculated dominant facets of β-, and ε-$LiVOPO_4$ are further verified on the experimental particle morphologies by TEM. Finally, extensive electrochemical testing shows that of the three $LiVOPO_4$ phases, the β phase is the most promising cathode material with the highest capacity and best rate capability. This may be attributed to its superior ionic kinetics and rate performances on the surfaces as the particle size approaches the nanoscale.

Chapter 4 is, in full, is a preprint currently being prepared for submission for publication of the material “Rational Synthesis and Electrochemical Performance of $LiVOPO_4$ Polymorphs”, Marc F. V. Hidalgo, Yuh-Chieh Lin, Antonin Grenier, Dongdong Xiao, Richard Tran, Huolin Xin, Jennifer Donohue, Fredrick O. Omenya, Iek-Heng Chu, Zhenbin Wang, Xiangguo Li, Natasha A. Chernova, Karena W. Chapman, Guangwen Zhou, Shyue Ping Ong, and M. Stanley Whittingham. The dissertation author was a co-primary investigator and author of this paper. All calculations and corresponding data analysis were done by the author. The experimental portion of the work – synthesis, characterization and data analysis were done by collaborator, M. F. V. Hidalgo.

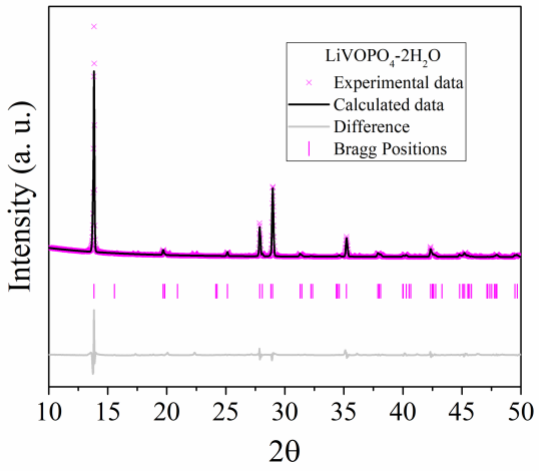

Figure 4.1 Rietveld refinement of as-synthesized $LiVOPO_4 \cdot 2H_2O$.

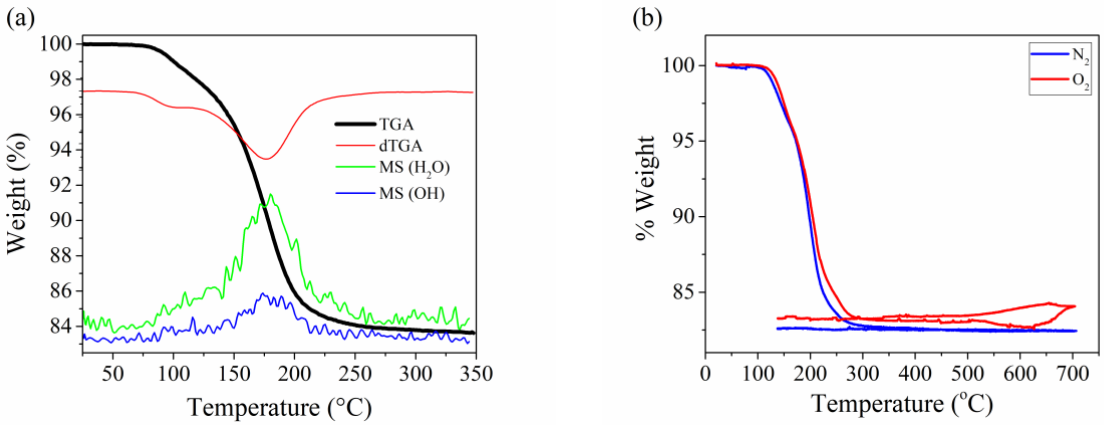

Figure 4.2 Thermal studies of $LiVOPO_4 \cdot 2H_2O$ via (a) TG-MS in Ar, showing loss of water, and (b) TGA in different atmospheres.

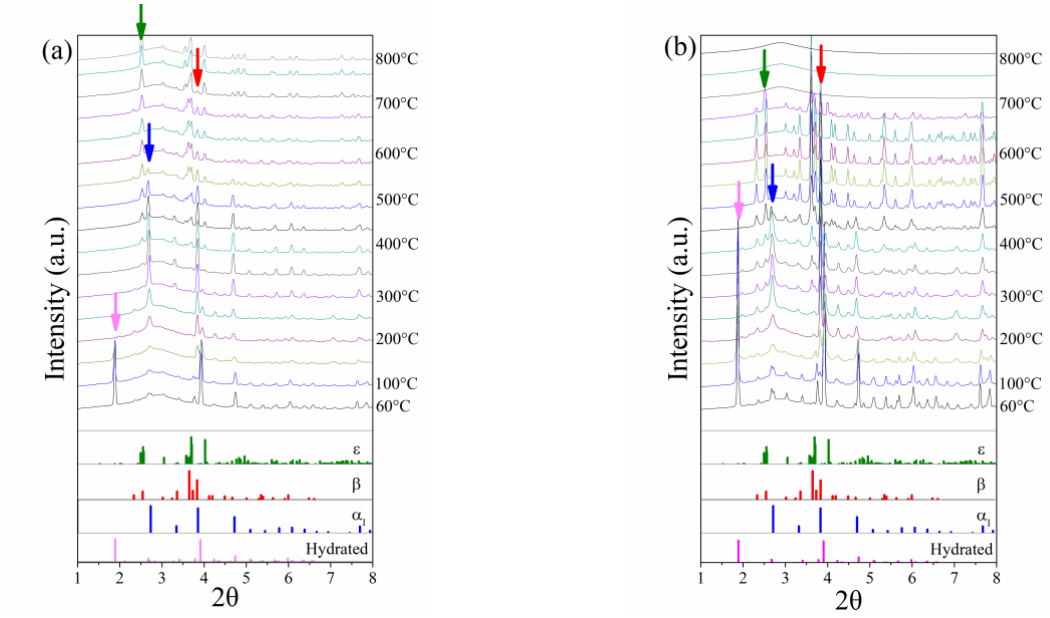

Figure 4.3 In-situ XRD of heated $LiVOPO_4 \cdot 2H_2O$ in (a) He and (b) O_2, with arrows showing characteristic peaks for each polymorph.

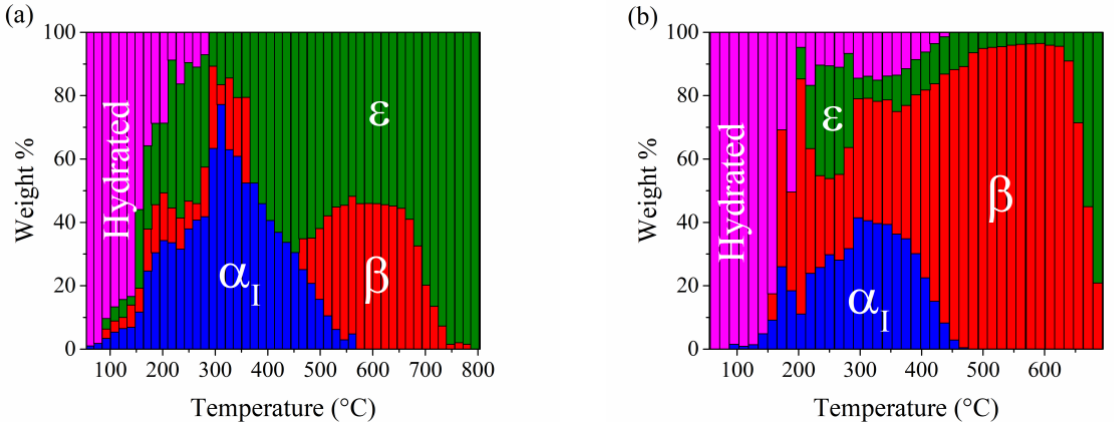

Figure 4.4 Phase quantification of in-situ XRD of $LiVOPO_4 \cdot 2H_2O$ heated in (a) He and (b) O_2.

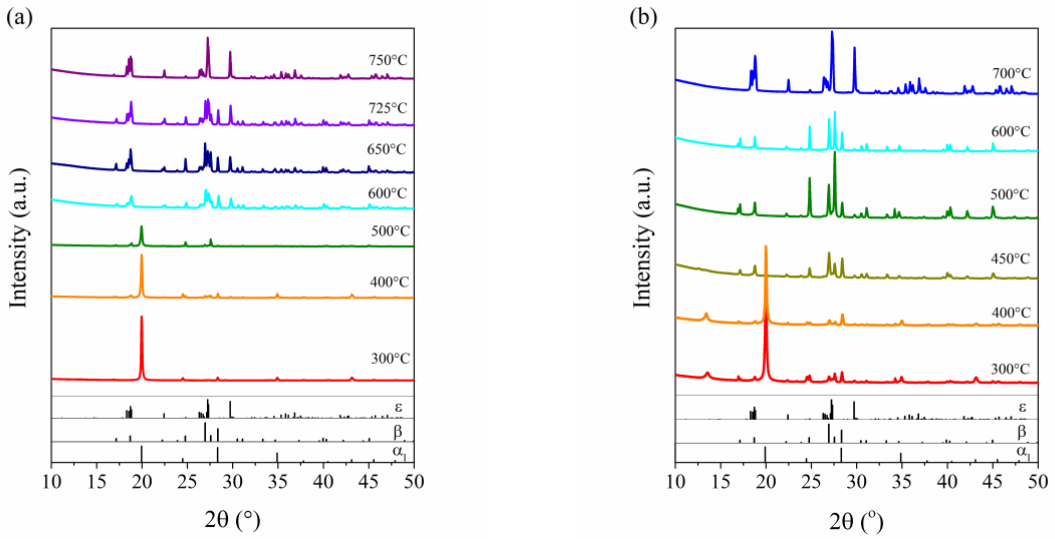

Figure 4.5 Ex-situ XRD of heated $LiVOPO_4 \cdot 2H_2O$ in (a) Ar and (b) air.

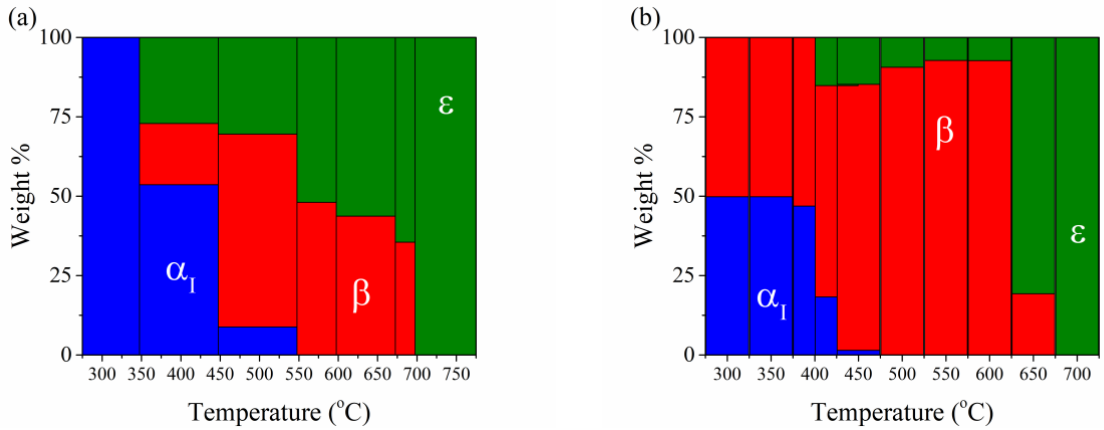

Figure 4.6 Phase quantification of ex-situ XRD of $LiVOPO_4 \cdot 2H_2O$ heated in (a) Ar and (b) air.

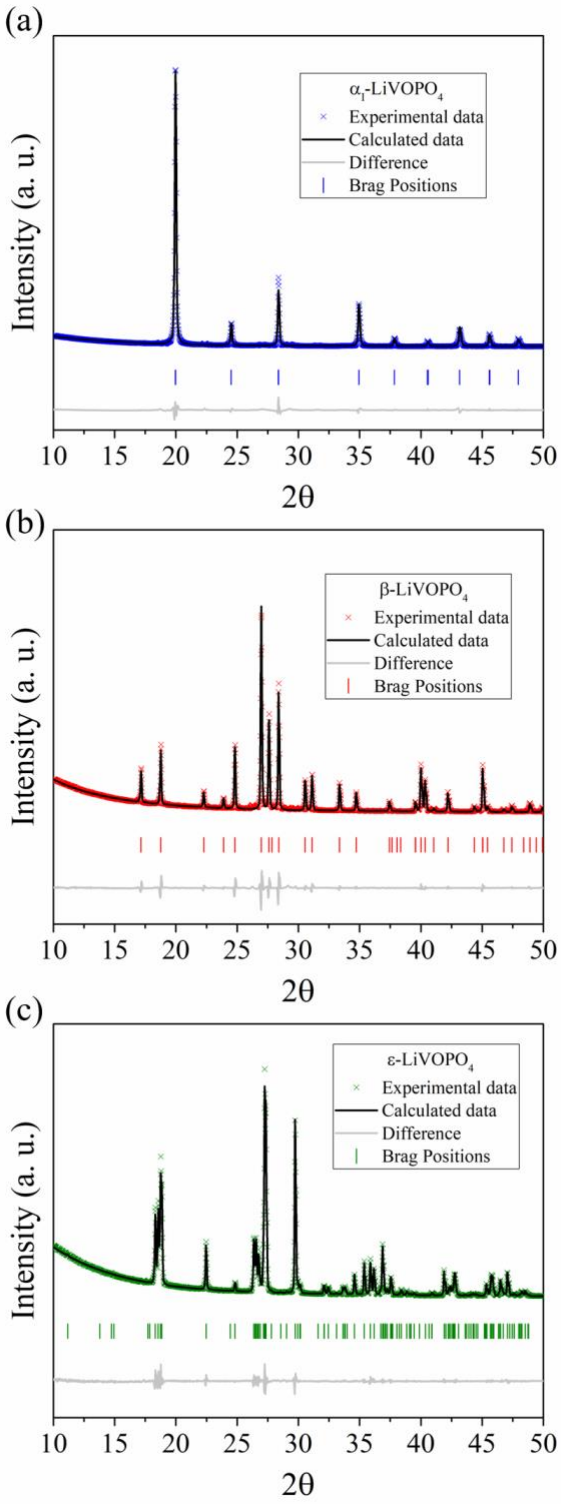

Figure 4.7 Rietveld refinement of purest phase (a) α_I-, (b) β-, and (c) ε-$LiVOPO_4$.

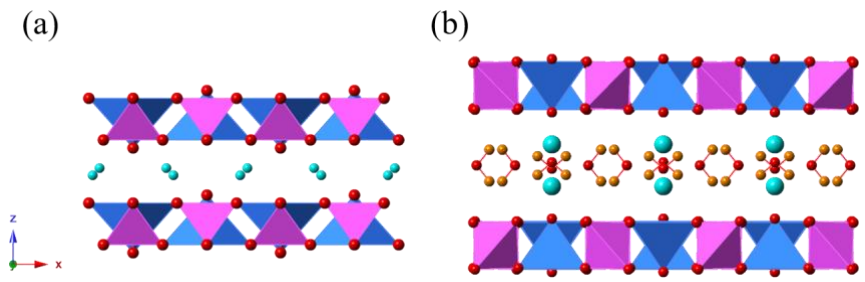

Figure 4.8 Crystal structure of (a) α_I-$LiVOPO_4$ and (b) $LiVOPO_4 \cdot 2H_2O$, showing the orientation of the PO tetrahedral (magenta), VO_6 octahedra (blue), Li (aqua) and water (red and yellow).

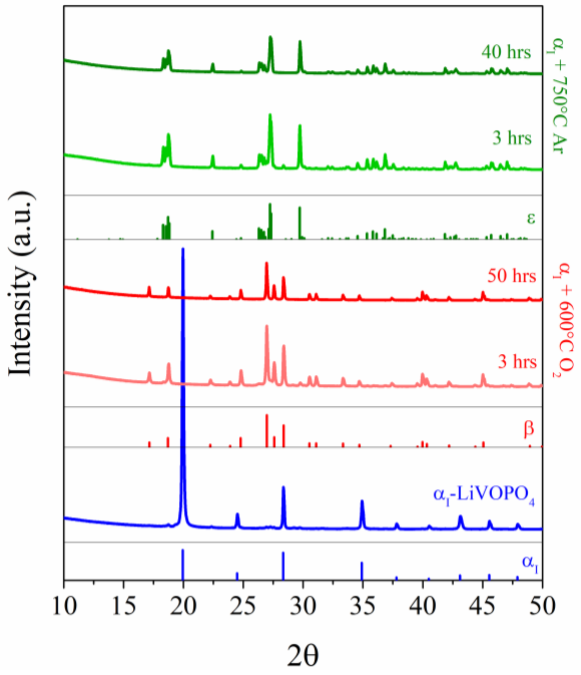

Figure 4.9 XRD patterns of α_I-$LiVOPO_4$ heated in conditions to form β- and ε-$LiVOPO_4$.

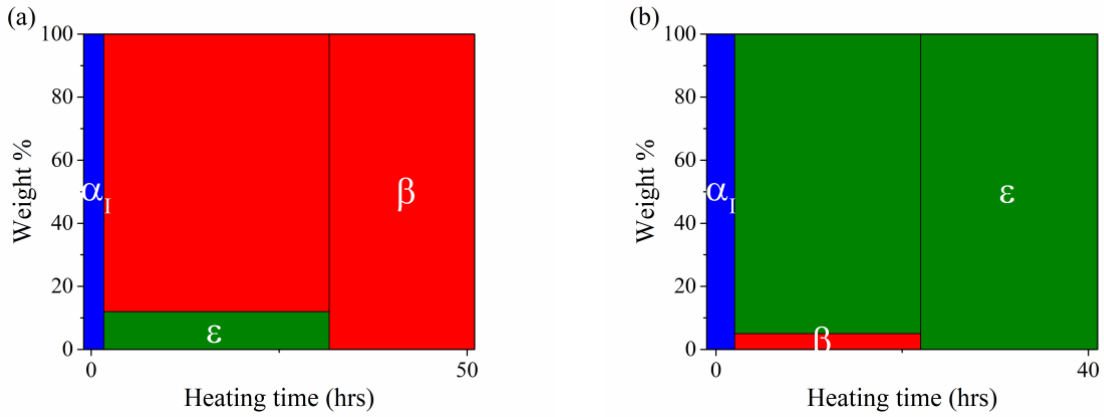

Figure 4.10 Phase quantification showing α_I-$LiVOPO_4$ heated in conditions for the formation of (a) β- (600 °C in O_2) and (b) ε-$LiVOPO_4$ (750 °C in Ar).

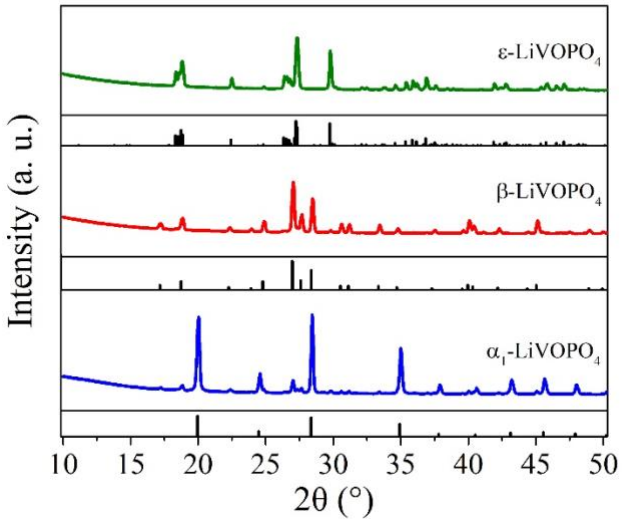

Figure 4.11 XRD of α_I-, β-, and ε-$LiVOPO_4$ heated at conditions for the formation of α_I-$LiVOPO_4$ (300 °C in Ar) for 50 hours.

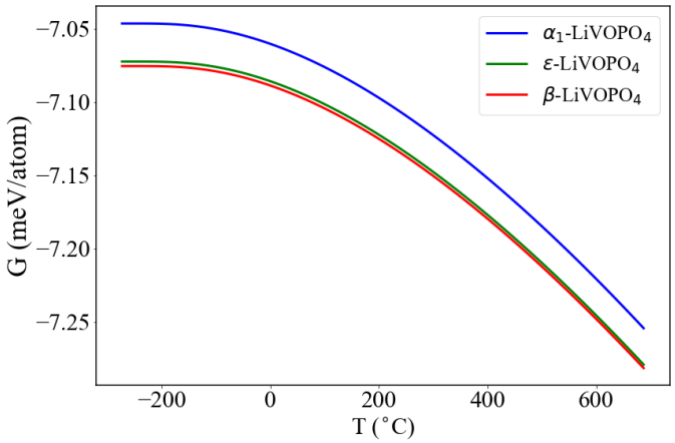

Figure 4.12 Calculated Gibbs free energies (G) of α_I-, β-, and ε- $LiVOPO_4$ as a function of temperature.

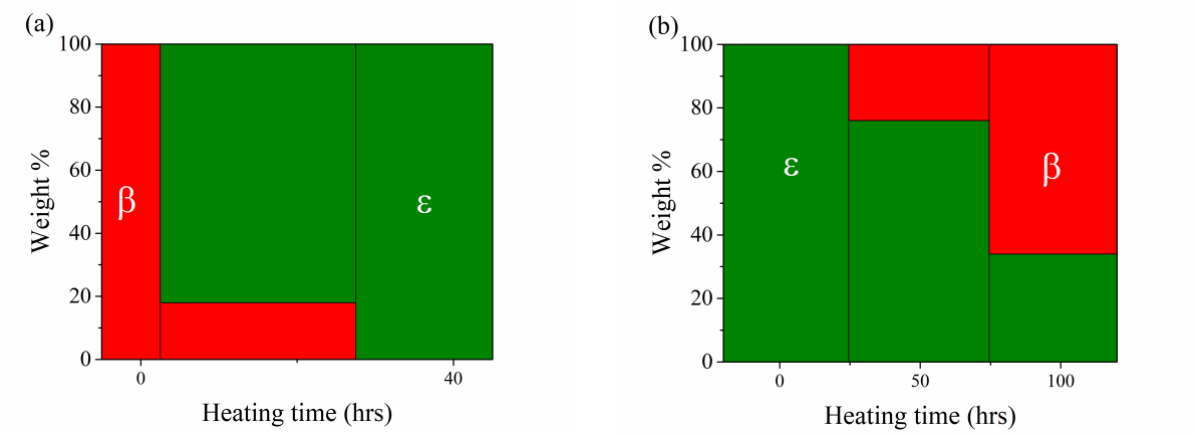

Figure 4.13 Phase quantification of (a) β-$LiVOPO_4$ transformation to ε-$LiVOPO_4$ (750 °C, Ar) and (b) ε-$LiVOPO_4$ transformation to β-$LiVOPO_4$ (600 °C, O_2).

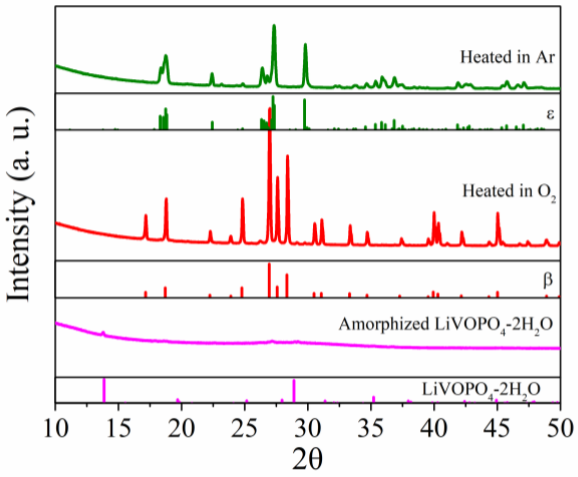

Figure 4.14 XRD of amorphized $LiVOPO_4 \cdot 2H_2O$ before and after heating at 600 °C in different atmospheres.

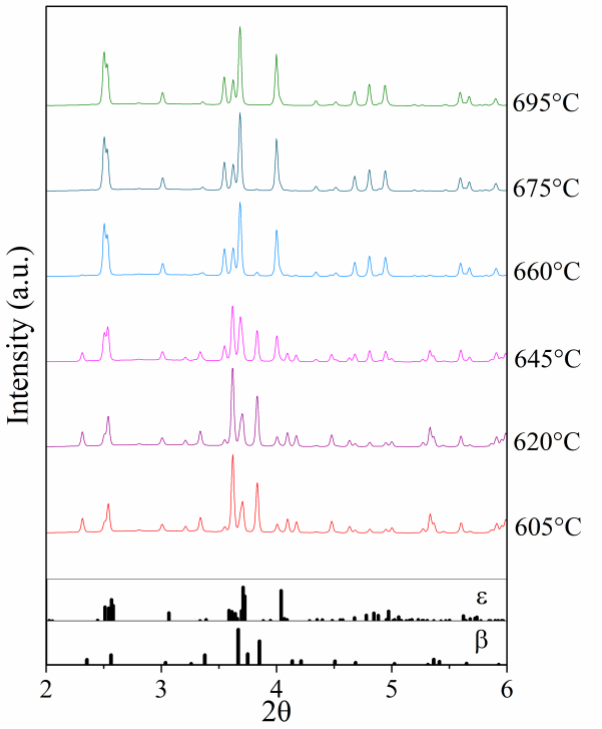

Figure 4.15 In-situ XRD of a mostly β-$LiVOPO_4$ sample heated in He.

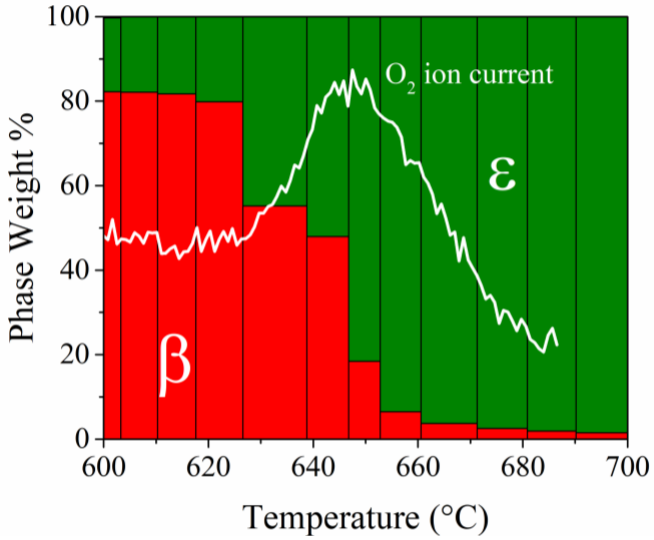

Figure 4.16 Phase quantification of in-situ XRD heating of a majorly β-$LiVOPO_4$ sample in He and RGA signal of O_2.

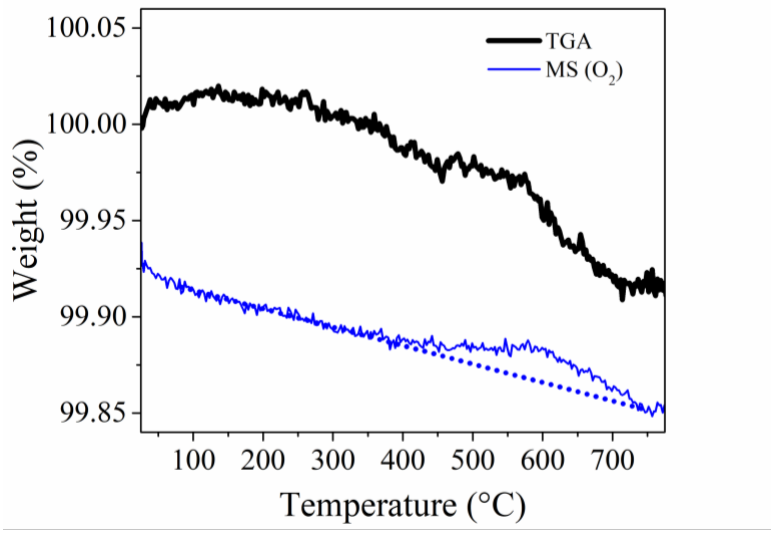

Figure 4.17 TG of β-$LiVOPO_4$ in Ar and coupled MS signal of O_2.

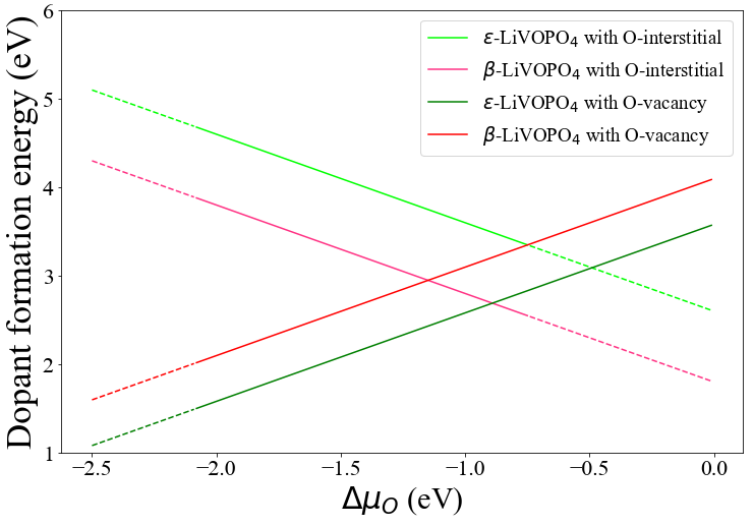

Figure 4.18 Calculated defect formation energies of (a) O-vacancy and (b) O-interstitial for β- and ε-$LiVOPO_4$ with respect to $\Delta\mu_O$. To avoid decomposition of $LiVOPO_4$, $-2.08 < \Delta\mu_O < -0.74$ eV, as indicated by the dash lines.

Table 4.1 Surface energies of symmetrically distinct facets of β- and ε-$LiVOPO_4$ with miller-index < 3.

β-$LiVOPO_4$	
Facet	Surface energy (J/m^2)
(0, 0, 1)	0.656
(0, 1, 0)	0.870
(0, 1, 1)	0.862
(0, 1, 2)	1.111
(0, 2, 1)	1.004
(1, 0, 0)	1.007
(1, 0, 1)	0.976
(1, 0, 2)	0.864
(1, 1, 0)	1.276
(1, 1, 1)	1,132
(1, 1, 2)	0.922
(1, 2, 0)	1.206
(1, 2, 1)	0.957
(1, 2, 2)	1.128
(2, 0, 1)	1.103
(2, 1, 0)	1.205
(2, 1, 1)	1.009
(2, 1, 2)	0.908
(2, 2, 1)	0.976

ε-$LiVOPO_4$	
Facet	Surface energy (J/m^2)
(0, 0, 1)	1.279
(0, 1, 0)	1.299
(0, 1, 1)	1.265
(0, 1, 2)	1.003
(0, 2, 1)	1.097
(1, $\bar{1}$, 0)	0.996
(1, $\bar{1}$, 1)	1.102
(1, $\bar{1}$, 2)	1.024
(1, $\bar{2}$, 0)	0.939
(1, $\bar{2}$, 1)	1.065
(1, $\bar{2}$, 2)	0.957
(1, 0, 0)	0.713
(1, 0, 1)	0.879
(1, 0, 2)	1.032
(1, 1, 0)	0.921
(1, 1, 1)	0.951
(1, 1, 2)	1.078
(1, 2, 0)	0.787
(1, 2, 1)	1.192
(1, 2, 2)	1.059
(2, $\bar{1}$, 0)	1.017
(2, $\bar{1}$, 1)	1.033
(2, $\bar{1}$, 2)	0.878
(2, $\bar{2}$, 1)	1.078
(2, 0, 1)	0.899
(2, 1, 0)	0.841
(2, 1, 1)	0.845
(2, 1, 2)	1.061
(2, 2, 1)	0.934

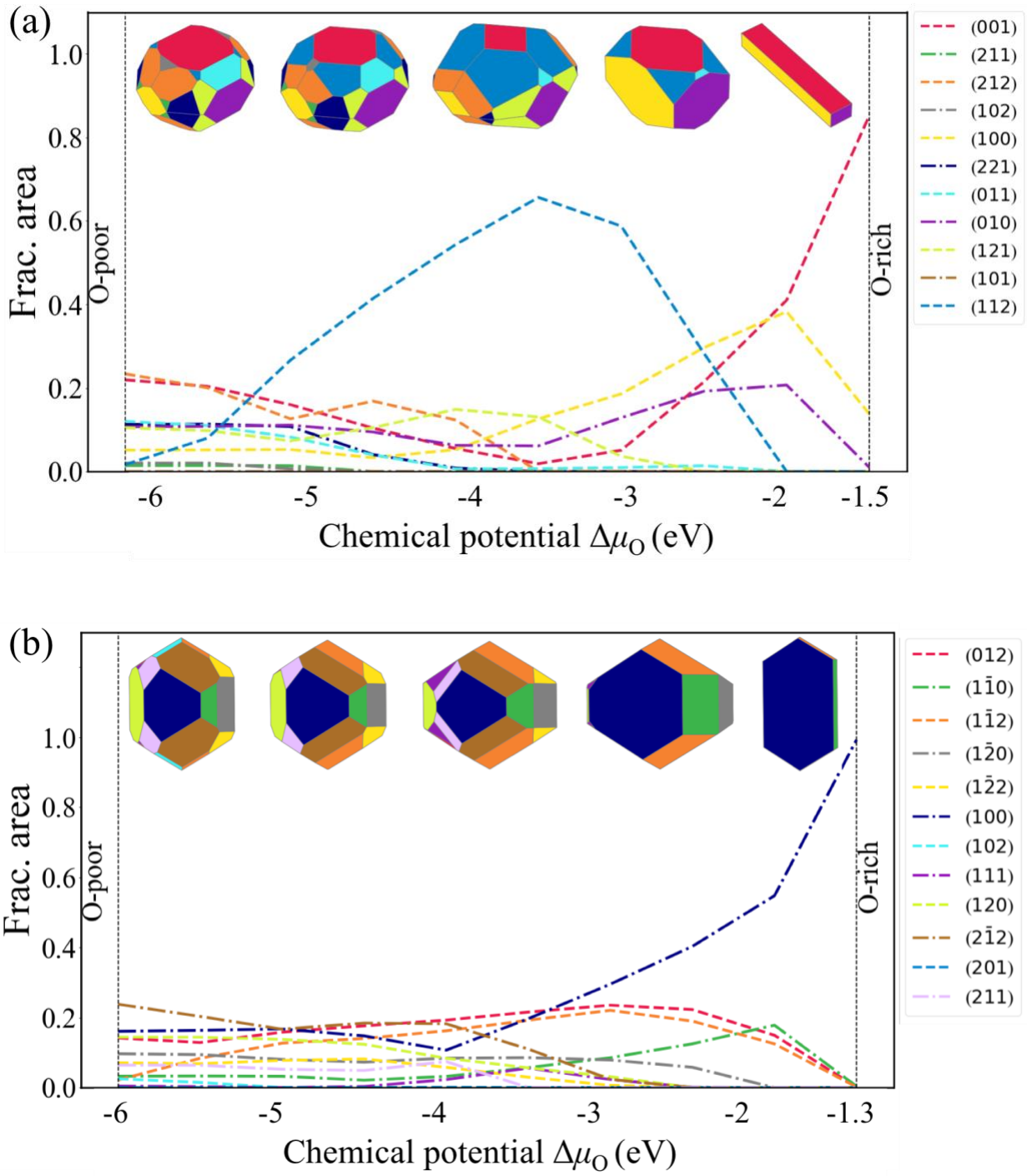

Figure 4.19 The fractional area of different facets and the Wulff shape as a function of $\Delta\mu_O$ for (a) β- and (b) ε-$LiVOPO_4$.

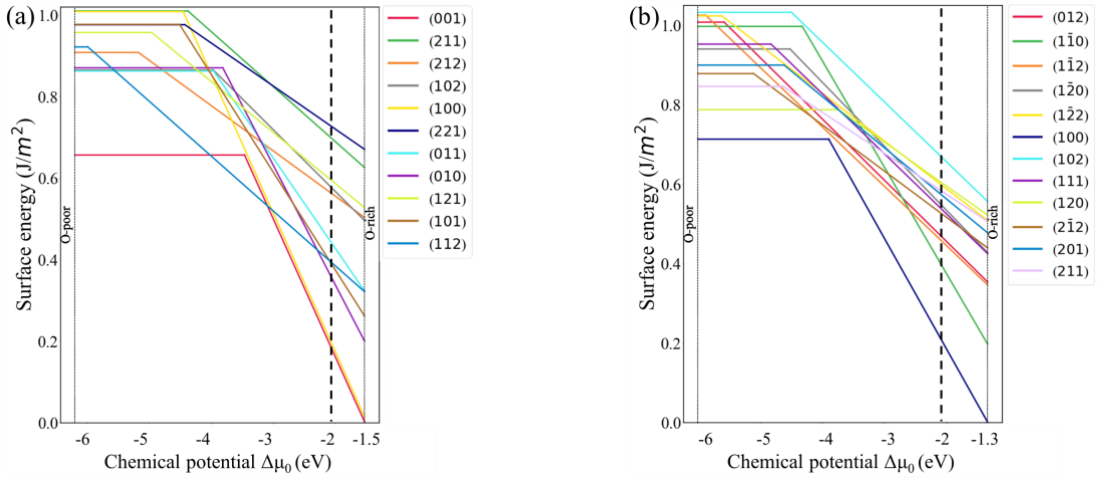

Figure 4.20 The evolution of surface energy of different facets with $\Delta\mu_O$ for (a) β- and (b) ε-$LiVOPO_4$.

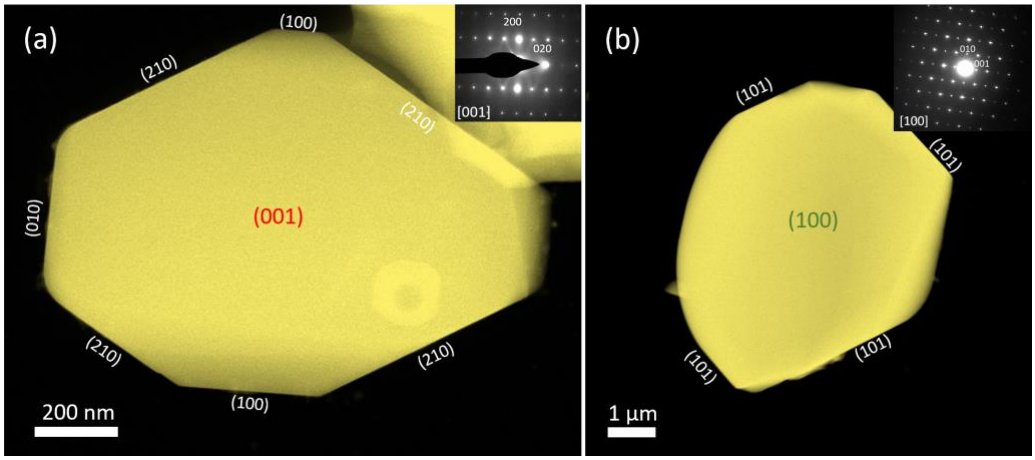

Figure 4.21 TEM image of (a) β- and (b) ε-$LiVOPO_4$ showing the major facets.

Table 4.2 Calculated redox potentials for the extraction of Li from different surfaces on the Wulff shape of $LiVOPO_4$, with the bulk potential provided for comparison.

β-$LiVOPO_4$						
Facet	(121)	(221)	(011)	(211)	(102)	(001)
Voltage (V)	4.51	4.35	4.33	4.12	4.02	3.88
Facet	(212)	(112)	(010)	(100)	(101)	Bulk
Voltage (V)	3.83	3.75	3.71	3.18	3.03	3.83

ε-$LiVOPO_4$						
Facet	(111)	(201)	(100)	(102)	$(1\bar{1}2)$	$(1\bar{2}0)$
Voltage (V)	4.63	4.17	3.82	3.79	3.63	3.45
Facet	(120)	(012)	$(1\bar{2}2)$	$(2\bar{1}2)$	(211)	$(1\bar{1}0)$
Voltage (V)	3.36	3.28	3.15	3.14	3.12	3.12
Facet	Bulk					
Voltage (V)	3.80					

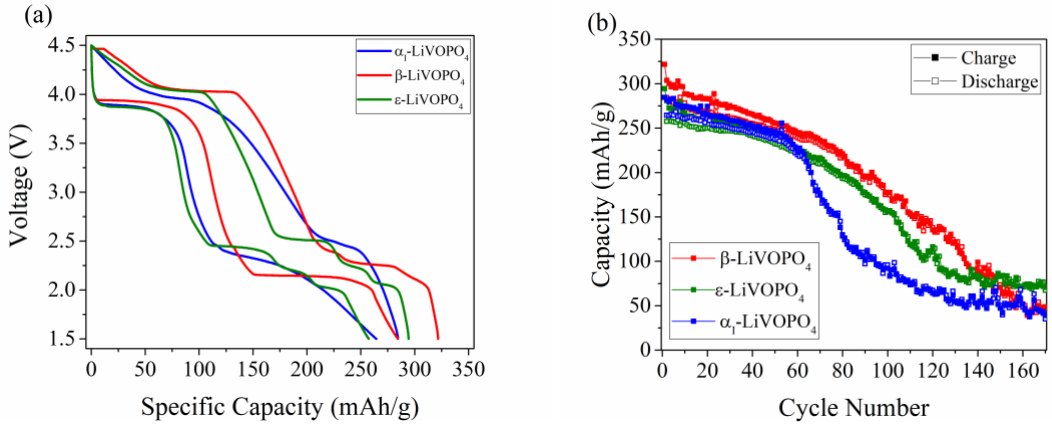

Figure 4.22 Comparison of the (a) first charge-discharge curves and (b) cycling performance, all at C/40, of the different $LiVOPO_4$ polymorphs.

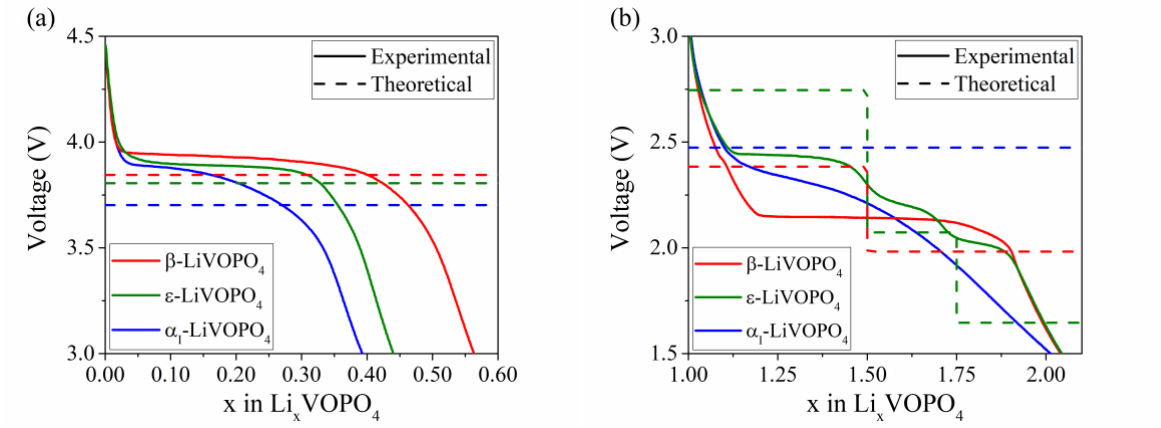

Figure 4.23 Experimental vs theoretical voltage plateaus in the (a) high- and (b) low-voltage regions of the different $LiVOPO_4$ polymorphs, cycled at C/40.

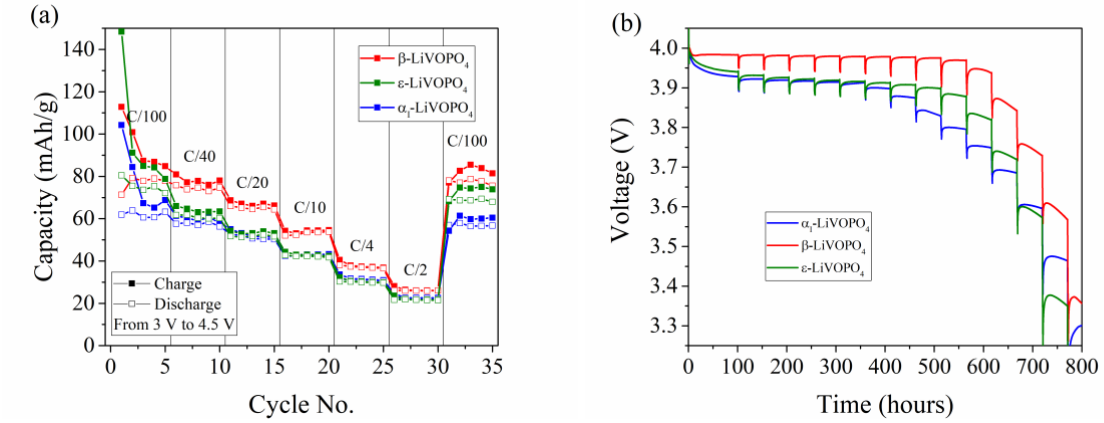

Figure 4.24 Comparison of the (a) rate capability and (b) GITT in the high-voltage region of the different $LiVOPO_4$ polymorphs.

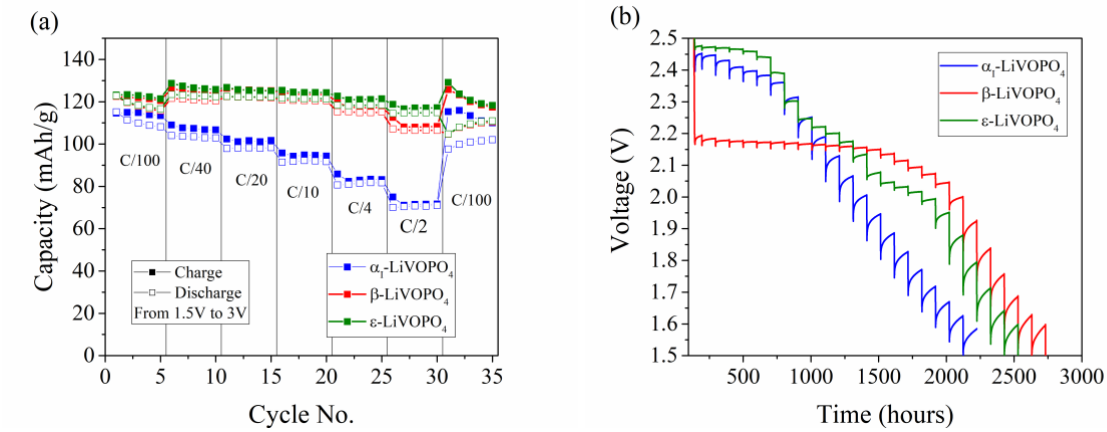

Figure 4.25 Comparison of the (a) rate capability and (b) GITT in the low-voltage region of the different $LiVOPO_4$ polymorphs.

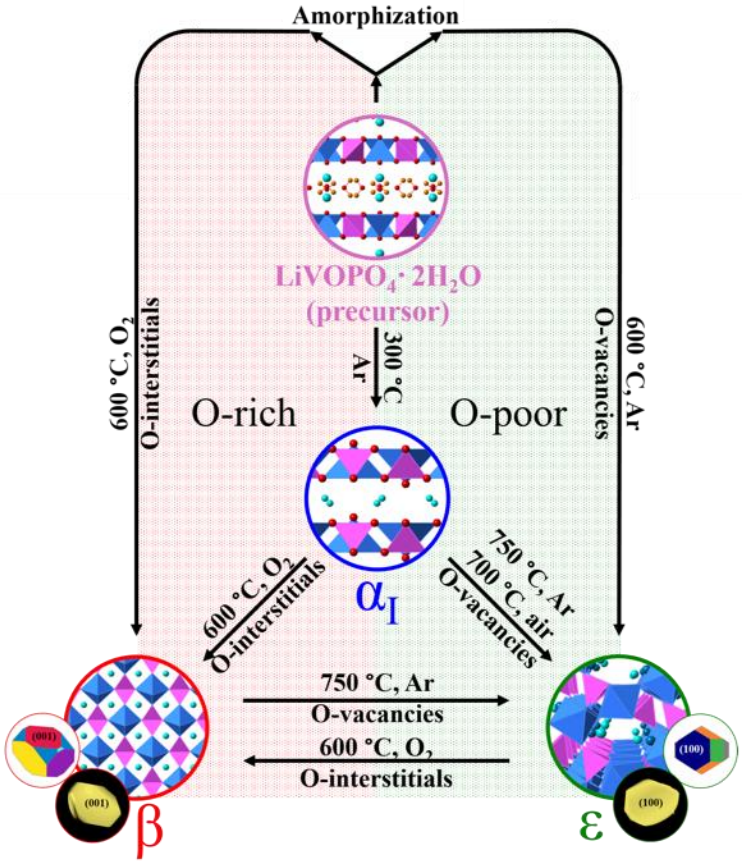

Figure 4.26 Summary of experimental phase transformations between the different polymorphs of $LiVOPO_4$.

Chapter 5. Summary and outlook

Multi-electron polyanion cathodes offer the potential for achieving both high voltage and high capacity in rechargeable AIB. In this thesis, we focused on the study of one of the promising multielectron cathodes, $AVOPO_4$. (A = Li, Na). Using first-principle calculations, we predicted the thermodynamic stabilities, kinetics and surface properties of $AVOPO_4$, which elucidate the experimental findings and serve to guide experiments in improving the electrochemical performance of $AVOPO_4$.

Firstly, we conducted a joint experimental and first-principles computational analysis of the thermodynamics, kinetics structural evolution of the highly promising ε-Li_xVOPO_4 cathode over its entire lithiation range ($0 \leq x \leq 2$). Using both GGA+U and HSE calculations, we find that consistent with previous experimental data, there are no intermediate phases predicted to be stable in the region of $0 \leq x \leq 1$, and two stable intermediate phases are identified at $x = 1.5$ and 1.75. We also find that the thermodynamic stability decreases with the incorporation of the second lithium into ε-$VOPO_4$, suggesting that there are inherent challenges to achieving stable two-electron cycling. Using a combination of DFT calculations, GITT measurements, operando PDF analysis and EXAFS spectra, we show that the capacity limitations during delithiation is likely to be driven by Li mobility limitations, whereas the increasing polarization during lithiation is the result of structural changes. In terms of electronic conductivity, we find ε-Li_xVOPO_4 to be a large band gap insulator across the entire lithiation range, and calculated small polaron migration barriers are similar to those of the olivine $LiMPO_4$ cathodes.[72] Finally, we demonstrate that $LiVOPO_4$ is likely to be a one-dimensional diffuser using climbing-image nudged elastic band calculations. These results highlight the importance of nano-sizing and carbon coating in achieving good electrochemical performance in this material.

In the second project, we performed a combined first-principles and experimental study to evaluate the thermodynamic stability, voltage and diffusion kinetics for Li and Na intercalation in the β, ε and α_I polymorphs of $VOPO_4$. We find that all A_xVOPO_4 polymorphs remain reasonably stable with one alkali intercalation, but significantly destabilizes with two alkali ion intercalation. The electronic band gap calculations suggest that carbon coating is critical for improving the electron conduction in A_xVOPO_4 (A=Li, Na; x=0, 1, 2). The computed alkali diffusion barriers indicate that the alkali diffusion of A_xVOPO_4 (A=Li, Na; x=0, 1) are more facile in α_I polymorph compared to β and ε polymorphs, especially for the larger Na^+ ion. The primary reason is that larger size of the Na^+ makes it particularly sensitive to changes in bottleneck size as a result of the fundamentally different VO_6/VO_5-PO_4 frameworks of the different polymorphs. These results provide crucial insights, such as the importance of structural selection, into the design of new multi-electron cathodes for Li-ion and Na-ion batteries.

In the third project, we conducted a thorough study on the effects of temperature and environment on the stability and formation of the different polymorphs of $LiVOPO_4$ using the identical precursor, $LiVOPO_4 \cdot 2H_2O$. The phase stability from 0 – 1000 K via Gibbs free energy calculations for the three phases is: α_I-$LiVOPO_4$ <<< ε-$LiVOPO_4$ ≤ β-$LiVOPO_4$, which is consistent with the experimental phase transformation process: α_I-$LiVOPO_4 \rightarrow \beta$-$LiVOPO_4 \leftrightarrow \varepsilon$-$LiVOPO_4$. By O-defect calculations, we showed that β-$LiVOPO_4$ and ε-$LiVOPO_4$ preferentially form in O-rich and O-deficient environments, respectively. Indeed, we achieved the largest amount of β-$LiVOPO_4$ phase in oxidizing atmospheres and pure ε-$LiVOPO_4$ phase in Ar atmospheres at high temperatures (> 750 °C). The study of effect of O chemical potential on particle morphology indicates that only the surface rate performance of β-$LiVOPO_4$ can be improved by synthesis under O-rich environments. The calculated dominant facets of β-, and ε-$LiVOPO_4$ are further verified on

the experimental particle morphologies by TEM. Finally, we performed extensive electrochemical testing demonstrating that β phase is the most promising cathode material with the highest capacity and best rate capability among the three phases. This may be ascribed to its superior ionic kinetics and rate performances on the surfaces as the particle size approaches the nanoscale.

To date, there are much fewer works on multielectron than single-electron systems in LIB and NIB, which might be attributed to (1) the instability of the active material in both charged and discharged states, (2) the large volume change making reversibility difficult and (3) the large gap of stepwise voltages due to phase transformations leading to fluctuated power output. The large voltage gap can be ascribed to the large difference of voltage contribution from the multiple redox couple of transition metal. Hautier et al. proposed a mixing-transition-metal strategy to design multielectron phosphate-based cathodes active in the voltage stability window.[196] This also potentially minimized the voltage gaps by the effective redox couples of both transition metals. Besides V, Mo, Cr, Ni, Bi, Sb are shown potentially with small voltage difference across multiple redox reactions in phosphates, which can be guidance to look for novel small-voltage-gap cathodes.[100] We believe in the near future, computational tools will be critically important to facilitate new electrode materials discovery, development and optimization, at the same time minimizing the traditional experimental trials.

Reference

1. Armand, J.-M. T. and M. Issues and challenges facing rechargeable lithium batteries. *Mater. Sustain. Energy* 171–179 (2010).

2. Palomares, V. Na-ion batteries, recent advances and present challenges to become low cost energy storage systems. *Energy Environ. Sci.* 5, 5884 (2012).

3. Karina B. Hueso, M. A. and T. R. High temperature sodium batteries: Status, challenges and future trends. *Energy Environ. Sci.* 1364–1371 (2011).

4. Slater, M. D., Kim, D., Lee, E. & Johnson, C. S. Sodium-ion batteries. *Adv. Funct. Mater.* 23, 947–958 (2013).

5. Palomares, V., Casas-Cabanas, M., Castillo-Martínez, E., Han, M. H. & Rojo, T. Update on Na-based battery materials. A growing research path. *Energy and Environmental Science* 6, 2312–2337 (2013).

6. Whittingham, M. S. History, Evolution, and Future Status of Energy Storage. *Proc. IEEE* 100, 1518–1534 (2012).

7. Arai, H., Okada, S., Sakurai, Y. & Yamaki, J. Cathode performance and voltage estimation of metal trihalides. *J. Power Sources* 68, 716–719 (1997).

8. Lindic, M. H. XPS investigations of TiO_ySz amorphous thin films used as positive electrode in lithium microbatteries. *Solid State Ionics* 176, 1529–1537 (2005).

9. Whittingham, M. S. Chemistry of intercalation compounds: Metal guests in chalcogenide hosts. *Progress in Solid State Chemistry* 12, 41–99 (1978).

10. Holleck, G. L. & Driscoll, J. R. Transition metal sulfides as cathodes for secondary lithium batteries-II. titanium sulfides. *Electrochim. Acta* 22, 647–655 (1977).

11. Whittingham, M. S. The Role of Ternary Phases in Cathode Reactions. *J. Electrochem. Soc.* 123, 315 (1976).

12. Sakuda, A. Amorphous TiS_4 positive electrode for lithium-sulfur secondary batteries. *Electrochem. commun.* 31, 71–75 (2013).

13. Hayashi, A., Matsuyama, T., Sakuda, A. & Tatsumisago, M. Amorphous Titanium Sulfide Electrode for All-solid-state Rechargeable Lithium Batteries with High Capacity. *Chem. Lett.* 41, 886–888 (2012).

14. Sakuda, A. Rock-salt-type lithium metal sulphides as novel positive-electrode materials. *Sci. Rep.* 4, 4883 (2014).

15. Delmas, C., $Li_xV_2O_5$ - a new electrode material for rechargeable lithium batteries. *J. Power Sources* 34, 113–118 (1991).

16. Azmi, B. M., Ishihara, T., Nishiguchi, H. & Takita, Y. Vanadyl phosphates of $VOPO_4$ as a cathode of Li-ion rechargeable batteries. in *Journal of Power Sources* (2003).

17. Chen, R. Disordered lithium-rich oxyfluoride as a stable host for enhanced Li^+ intercalation storage. *Adv. Energy Mater.* 5, 1–7 (2015).

18. Park, Y. U. A family of high-performance cathode materials for na-ion batteries, $Na_3(VO_{1-x}PO_4)_2$ F_{1+2x} $(0 \leq x \leq 1)$: Combined first-principles and experimental study. *Adv. Funct. Mater.* 24, 4603–4614 (2014).

19. Wu, X. Highly Crystallized $Na_2CoFe(CN)_6$ with Suppressed Lattice Defects as Superior Cathode Material for Sodium-Ion Batteries. *ACS Appl. Mater. Interfaces* 8, 5393–5399 (2016).

20. Park, Y. U. A new high-energy cathode for a Na-ion battery with ultrahigh stability. *J. Am. Chem. Soc.* 135, 13870–13878 (2013).

21. He, G., Kan, W. H. & Manthiram, A. A 3.4 V Layered $VOPO_4$ Cathode for Na-Ion Batteries. *Chem. Mater.* (2016).

22. Hautier, G. Phosphates as lithium-ion battery cathodes: An evaluation based on high-throughput ab initio calculations. *Chem. Mater.* 23, 3495–3508 (2011).

23. Bianchini, M. Multiple phases in the ε-VPO_4O–$LiVPO_4O$–Li_2VPO_4O system: a combined solid state electrochemistry and diffraction structural study. *J. Mater. Chem. A* 2, 10182 (2014).

24. Harrison, K. L. Chemical and Electrochemical Lithiation of $LiVOPO_4$ Cathodes for Lithium-Ion Batteries. *Chem. Mater.* 26, 3849–3861 (2014).

25. Chen, Z. Electrochemical Behavior of Nanostructured ε-$VOPO_4$ over Two Redox Plateaus. *J. Electrochem. Soc.* 160, A1777–A1780 (2013).

26. Ong, S. P. Voltage, stability and diffusion barrier differences between sodium-ion and lithium-ion intercalation materials. *Energy Environ. Sci.* 4, 3680–3688 (2011).

27. Shahul Hameed, A., Nagarathinam, M., Reddy, M. V., Chowdari, B. V. R. & Vittal, J. J. Synthesis and electrochemical studies of layer-structured metastable α_I-$LiVOPO_4$. *J. Mater. Chem.* (2012).

28. Allen, C. J., Jia, Q., Chinnasamy, C. N., Mukerjee, S. & Abraham, K. M. Synthesis, Structure and Electrochemistry of Lithium Vanadium Phosphate Cathode Materials. *J. Electrochem. Soc.* (2011).

29. Lin, Y.-C. Thermodynamics, Kinetics and Structural Evolution of ε-$LiVOPO_4$ over Multiple Lithium Intercalation. *Chem. Mater.* (2016).

30. Harrison, K. L. Chemical and Electrochemical Lithiation of $LiVOPO_4$ Cathodes for Lithium-Ion Batteries. *Chem. Mater.* (2014).

31. Barker, J., Saidi, M. Y. & Swoyer, J. L. Electrochemical Properties of Beta-$LiVOPO_4$ Prepared by Carbothermal Reduction. *J. Electrochem. Soc.* (2004).

32. Liu, Z. Synthesis of β-$LiVOPO_4$/C by Sol-gel Method and Microwave Sintering as Cathode Material for Lithium Ion Batteries. *Int. J. Electrochem. Sci.* 12, 10107–10114 (2017).

33. Ateba Mba, J.-M., Masquelier, C., Suard, E. & Croguennec, L. Synthesis and Crystallographic Study of Homeotypic LiVPO4F and $LiVPO_4O$. *Chem. Mater.* (2012).

34. Zhou, H., Shi, Y., Xin, F., Omenya, F. & Whittingham, M. S. ϵ- and β-$LiVOPO_4$: Phase Transformation and Electrochemistry. *ACS Appl. Mater. Interfaces* (2017).

35. Nagamine, K., Honma, T. & Komatsu, T. Selective synthesis of lithium ion-conductive β-LiVOPO4 crystals via glass-ceramic processing. *J. Am. Ceram. Soc.* (2008).

36. Whittingham, M. S. & Thompson, A. H. Intercalation and lattice expansion in titanium disulfide. *The Journal of Chemical Physics* 62, 1588 (1975).

37. Whittingham, M. S. Electrical energy storage and intercalation chemistry. *Science (80-.).* 192, 1126–1127 (1976).

38. Mizushima, K., Jones, P. C., Wiseman, P. J. & Goodenough, J. B. Li_xCoO_2 ($0<x\leq1$): A new cathode material for batteries of high energy density. *Solid State Ionics* 3–4, 171–174 (1981).

39. Padhi, A. K. Phospho-olivines as Positive-Electrode Materials for Rechargeable Lithium Batteries. *J. Electrochem. Soc.* 144, 1188 (1997).

40. Whittingham, M. S. Ultimate limits to intercalation reactions for lithium batteries. *Chemical Reviews* 114, 11414–11443 (2014).

41. Xu, K. Nonaqueous liquid electrolytes for lithium-based rechargeable batteries. *Chem. Rev.* 104, 4303–4417 (2004).

42. Song, Y., Zavalij, P. Y. & Whittingham, M. S. ε-$VOPO_4$: Electrochemical Synthesis and Enhanced Cathode Behavior. *J. Electrochem. Soc.* 152, A721 (2005).

43. Kerr, T. a. Highly Reversible Li Insertion at 4 V in ε-$VOPO_4$/α-$LiVOPO_4$ Cathodes. *Electrochem. Solid-State Lett.* 3, 460 (1999).

44. Borkiewicz, O. J. The AMPIX electrochemical cell: A versatile apparatus for in situ X-ray scattering and spectroscopic measurements. *J. Appl. Crystallogr.* 45, 1261–1269 (2012).

45. Chupas, P. J., Chapman, K. W. & Lee, P. L. Applications of an amorphous silicon-based area detector for high-resolution, high-sensitivity and fast time-resolved pair distribution function measurements. *J. Appl. Crystallogr.* 40, 463–470 (2007).

46. Chupas, P. J. Rapid-acquisition pair distribution function (RA-PDF) analysis. *J. Appl. Crystallogr.* 36, 1342–1347 (2003).

47. Hammersley, A. P., Svensson, S. O., Hanfland, M., Fitch, A. N. & Hausermann, D. Two-dimensional detector software: From real detector to idealised image or two-theta scan. *High Press. Res.* 14, 235–248 (1996).

48. Qiu, X., Thompson, J. W. & Billinge, S. J. L. PDFgetX2: A GUI-driven program to obtain the pair distribution function from X-ray powder diffraction data. *J. Appl. Crystallogr.* 37, 678 (2004).

49. Farrow, C. L. PDFfit2 and PDFgui: Computer programs for studying nanostructure in crystals. *J. Phys. Condens. Matter* 19, (2007).

50. Wojdyr, M. Fityk: A general-purpose peak fitting program. *J. Appl. Crystallogr.* 43, 1126–1128 (2010).

51. ATHENA, ARTEMIS, HEPHAESTUS: Data analysis for X-ray absorption spectroscopy using IFEFFITRavel, B. & Newville, M. ATHENA, ARTEMIS, HEPHAESTUS: Data analysis for X-ray absorption spectroscopy using IFEFFIT. in *Journal of Synchrotron Radiation* 12, 537–541 (2005).

52. Kresse, G. & Furthmüller, J. Efficient iterative schemes for *ab initio* total-energy calculations using a plane-wave basis set. *Phys. Rev. B* 54, 11169–11186 (1996).

53. Blöchl, P. E. Projector augmented-wave method. *Phys. Rev. B* 50, 17953–17979 (1994).

54. Bergerhoff, G., Hundt, R., Sievers, R. & Brown, I. D. The Inorganic Crystal Structure Data Base. *J. Chem. Inf. Comput. Sci.* 23, 66–69 (1983).

55. Hart, G. L. W. & Forcade, R. W. Algorithm for generating derivative structures. *Phys. Rev. B - Condens. Matter Mater. Phys.* 77, (2008).

56. Ong, S. P. Python Materials Genomics (pymatgen): A robust, open-source python library for materials analysis. *Comput. Mater. Sci.* 68, 314–319 (2013).

57. Perdew, J. P., Burke, K. & Ernzerhof, M. Generalized gradient approximation made simple. *Phys. Rev. Lett.* 77, 3865–3868 (1996).

58. Dudarev, S. & Botton, G. Electron-energy-loss spectra and the structural stability of nickel oxide: An LSDA+U study. *Phys. Rev. B - Condens. Matter Mater. Phys.* 57, 1505–1509 (1998).

59. Liechtenstein, A. I., Anisimov, V. I. & Zaanen, J. Density-functional theory and strong interactions: Orbital ordering in Mott-Hubbard insulators. *Phys. Rev. B* 52, (1995).

60. Lichtenstein, V. I. A. and F. A. and A. I. First-principles calculations of the electronic structure and spectra of strongly correlated systems: the LDA + U method. *J. Phys. Condens. Matter* 9, 767 (1997).

61. Jain, A. Commentary: The materials project: A materials genome approach to accelerating materials innovation. *APL Materials* 1, (2013).

62. Ling, C., Zhang, R. & Mizuno, F. Phase stability and its impact on the electrochemical performance of $VOPO_4$ and $LiVOPO_4$. *J. Mater. Chem. A* 2, 12330–12339 (2014).

63. Ong, S. P. The Materials Application Programming Interface (API): A simple, flexible and efficient API for materials data based on REpresentational State Transfer (REST) principles. *Comput. Mater. Sci.* 97, 209–215 (2015).

64. Ong, S. P., Wang, L., Kang, B. & Ceder, G. Li-Fe-P-O_2 phase diagram from first principles calculations. *Chem. Mater.* 20, 1798–1807 (2008).

65. Aydinol, M. K., Kohan, A. F., Ceder, G., Cho, K. & Joannopoulos, J. Ab initio study of lithium intercalation in metal oxides and metal dichalcogenides. *Phys. Rev. B* 56, 1354–1365 (1997).

66. Heyd, J., Scuseria, G. E. & Ernzerhof, M. Hybrid functionals based on a screened Coulomb potential. *J. Chem. Phys.* 118, 8207–8215 (2003).

67. Henkelman, G. & Jónsson, H. Improved tangent estimate in the nudged elastic band method for finding minimum energy paths and saddle points. *J. Chem. Phys.* 113, 9978–9985 (2000).

68. Henkelman, G., Uberuaga, B. P. & Jónsson, H. Climbing image nudged elastic band method for finding saddle points and minimum energy paths. *J. Chem. Phys.* 113, 9901–9904 (2000).

69. Mueller, T., Hautier, G., Jain, A. & Ceder, G. Evaluation of tavorite-structured cathode materials for lithium-ion batteries using high-throughput computing. *Chem. Mater.* 23, 3854–3862 (2011).

70. Henderson, T. M., Paier, J. & Scuseria, G. E. Accurate treatment of solids with the HSE screened hybrid. *Phys. Status Solidi Basic Res.* 248, 767–774 (2011).

71. Heyd, J. & Scuseria, G. E. Efficient hybrid density functional calculations in solids: Assessment of the Heyd-Scuseria-Ernzerhof screened Coulomb hybrid functional. *J. Chem. Phys.* 121, 1187–1192 (2004).

72. Ong, S. P., Chevrier, V. L. & Ceder, G. Comparison of small polaron migration and phase separation in olivine $LiMnPO_4$ and $LiFePO_4$ using hybrid density functional theory. *Phys. Rev. B - Condens. Matter Mater. Phys.* 83, (2011).

73. Ateba Mba, J.-M., Masquelier, C., Suard, E. & Croguennec, L. Synthesis and Crystallographic Study of Homeotypic $LiVPO_4F$ and $LiVPO_4O$. *Chem. Mater.* 24, 1223–1234 (2012).

74. Allen, C. J., Jia, Q., Chinnasamy, C. N., Mukerjee, S. & Abraham, K. M. Synthesis, Structure and Electrochemistry of Lithium Vanadium Phosphate Cathode Materials. *J. Electrochem. Soc.* 158, A1250 (2011).

75. Quackenbush, N. F. Interfacial Effects in ε-Li_xVOPO_4 and Evolution of the Electronic Structure. *Chem. Mater.* 27, 8211–8219 (2015).

76. Vineyard, G. H. Frequency factors and isotope effects in solid state rate processes. *J. Phys. Chem. Solids* 3, 121–127 (1957).

77. Yang, Y. Towards the understanding of poor electrochemical activity of triclinic $LiVOPO_4$: Experimental characterization and theoretical investigations. *Solid State Sci.* 10, 1292–1298 (2008).

78. Chen, Z. New class of nonaqueous electrolytes for long-life and safe lithium-ion batteries. *Nat. Commun.* 4, (2013).

79. Wilde, L., Trommer, J., Steinike, U., Worzala, H. & Wolf, G.-U. Ab initio Structure Analysis of $VO(HPO_4)$. *Mater. Sci. Forum* 278–281, 704–707 (1998).

80. Hutchings, G. J. Vanadium phosphate: A new look at the active components of catalysts for the oxidation of butane to maleic anhydride. *Journal of Materials Chemistry* 14, 3385–3395 (2004).

81. Cabello Sanchez, F. J. Effect of dehydration of $VOPO_4 \cdot 2H_2O$ on the preparation and reactivity of vanadium phosphate catalyst for the oxidation of n-butane. *Catal. Letters* 77, 189–192 (2001).

82. Huang, Y. Thermal Stability and Reactivity of Cathode Materials for Li-Ion Batteries. *ACS Appl. Mater. Interfaces* 8, 7013–7021 (2016).

83. Islam, M. S., Driscoll, D. J., Fisher, C. A. J. & Slater, P. R. Atomic-scale investigation of defects, dopants, and lithium transport in the $LiFePO_4$ olivine-type battery material. *Chem.*

Mater. 17, 5085–5092 (2005).

84. Morgan, D., Van der Ven, A. & Ceder, G. Li Conductivity in Li_xMPO_4 (M = Mn, Fe, Co, Ni) Olivine Materials. *Electrochem. Solid-State Lett.* 7, A30 (2004).

85. Malik, R., Burch, D., Bazant, M. & Ceder, G. Particle size dependence of the ionic diffusivity. *Nano Lett.* 10, 4123–4127 (2010).

86. Lee, K. T. & Cho, J. Roles of nanosize in lithium reactive nanomaterials for lithium ion batteries. *Nano Today* 6, 28–41 (2011).

87. Li, H. & Zhou, H. Enhancing the performances of Li-ion batteries by carbon-coating: Present and future. *Chem. Commun.* 48, 1201–1217 (2012).

88. Saravanan, K., Lee, H. S., Kuezma, M., Vittal, J. J. & Balaya, P. Hollow α-$LiVOPO_4$ sphere cathodes for high energy Li-ion battery application. *J. Mater. Chem.* 21, 10042 (2011).

89. Paul, B. J. Enhanced Storage Capacities in Carbon-Coated Triclinic-$LiVOPO_4$ Cathode with Porous Structure for Li-Ion Batteries. *ECS Electrochem. Lett.* 1, A63–A65 (2012).

90. Xu, Y.-N., Chung, S.-Y., Bloking, J. T., Chiang, Y.-M. & Ching, W. Y. Electronic Structure and Electrical Conductivity of Undoped LiFePO4. *Electrochem. Solid-State Lett.* 7, A131 (2004).

91. Chung, S. Y., Bloking, J. T. & Chiang, Y. M. Electronically conductive phospho-olivines as lithium storage electrodes. *Nat. Mater.* 1, 123–128 (2002).

92. Whittingham, M. S. Ultimate Limits to Intercalation Reactions for Lithium Batteries. *Chem. Rev.* 114, 11414–11443 (2014).

93. Ong, S. P. Voltage, stability and diffusion barrier differences between sodium-ion and lithium-ion intercalation materials. *Energy Environ. Sci.* 4, 3680 (2011).

94. Padhi, A. K., Nanjundaswamy, K. S. & Goodenough, J. B. Phospho olivines as Positive Electrode Materials for Rechargeable Lithium Batteries. *J. Electrochem. Soc.* 144, 1188–1194 (1997).

95. Rangappa, D., Murukanahally, K. D., Tomai, T., Unemoto, A. & Honma, I. Ultrathin Nanosheets of Li_2MSiO_4 (M = Fe, Mn) as High-Capacity Li-Ion Battery Electrode. *Nano Lett.* 12, 1146–1151 (2012).

96. Islam, M. S. Silicate cathodes for lithium batteries: alternatives to phosphates, *J. Mater. Chem.* 21, 9811 (2011).

97. Kuganathan, N. & Islam, M. S. Li_2MnSiO_4 lithium battery material: Atomic-scale study of defects, lithium mobility, and trivalent dopants. *Chem. Mater.* 21, 5196–5202 (2009).

98. Armstrong, A. R., Kuganathan, N., Islam, M. S. & Bruce, P. G. Structure and Lithium Transport Pathways in Li 2 FeSiO 4 Cathodes for Lithium Batteries. *J. Am. Chem. Soc.* 133, 13031–13035 (2011).

99. Zhang, P. Effects of Na Substitution on Li Ion Migration in Li_2CoSiO_4 Cathode Material. *J. Electrochem. Soc.* 160, A658–A661 (2013).

100. Hautier, G. Phosphates as Lithium-Ion Battery Cathodes: An Evaluation Based on High-Throughput ab Initio Calculations. *Chem. Mater.* 23, 3495–3508 (2011).

101. Saïdi, M. Y., Barker, J., Huang, H., Swoyer, J. L. & Adamson, G. Performance characteristics of lithium vanadium phosphate as a cathode material for lithium-ion batteries. in *Journal of Power Sources* 119–121, 266–272 (2003).

102. Patoux, S., Wurm, C., Morcrette, M., Rousse, G. & Masquelier, C. A comparative structural and electrochemical study of monoclinic $Li_3Fe_2(PO_4)_3$ and $Li_3V_2(PO_4)_3$. in *Journal of Power Sources* 119–121, 278–284 (2003).

103. Jain, A. A Computational Investigation of $Li_9M_3(P_2O_7)_3(PO_4)_2$ (M = V, Mo) as Cathodes for Li Ion Batteries. *J. Electrochem. Soc.* 159, A622 (2012).

104. Makimura, Y., Cahill, L. S., Iriyama, Y., Goward, G. R. & Nazar, L. F. Layered Lithium Vanadium Fluorophosphate, $Li_5V(PO_4)_2F_2$: A 4 V Class Positive Electrode Material for Lithium-Ion Batteries. *Chem. Mater.* 20, 4240–4248 (2008).

105. Yin, S. C., Grondey, H., Strobel, P., Anne, M. & Nazar, L. F. Electrochemical property: Structure relationships in monoclinic $Li_{3-y}V_2(PO_4)_3$. *J. Am. Chem. Soc.* 125, 10402–10411 (2003).

106. Lim, S. Y., Kim, H., Shakoor, R. A., Jung, Y. & Choi, J. W. Electrochemical and Thermal Properties of NASICON Structured $Na_3V_2(PO_4)_3$ as a Sodium Rechargeable Battery Cathode: A Combined Experimental and Theoretical Study. *J. Electrochem. Soc.* 159, A1393–A1397 (2012).

107. Shakoor, R. A. A combined first principles and experimental study on $Na_3V_2(PO_4)_2F_3$ for rechargeable Na batteries. *J. Mater. Chem.* 22, 20535 (2012).

108. Matts, I. L., Dacek, S., Pietrzak, T. K., Malik, R. & Ceder, G. Explaining Performance-Limiting Mechanisms in Fluorophosphate Na-Ion Battery Cathodes through Inactive Transition-Metal Mixing and First-Principles Mobility Calculations. *Chem. Mater.* 27, 6008–6015 (2015).

109. Lin, Y.-C. Thermodynamics, Kinetics and Structural Evolution of ε-$LiVOPO_4$ over Multiple Lithium Intercalation. *Chem. Mater.* 28, 1794–1805 (2016).

110. Song, J., Xu, M., Wang, L. & Goodenough, J. B. Exploration of $NaVOPO_4$ as a cathode for a Na-ion battery. *Chem. Commun.* 49, 5280–5282 (2013).

111. He, G., Kan, W. H. & Manthiram, A. A 3.4 V Layered $VOPO_4$ Cathode for Na-Ion Batteries. *Chem. Mater.* 28, 682–688 (2016).

112. He, G., Huq, A., Kan, W. H. & Manthiram, A. β-$NaVOPO_4$ Obtained by a Low-Temperature Synthesis Process: A New 3.3 V Cathode for Sodium-Ion Batteries. *Chem. Mater.* 28, 1503–1512 (2016).

113. Quackenbush, N. F. Interfacial Effects in ε-Li_xVOPO_4 and Evolution of the Electronic Structure. *Chem. Mater.* 27, 8211–8219 (2015).

114. He, G., Bridges, C. A. & Manthiram, A. Crystal Chemistry of Electrochemically and Chemically Lithiated Layered α_I-$LiVOPO_4$. *Chem. Mater.* 27, 6699–6707 (2015).

115. Harrison, K. L. Chemical and electrochemical lithiation of $LiVOPO_4$ cathodes for lithium-ion batteries. *Chem. Mater.* 26, 3849–3861 (2014).

116. Bianchini, M. Multiple phases in the ε-VPO_4O–$LiVPO_4O$–Li_2VPO_4O system: a combined solid state electrochemistry and diffraction structural study. *J. Mater. Chem. A* 2, 10182 (2014).

117. Chen, Z. Electrochemical Behavior of Nanostructured ε-$VOPO_4$ over Two Redox Plateaus. *J. Electrochem. Soc.* 160, A1777–A1780 (2013).

118. Harrison, K. L. & Manthiram, A. Microwave-assisted solvothermal synthesis and characterization of various polymorphs of $LiVOPO_4$. *Chem. Mater.* 25, 1751–1760 (2013).

119. Hellenbrandt, M. The Inorganic Crystal Structure Database (ICSD)—Present and Future. *Crystallogr. Rev.* 10, 17–22 (2014).

120. Girgsdies, F., Schneider, M., Brückner, A., Ressler, T. & Schlögl, R. The crystal structure of δ-$VOPO_4$ and its relationship to ω-$VOPO_4$. *Solid State Sci.* 11, 1258–1264 (2009).

121. Shahul Hameed, A. Synthesis and electrochemical studies of layer-structured metastable α_1-$LiVOPO_4$. *J. Mater. Chem.* 22, 7206–7213 (2012).

122. Kerr, T. a. Highly Reversible Li Insertion at 4 V in ε-$VOPO_4$/α-$LiVOPO_4$ Cathodes. *Electrochem. Solid-State Lett.* 3, 460 (1999).

123. Gaubicher, J. Li/β-$VOPO_4$: A New 4 V System for Lithium Batteries. *J. Electrochem. Soc.* 146, 4375 (1999).

124. Allen, C. J., Jia, Q., Chinnasamy, C. N., Mukerjee, S. & Abraham, K. M. Synthesis, Structure and Electrochemistry of Lithium Vanadium Phosphate Cathode Materials. *J.*

Electrochem. Soc. 158, 1250–1259 (2011).

125. Song, J., Xu, M., Wang, L. & Goodenough, J. B. Exploration of $NaVOPO_4$ as a cathode for a Na-ion battery. *Chem. Commun.* 49, 5280–5282 (2013).

126. Kresse, G. & Furthmüller, J. Efficient iterative schemes for ab initio total-energy calculations using a plane-wave basis set. *Phys. Rev. B* 54, 11169–11186 (1996).

127. Blochl, P. E. Projector augmented-wave method. *Phys. Rev. B* 50, 17953–17979 (1994).

128. Ong, S. P. Python Materials Genomics (pymatgen): A robust, open-source python library for materials analysis. *Comput. Mater. Sci.* 68, 314–319 (2013).

129. Deng, Z., Zhu, Z., Chu, I.-H. & Ong, S. P. Data-Driven First-Principles Methods for the Study and Design of Alkali Superionic Conductors. *Chem. Mater.* 29, 281–288 (2017).

130. Dupré, N., Wallez, G., Gaubicher, J. & Quarton, M. Phase transition induced by lithium insertion in α_I- and α_{II}-$VOPO_4$. *J. Solid State Chem.* 177, 2896–2902 (2004).

131. Perdew, J. P., Burke, K. & Ernzerhof, M. Generalized Gradient Approximation Made Simple. *Phys. Rev. Lett.* 77, 3865–3868 (1996).

132. Dudarev, S. L., Botton, G. A., Savrasov, S. Y., Humphreys, C. J. & Sutton, a. P. Electron-energy-loss spectra and the structural stability of nickel oxide: An LSDA+U study. *Phys. Rev. B* 57, 1505–1509 (1998).

133. Liechtenstein, A. I., Anisimov, V. I. & Zaanen, J. Density-functional theory and strong interactions: Orbital ordering in Mott-Hubbard insulators. *Phys. Rev. B* 52, R5467–R5470 (1995).

134. Jain, A. Commentary: The materials project: A materials genome approach to accelerating materials innovation. *APL Mater.* 1, 011002 (2013).

135. Ping Ong, S. $Li-Fe-P-O_2$ Phase Diagram from First Principles Calculations. *Chem. Mater.* 20, 1798–1807 (2008).

136. Ong, S. P. The Materials Application Programming Interface (API): A simple, flexible and efficient API for materials data based on REpresentational State Transfer (REST) principles. *Comput. Mater. Sci.* 97, 209–215 (2015).

137. Heyd, J. & Scuseria, G. E. Efficient hybrid density functional calculations in solids: Assessment of the Heyd-Scuseria-Ernzerhof screened Coulomb hybrid functional. *J. Chem. Phys.* 121, 1187–1192 (2004).

138. Henderson, T. M., Paier, J. & Scuseria, G. E. Accurate treatment of solids with the HSE screened hybrid. *Phys. Status Solidi Basic Res.* 248, 767–774 (2011).

139. Henkelman, G. & Jónsson, H. Improved tangent estimate in the nudged elastic band method for finding minimum energy paths and saddle points. *J. Chem. Phys.* 113, 9978–9985 (2000).

140. Henkelman, G., Uberuaga, B. P. & Jónsson, H. A climbing image nudged elastic band method for finding saddle points and minimum energy paths. *J. Chem. Phys.* 113, 9901 (2000).

141. Mueller, T., Hautier, G., Jain, A. & Ceder, G. Evaluation of Tavorite-Structured Cathode Materials for Lithium-Ion Batteries Using High-Throughput Computing. *Chem. Mater.* 23, 3854–3862 (2011).

142. Smidstrup, S., Pedersen, A., Stokbro, K. & Jónsson, H. Improved initial guess for minimum energy path calculations. *J. Chem. Phys.* 140, 214106 (2014).

143. Lord, H. L., Zhan, W. & Pawliszyn, J. in *Comprehensive Sampling and Sample Preparation* 6, 677–697 (Elsevier, 2012).

144. Song, Y., Zavalij, P. Y. & Whittingham, M. S. ε-$VOPO_4$: Electrochemical Synthesis and Enhanced Cathode Behavior. *J. Electrochem. Soc.* 152, A721 (2005).

145. Lim, S.; Vaughey, J.T.; Harrison, W.T.A.; Dussack, L.L.; Jacobson, A.J.; Johnson, J. W. Redox transformations of simple vanadium phosphates: the synthesis of ε-$VOPO_4$. *Solid State Ionics* 84, 219–226 (1996).

146. Azmi, B. M., Ishihara, T., Nishiguchi, H. & Takita, Y. Cathodic performance of $VOPO_4$ with various crystal phases for Li ion rechargeable battery. *Denki Kagaku* 48, 165–170 (2002).

147. Tachez, M., Theobald, F. & Bordes, E. A structural explanation for the polymorphism of the α form of anhydrous vanadyl phosphate. *J. Solid State Chem.* 40, 280–283 (1981).

148. Byron Jorda & Crispin Calv. Crystal Structure of α-VPO_5. *Can. J. Chem.* 51, 2621 (1973).

149. Barker, J., Saidi, M. Y. & Swoyer, J. L. Electrochemical Properties of β-$LiVOPO_4$ Prepared by Carbothermal Reduction. *J. Electrochem. Soc.* 151, A796 (2004).

150. Azmi, B. M., Ishihara, T., Nishiguchi, H. & Takita, Y. Vanadyl phosphates of $VOPO_4$ as a cathode of Li-ion rechargeable batteries. *J. Power Sources* 119–121, 273–277 (2003).

151. Wangoh, L. W. Uniform second Li ion intercalation in solid state ϵ-$LiVOPO_4$. *Appl. Phys. Lett.* 109, 053904 (2016).

152. Perdew, J. Restoring the Density-Gradient Expansion for Exchange in Solids and Surfaces. *Phys. Rev. Lett.* 100, 136406 (2008).

153. Kang, K. & Ceder, G. Factors that affect Li mobility in layered lithium transition metal oxides. *Phys. Rev. B* 74, 094105 (2006).

154. Martin, R. L., Smit, B. & Haranczyk, M. Addressing challenges of identifying geometrically diverse sets of crystalline porous materials. in *Journal of Chemical Information and Modeling* 52, 308–318 (2012).

155. Willems, T. F., Rycroft, C. H., Kazi, M., Meza, J. C. & Haranczyk, M. Algorithms and tools for high-throughput geometry-based analysis of crystalline porous materials. *Microporous Mesoporous Mater.* 149, 134–141 (2012).

156. Dominko, R. Impact of the carbon coating thickness on the electrochemical performance of $LiFePO_4$/C composites. *J. Electrochem. Soc.* 152, A607–A610 (2005).

157. Barker, J., Saidi, M. Y. & Swoyer, J. L. Lithium Iron(II) Phospho-olivines Prepared by a Novel Carbothermal Reduction Method. *Electrochem. Solid-State Lett.* 6, A53–A55 (2003).

158. Gopal, R. & Calvo, C. Crystal structure of βVPO_5. *J. Solid State Chem.* 5, 432–435 (1972).

159. Lii, K. H., Li, C. H., Cheng, C. Y. & Wang, S. L. Hydrothermal synthesis, structure, and magnetic properties of a new polymorph of lithium vanadyl(IV) orthophosphate: β-$LiVOPO_4$. *J. Solid State Chem.* 95, 352–359 (1991).

160. Girgsdies, F. The crystal structure of ε-$VOPO_4$. *Solid State Sci.* 8, 807–812 (2006).

161. Yang, Y. Towards the understanding of poor electrochemical activity of triclinic $LiVOPO_4$: Experimental characterization and theoretical investigations. *Solid State Sci.* 10, 1292–1298 (2008).

162. Whittingham, M. S. History, Evolution, and Future Status of Energy Storage. *Proc. IEEE* (2012).

163. Lu, L., Han, X., Li, J., Hua, J. & Ouyang, M. A review on the key issues for lithium-ion battery management in electric vehicles. *Journal of Power Sources* (2013).

164. Whittingham, M. S. Ultimate limits to intercalation reactions for lithium batteries. *Chemical Reviews* (2014).

165. Blomgren, G. E. The Development and Future of Lithium Ion Batteries. *J. Electrochem. Soc.* (2017).

166. Whittingham, M. S. Lithium batteries and cathode materials. *Chem. Rev.* (2004).

167. Etacheri, V., Marom, R., Elazari, R., Salitra, G. & Aurbach, D. Challenges in the development of advanced Li-ion batteries: a review. *Energy Environ. Sci.* (2011).

168. Ding, J. $KVOPO_4$: A New High Capacity Multielectron Na-Ion Battery Cathode. *Adv. Energy Mater.* (2018).

169. Chen, R., Luo, R., Huang, Y., Wu, F. & Li, L. Advanced High Energy Density Secondary Batteries with Multi-Electron Reaction Materials. *Advanced Science* (2016).

170. Armand, M. & Tarascon, J. M. Building better batteries. *Nature* (2008).

171. Kim, S. W., Seo, D. H., Ma, X., Ceder, G. & Kang, K. Electrode materials for rechargeable sodium-ion batteries: Potential alternatives to current lithium-ion batteries. *Advanced Energy Materials* (2012).

172. Gao, X. P. & Yang, H. X. Multi-electron reaction materials for high energy density batteries. *Energy and Environmental Science* (2010).

173. Wang, C., Sawicki, M., Emani, S., Liu, C. & Shaw, L. L. $Na_3MnCO_3PO_4$- A high capacity, multi-electron transfer redox cathode material for sodium ion batteries. *Electrochim. Acta* (2015).

174. Hautier, G. Designing multielectron lithium-ion phosphate cathodes by mixing transition Metals. *Chem. Mater.* (2013).

175. Liu, J., Yin, L., Yang, X. Q. & Khalifah, P. G. $Li_3VP_3O_9N$ as a Multielectron Redox Cathode for Li-Ion Battery. *Chem. Mater.* 30, 4609–4616 (2018).

176. Lin, Y. C. Comparison of the polymorphs of $VOPO_4$ as multi-electron cathodes for rechargeable alkali-ion batteries. *J. Mater. Chem. A* (2017).

177. Hautier, G. Phosphates as lithium-ion battery cathodes: An evaluation based on high-throughput ab initio calculations. *Chem. Mater.* (2011).

178. Siu, C. Enabling multi-electron reaction of ε-$VOPO_4$ to reach theoretical capacity for lithium-ion batteries. *Chem. Commun.* (2018).

179. Bianchini, M. Multiple phases in the ε-VPO_4O–$LiVPO_4O$–Li_2VPO_4O system: a combined solid state electrochemistry and diffraction structural study. *J. Mater. Chem. A* (2014).

180. Tachez, M., Theobald, F. & Bordes, E. A structural explanation for the polymorphism of the α form of anhydrous vanadyl phosphate. *J. Solid State Chem.* (1981).

181. He, G., Bridges, C. A. & Manthiram, A. Crystal Chemistry of Electrochemically and Chemically Lithiated Layered αI-LiVOPO4. *Chem. Mater.* (2015).

182. Dupré, N., Wallez, G., Gaubicher, J. & Quarton, M. Phase transition induced by lithium insertion in α_I- and α_{II}-$VOPO_4$. *J. Solid State Chem.* (2004).

183. Gopal, R. & Calvo, C. Crystal structure of βVPO$_5$. *J. Solid State Chem.* 5, 432–435 (1972).

184. Ren, M. M., Zhou, Z., Su, L. W. & Gao, X. P. LiVOPO$_4$: A cathode material for 4 V lithium ion batteries. *J. Power Sources* (2009).

185. Lii, K. H., Li, C. H., Cheng, C. Y. & Wang, S. L. Hydrothermal synthesis, structure, and magnetic properties of a new polymorph of lithium vanadyl(IV) orthophosphate: β-LiVOPO$_4$. *J. Solid State Chem.* (1991).

186. Song, Y., Zavalij, P. Y. & Whittingham, M. S. ε-VOPO$_4$: Electrochemical Synthesis and Enhanced Cathode Behavior. *J. Electrochem. Soc.* (2005).

187. Ling, C., Zhang, R. & Mizuno, F. Phase stability and its impact on the electrochemical performance of VOPO$_4$ and LiVOPO$_4$. *J. Mater. Chem. A* (2014).

188. Wang, L. Synthesis of LiVOPO$_4$ for cathode materials by coordination and microwave sintering. *Electrochimica Acta* (2011).

189. Van der Ven, A. Lithium Diffusion in Layered Li$_x$CoO$_2$. *Electrochem. Solid-State Lett.* (1999).

190. Wang, L., Zhou, F., Meng, Y. S. & Ceder, G. First-principles study of surface properties of LiFePO$_4$: Surface energy, structure, Wulff shape, and surface redox potential. *Phys. Rev. B - Condens. Matter Mater. Phys.* (2007).

191. Li, Y. Morphology and surface properties of LiVOPO$_4$: A first principles study. *Phys. Chem. Chem. Phys.* (2014).

192. Togo, A. & Tanaka, I. First principles phonon calculations in materials science. *Scr. Mater.* (2015).

193. Tran, R. Data Descriptor: Surface energies of elemental crystals. *Sci. Data* (2016).

194. Tasker, P. W. The stability of ionic crystal surfaces. *J. Phys. C Solid State Phys.* (1979).

195. Montoya, J. H. & Persson, K. A. A high-throughput framework for determining adsorption energies on solid surfaces. *npj Comput. Mater.* (2017).

196. Hautier, G. Designing multielectron lithium-ion phosphate cathodes by mixing transition Metals. *Chem. Mater.* 25, 2064–2074 (2013).